ADVANCED NONCONTRAST MAGNETIC RESONANCE ANGIOGRAPHY OF THE THORACIC AND PERIPHERAL ARTERIES

by

Marc Daniel Lindley

A dissertation submitted to the faculty of
The University of Utah
in partial fulfillment of the requirements for the degree of

Doctor of Philosophy

in

Physics

Department of Physics and Astronomy

The University of Utah

May 2017

The University of Utah Graduate School

STATEMENT OF DISSERTATION APPROVAL

The dissertation of Marc Daniel Lindley

has been approved by the following supervisory committee members:

Brian Saam, Chair 11/18/2016
Date Approved

Daniel Kim, Member
Date Approved

Edward Dibella, Member
Date Approved

Charles Jui, Member 12/06/2016
Date Approved

Benjamin Bromley, Member 11/22/2016
Date Approved

and by Benjamin Bromley, Chair/Dean of the Department/College/School of Physics and Astronomy

and by David B. Kieda, Dean of The Graduate School.

ABSTRACT

The gold standard for evaluation of arterial disease using MR continues to be contrast-enhanced MR angiography (MRA) with gadolinium-based contrast agents (Gd-MRA). There has been a recent resurgence in interest in methods that do not rely on gadolinium for enhancement of blood vessels due to associations Gd-MRA has with nephrogenic systemic fibrosis (NSF) in patients with impaired renal function. The risk due to NSF has been shown to be minimized when selecting the appropriate contrast type and dose. Even though the risk of NSF has been shown to be minimized, demand for noncontrast MRA has continued to rise to reduce examination cost, and improve patient comfort and ability to repeat scans.

Several methods have been proposed and used to perform angiography of the aorta and peripheral arteries without the use of gadolinium. These techniques have had limitations in transmit radiofrequency field (B1+) inhomogeneities, acquisition time, and specific hardware requirements, which have stunted the utility of noncontrast enhanced MRA.

In this work feasibility of noncontrast (NC) MRA at 3T of the femoral arteries using dielectric padding, and using 3D radial stack of stars and compressed sensing to accelerate acquisitions in the abdomen and thorax were tested.

Imaging was performed on 13 subjects in the pelvis and thighs using high permittivity padding, and 11 in the abdomen and 19 in the thorax using 3D radial stack of stars with tiny golden angle using gold standards or previously published techniques. Qualitative scores for each study were determined by radiologists who were blinded to acquisition type.

Vessel conspicuity in the thigh and pelvis showed significant increase when high permittivity padding was used in the acquisition. No significant difference in image quality was observed in the abdomen and thorax when using undersampling, except for the descending aorta in thoracic imaging. All image quality scores were determined to be of diagnostic quality.

In this work it is shown that NC-MRA can be improved through the use of high permittivity dielectric padding and acquisition time can be decreased through the use of 3D radial stack of stars acquisitions.

Dedicated to my loving wife, Jen, and my kids, Beckett and Priya, without whom this never would have happened. They dealt with a lot through the whole process, and were supportive through the whole thing. It has been an uphill battle, but we have managed to make it through and are stronger than ever. We will always remember the times we had right now and appreciate the work that we had to do. Thank you very much for your love and support through this whole long process.

TABLE OF CONTENTS

Chapters

LIST OF TABLES

Tables

ACKNOWLEDGMENTS

I would like to thank all of my professors, friends, relatives, and everyone who supported me and helped to make this happen.

First, I would like to thank Dr. Daniel Kim, my advisor through this whole process. His knowledge of writing and study design really helped me to solidify my knowledge of the scientific process and how to go about getting papers published. His stern guidance helped me push to new heights and helped me continually strive to develop and do more. It was because of his influence that I know the importance of working closely with clinicians so as to meet their needs.

Second, without the support of Dr. Vivian Lee these projects and the knowledge that I have been able to gain never would have happened. Her support and expertise through this helped guide the work that I was to accomplish. She was constantly mindful of the progress that we were making and was able to offer her insight and advice for the next steps that we should take.

One of the biggest helps through this whole process and without whom none of this would have been done, is Kristi Carlston. Her efforts in recruitment and consenting of patients happened at almost all hours. She truly went above and beyond to try to help my projects come to fruition.

Dr. Andrew Webb helped through the construction and use of the were not as successful as after our conversations about what steps to go through in sealing the bags for long term use and what to challenges I might face through the process.

Thanks to everyone involved, this was truly a team effort.

CHAPTER 1

INTRODUCTION

1.1 Introduction

Peripheral arterial disease (PAD) is a classification of conditions that affect the arteries that are distal to the aortic arch. PAD is most commonly caused by atherosclerosis (1) and is very prevalent today, affecting over 8 million Americans, with 12% to 20% of those being 65 years of age or older (2). Imaging plays an important role in the diagnosis and planning for treatment, because it allows physicians to noninvasively know the extent, severity and location of the disease. The main imaging methods used for visualization of arteries are contrast-enhanced computed tomography angiography (CTA) (3) or magnetic resonance angiography (MRA), both of which present benefits and difficulties in their application.

In order to obtain angiograms, it has been necessary to utilize contrast agents. In CTA, an iodine-based contrast agent is used, while in MRA a gadolinium-based contrast agent is used. CTA can be performed rapidly, but there are safety concerns associated with ionizing radiation and iodine based contrast agent (4) in patients with impaired renal function. Contrast induced nephropathy (CIN) can cause temporary or permanent reduction in kidney function. CTA also has been known to produce image artifacts caused by plaques in the arteries. MRA does not use ionizing radiation to acquire images, but scan times are longer and acquisitions are more technically challenging. In recent years, a few cases of nephrogenic systemic fibrosis (NSF) have been reported (5,6) and a link to the gadolinium-based contrast agents used in MRI has been suggested. Approximately 30% of PAD patients also have renal insufficiency (7), thus being at risk for NSF from the gadolinium-based contrast agent used in MRA or at risk for CIN from iodine-based contrast used in CTA. In addition to risks of NSF, gadolinium deposits have been found in the brains of individuals with normal kidney function (8-10). Due to these concerns, there is a clinical need to develop rapid, safe, robust angiographic methods without the use of gadolinium-based or iodine-based contrast media or ionizing radiation, in order to widen the availability of angiography to all patients, including those with reduced renal function.

In recent years there have been several promising advancements in noncontrast magnetic resonance angiography (NC-MRA)(11-15). Currently the use of NC-MRA has been restricted due to the need for special coils, MRI hardware, or the time that is required to acquire images. In this work, we have developed new NC-MRA methods to image the thoracic aorta, descending aorta, iliacs, and the femoral arteries, using standard MRI hardware, coils, and in clinically acceptable scan times. These improvements could improve the availability of these techniques to more systems and thus more patients, including those who are contraindicated for contrast agents. This has been accomplished through improvements in B1+, or transmit RF field, homogeneity at high field strengths (>3T), reducing the scan time by a factor 2, and performing NC-MRA using standard receiver coils.

The manuscript begins by giving an overview of the principles of MRI, including the current state-of-the-art MRA clinical tools. Chapter 4 discusses k-space sampling and compressed sensing reconstruction techniques. Following this discussion, RF field characteristics and the difficulties presented by higher field strengths will be covered. Chapter 6 describes the use of high-permittivity padding to improve transmit B1 inhomogeneity to improve ECG-based TSE acquisitions of the femoral arteries of the thigh. Chapter 7 will focus on how the acquisition of the aorta and iliac arteries can be acquired in half the normal time through the use of radial stack of stars undersampled k-space and compressed sensing. Chapter 8 will discuss imaging of the thoracic aorta, and how through the use of a T2 prepared acquisition, images of the aorta can be acquired in a single breath-hold with the use of standard receiver coils.

1.2 References

1. Sigvant B, Wiberg-Hedman K, Bergqvist D, Rolandsson O, Andersson B, Persson E, Wahlberg E. A population-based study of peripheral arterial disease prevalence with special focus on critical limb ischemia and sex differences. J Vasc Surg 2007;45:1185-1191.

2. Rosamond W, Flegal K, Furie K, Go A, Greenlund K, Haase N, Hailpern SM, Ho M, Howard V, Kissela B, Kittner S, Lloyd-Jones D, McDermott M, Meigs J, Moy C, Nichol G, O'Donnell C, Roger V, Sorlie P, Steinberger J, Thom T, Wilson M, Hong Y. Heart disease and stroke statistics--2008 update: a report from the American Heart Association Statistics Committee and Stroke Statistics Subcommittee. Circulation 2008;117:e25-146.

3. Sun Z. Diagnostic accuracy of multislice CT angiography in peripheral arterial disease. J Vasc Interv Radiol 2006;17:1915-1921.

4. Davenport MS, Khalatbari S, Dillman JR, Cohan RH, Caoili EM, Ellis JH. Contrast material-induced nephrotoxicity and intravenous low-osmolality iodinated contrast material. Radiology 2013;267:94-105.

5. Sadowski EA, Bennett LK, Chan MR, Wentland AL, Garrett AL, Garrett RW, Djamali A. Nephrogenic systemic fibrosis: risk factors and incidence estimation. Radiology 2007;243:148-157.

6. Hoppe H, Spagnuolo S, Froehlich JM, Nievergelt H, Dinkel HP, Gretener S, Thoeny HC. Retrospective analysis of patients for development of nephrogenic systemic fibrosis following conventional angiography using gadolinium-based contrast agents. Eur Radiol 2010;20:595-603.

7. O'Hare AM, Bertenthal D, Shlipak MG, Sen S, Chren MM. Impact of renal insufficiency on mortality in advanced lower extremity peripheral arterial disease. J Am Soc Nephrol 2005;16:514-519

.

8. Kanda T, Ishii K, Kawaguchi H, Kitajima K, Takenaka D. High signal intensity in the dentate nucleus and globus pallidus on unenhanced T1-weighted MR images: relationship with increasing cumulative dose of a gadolinium-based contrast material. Radiology 2014;270:834-841.

9. McDonald RJ, McDonald JS, Kallmes DF, Jentoft ME, Murray DL, Thielen KR, Williamson EE, Eckel LJ. Intracranial gadolinium deposition after contrast-enhanced MR imaging. Radiology 2015;275:772-782.

10. Errante Y, Cirimele V, Mallio CA, Di Lazzaro V, Zobel BB, Quattrocchi CC. Progressive increase of T1 signal intensity of the dentate nucleus on unenhanced magnetic resonance images is associated with cumulative doses of intravenously administered gadodiamide in patients with normal renal function, suggesting dechelation. Invest Radiol 2014;49:685-690.

11. Wedeen VJ, Meuli RA, Edelman RR, Geller SC, Frank LR, Brady TJ, Rosen BR. Projective imaging of pulsatile flow with magnetic resonance. Science 1985;230:946-948.

12. Miyazaki M, Sugiura S, Tateishi F, Wada H, Kassai Y, Abe H. Non-contrast-enhanced MR angiography using 3D ECG-synchronized half-Fourier fast spin echo. J Magn Reson Imaging 2000;12:776-783.

13. Li D, Lin J, Yan F, Wu Q, Lv W, San Y, Yun H. Unenhanced calf MR angiography at 3.0 T using electrocardiography-gated partial-fourier fast spin echo imaging with variable flip angle. Eur Radiol 2011;21:1311-1322.

14. Atanasova IP, Kim D, Lim RP, Storey P, Kim S, Guo H, Lee VS. Noncontrast MR angiography for comprehensive assessment of abdominopelvic arteries using quadruple inversion-recovery preconditioning and 3D balanced steady-state free precession imaging. J Magn Reson Imaging 2011;33:1430-1439.

15. Shin T, Worters PW, Hu BS, Nishimura DG. Non-contrast-enhanced renal and abdominal MR angiography using velocity-selective inversion preparation. Magn Reson Med 2013;69:1268-1275.

CHAPTER 2

PRINCIPLES OF MAGNETIC RESONANCE IMAGING

Medical imaging using MRI requires taking advantage of the nuclear magnetic resonance (NMR) effect. The nuclear magnetic resonance (NMR) effect was discovered initially in 1946 by Bloch and Purcell (1,2), and has begun to be a useful tool in the noninvasive diagnosis of arterial disease. To improve imaging, it is necessary to understand how the imaging is performed. This section will begin the discussion of the nuclear magnetic resonance effect, and the associated quantum mechanical principles, along with excitation and relaxation mechanisms, and their applications. To improve imaging methods that are already established it is necessary to understand the physics behind MRI to aid in the decisions that are made.

2.1 Nuclear Magnetic Resonance

2.1.1 Nuclear Magnetic Resonance Effect

NMR relies on the intrinsic spin properties of atoms. Atoms with odd numbers of protons and/or neutrons have an angular spin momentum, or a spin, and so they will act as magnetic dipoles. When atoms are not in an external magnetic field the spins will align randomly which results in a zero net magnetization. When placed in a static external magnetic field, the spins will align either parallel or antiparallel to the magnetic field. The spins in the external field will also precess with a known frequency,

$$\omega_0 = \gamma B_0 \tag{2.1}$$

where γ is the gyromagnetic ratio. Different elements will have different gyromagnetic ratios, for example, for hydrogen γ = 42.58 MHz/T. This work focuses on hydrogen atoms with a single proton, or H^1, which due to its abundance in the body is the focus of clinical scans.

When the spins align in the external magnetic field the antiparallel state has higher energy than the parallel state. The lower energy state can transition to the higher energy state by absorbing energy. The energy can be determined through analyzing the Hamiltonian, where

$$H|m_1\rangle = E|m_I\rangle = -\hbar\gamma B_z I_z|m_I\rangle \qquad [2.2]$$

resulting in

$$E = -\hbar\gamma B_z m_I \qquad [2.3]$$

which for a proton where $m_I = \pm\frac{1}{2}$, we get that

$$\Delta E = \hbar\omega_0 \qquad [2.4]$$

where $\hbar$ is Planck's constant, and B_0 is in the z direction. The lower energy state is the preferred state based on the Boltzmann distribution, with the ratio of the number of protons in each state given by

$$\frac{N_-}{N_+} = e^{\frac{-\Delta E}{kT}} , \qquad [2.5]$$

where the number of spins in the lower energy state is given by N_- and the higher by N_+, ΔE is the energy difference between the lower and higher energy states and is given above, and T is the temperature.

With an increase in the main magnetic field, B0, there is an increase in the precession frequency of the protons. There is also an increase in the separation energy between the states, as well as the equilibrium ratio. Based on the ratio of spins parallel and spins antiparallel it is observed that in the limit where the temperature approaches absolute zero all spins point with the applied magnetic field and the magnetization will be complete. But in practice, at the temperatures used in imaging the human body, approximately 310 K, and the magnetic field strengths will vary from 0.35 T to 7 T in clinical practice for whole-body systems and up to 9.4 T systems for head-only scans. For these field strengths, the excess of the spins is on the order of one spin per one million, with 1.5T corresponding to an excess of 10 parallel spins per million.

The total observable magnetization is then the vector sum of all the magnetic moments individually. This can be written generally as

$$\boldsymbol{M} = (N_- - N_+)\boldsymbol{\mu} \qquad [2.6]$$

or it can be written with respect to a particular axis, using the angular orientation to that particular axis, with

$$M_z = N\langle \mu \cos(\theta) \rangle\,. \qquad [2.7]$$

When solving these equations with the Boltzmann distribution, the equilibrium magnetization can be obtained,

$$M_0 = N\frac{B_0\gamma^2 h^2}{4kT}\,. \qquad [2.8]$$

The equilibrium magnetization is directly proportional to the main magnetic field strength.

2.1.2 Excitation

Hydrogen, when placed in an external magnetic field, will precess at a frequency

$$\omega_0 = \gamma B_0, \qquad [2.9]$$

which is in the radio transmission part of the spectrum (for H^1at 1.5T, ω_0 = 63.86 MHz and 127.7 MHz at 3T). Resonance will occur if an electromagnetic wave is applied with the same frequency as the precession frequency, and is called radio frequency excitation (RF excitation). The excitation causes the magnetization to change according to

$$\frac{d\mathbf{M}}{dt} = \mathbf{M}\times \gamma\mathbf{B} \qquad [2.10]$$

where

$$\mathbf{M} = \begin{pmatrix} M_x \\ M_y \\ M_z \end{pmatrix} \qquad [2.11]$$

and

$$\mathbf{B} = \begin{pmatrix} \boldsymbol{B_1}\mathbf{cos}(\boldsymbol{\omega_0 t}) \\ \boldsymbol{B_1}\mathbf{sin}(\boldsymbol{\omega_0 t}) \\ \boldsymbol{B_0} \end{pmatrix} \qquad [2.12]$$

(3). When this excitation is performed the magnetization tips into the transverse plane, which allows a signal to be received by receiver coils on the same frequency.

2.1.3 Relaxation

After excitation the spins will relax back to their longitudinal magnetization along the direction of the static external field. There are two relaxation mechanisms, spin-lattice or longitudinal relaxation, and spin-spin or transverse relaxation. Both of these relaxations need to be taken in to account when determining magnetization and thus Bloch added this to the magnetization equation to make

$$\frac{d\mathbf{M}}{dt} = \mathbf{M}\times \gamma\mathbf{B} + \begin{pmatrix} -\frac{\boldsymbol{M_x}}{\boldsymbol{T_2}} \\ -\frac{\boldsymbol{M_y}}{\boldsymbol{T_2}} \\ \frac{\boldsymbol{M_0} - \boldsymbol{M_z}}{\boldsymbol{T_1}} \end{pmatrix}, \qquad [2.13]$$

where T_1 is the longitudinal relaxation term and T_2 is the transverse relaxation time (4).

Spin-lattice relaxation is the relaxation that occurs in the longitudinal or Mz direction, as shown in Figure 2.1. After excitation the magnetization will recover along the direction of the static magnetic field in an attempt to return to thermal equilibrium. The relaxation time, or T1 value, is a time constant specific to individual tissues, which characterizes the rate at which the exponential recovery occurs along the Mz direction.

Spin-spin relaxation is the decay along the direction perpendicular, or xy direction, to the static magnetic field. This relaxation is the result of the interactions of the molecules within their own unique microenvironment. These interactions cause the excited spins to dephase and the net magnetization in the xy direction will be zero, as can be seen in Figure 2.2. This dephasing is characterized by a time constant T2, which specifies the expected time that the tranverse magnetization will decay to approximately 34% of the original magnetization. In practical terms, the transverse relaxation occurs at a faster rate due to inhomogeneities in the effective field homogeneity, and this faster relaxation is characterized by the relaxation time T2*. This field inhomogeneity comes from inhomogeneities in the static magnetic field, as well as susceptibility differences, which cause dephasing to occur more quickly. The observed T2 relaxation, or the effective T2 relaxation, can be determined through

$$\frac{1}{T_2{}^*} = \frac{1}{T_2} + \frac{1}{T_{2i}}, \qquad [2.14]$$

where $T_2{}^*$ is the combination of the effect of T_2 and T_{2i}, which is the effective field inhomogeneity. Some sequences are T2* weighted, while others are able to be weighted according to T2, and will be discussed later.

2.2 Image Contrast and Techniques

2.2.1 Image Contrast

There are multiple ways in which contrast between different structures and tissues can be obtained. When acquiring images, it is possible to specify the repetition time (TR) and the echo time (TE), as can be seen in Figure 2.3, which depending on settings can affect the contrast in the image. There are three main contrasts, or “weightings,” which are clinically relevant: T_1, T_2, and proton density weighted. For the studies performed in this work, each of these image weightings were used.

T_1 weighted images are acquired with a short TR and a short TE, where short is typically considered to be TR and TE << T_1 or T_2, respectively. By acquiring the image with a short TR, the more signal the tissue with shorter T_1

will produce compared to tissues with longer T_1. T_1 values for common bodily tissues can be found in Table 2.1 (5,6). T_1 weighted images were acquired in the abdominopelvic region, which is discussed in Chapter 7.

When trying to obtain T_2 weighted images long TR and TE is used. Long is not generally specified, but is typically considered 3-5x T_1 or T_2, respectively. When imaging for T_2 weight, tissues with longer T_2 will have greater signal. T_2 values for common bodily tissues can be found in Table 2.2 (5,6). Fast spin echo, a T2 weighted acquisition, was used for NC-MRA of the iliac and femoral arteries, which were susceptible to B1+ inhomogeneities, or inhomogeneities in the transmit RF field, which is discussed in greater detail in Chapter 5. Improvements needed are discussed in Chapter 6.

The third most common image weighting is proton density (PD) imaging. PD images are acquired with a long TR and a short TE. When imaged with this weighting the areas that have a higher number of protons will have the greatest signal. PD imaging is an important component for B_1+ mapping, which will be discussed in Chapter 5 in greater depth.

2.2.2 Imaging Techniques

The conventional imaging techniques used in MRI are gradient echo and spin echo imaging. Lately, Steady State of Free Precession (SSFP) techniques have begun to be used in MRI for angiography.

Gradient echo (GRE) imaging is performed by using gradients to form an echo. During the free induction decay, a dephasing gradient is applied, which causes the signal to have an accelerated decay. In order to obtain a signal, the process is reversed, where a rephrasing gradient is applied, the same strength but an opposite polarity, which undoes the dephasing that was applied in the first step, creating an echo. This rephasing gradient only refocuses the spins that were dephased by the initial dephasing gradient; it will not affect T2 or T2* processes. During this process only one RF pulse is applied to the sample. This acquisition type is beneficial because when GRE sequences are applied with a low flip angle, then short TR values can be used as well. As a result of short TR and short TE, image acquisition can be rapid. However, due to the nature of the acquisition, GRE sequence image contrast is obtained not by true T2 weighting, but rather by T2* weighting. As a result of this dependence on T2*, GRE sequences are affected by susceptibility, chemical shift artifacts, and also homogeneity issues.

Spin echo (SE) relies on the refocusing of the transverse magnetization through the application of an RF pulse to put the spins in the transverse plane. After a period of time, t, a 180° refocusing pulse is applied. After time t has passed following the refocusing pulse, the nonmoving spins reconverge and a signal echo is formed. Just as with gradient echo imaging, T1 and T2 effects are not corrected for. There is also no correction for phase shifts, or flow. It is possible, if the T2 for the tissue in question is long enough for multiple signal echoes to be formed by repeating the refocusing pulse, to acquire a chain of signals. SE imaging uses an RF pulse for refocusing the spins, where GRE sequences refocus using gradients, so B1 inhomogeneities can cause problems with this acquisition type.

Steady state imaging is done when TR << T2 < T1. When acquiring steady state signal, the transverse signal does not completely decay before the next signal is acquired. This creates a signal that is both T1 and T2 weighted. It is referred to as steady state imaging because the magnetizations, transverse and longitudinal, reach a steady state. One specific steady state method is balanced SSFP (b-SSFP), since the gradients being applied are balanced, which causes the net gradient per TR to be zero, as shown in Figure 2.4, which prevents the magnetization from dephasing. The steady state magnetization of b-SSFP acquisition can be written as

$$bSSFP \simeq M_0 \sin(\alpha) \frac{1}{\left(\frac{T1}{T2}\right)(1-\cos(\alpha)) + (1+\cos(\alpha))} e^{-\frac{TE}{T2}} \qquad [2.15]$$

where α is the flip angle. Of note is the T1/T2 factor in the denominator. This indicates that b-SSFP contrast is actually T2/T1 weighted when the flip angle is near 90°.

One of the advantages of the b-SSFP readout for NC-MRA techniques is that blood signal is bright due to the high T2/T1 weighting, but fat signal needs to be taken into consideration as well due to its high T2/T1 ratio. B-SSFP imaging also benefits from the fresh blood flowing into the imaging slice, and can also be done rapidly, which is beneficial for patient comfort and image quality.

B-SSFP is highly susceptible to off-resonance effects. If there are B0 inhomogeneites, the off-resonance effects are typically presented through a banding artifact. Since B0 inhomogeneities increase with increasing field strength, b-SSFP imaging can become more challenging at higher field strength (≥3T). Improving B0 homogeneity and minimizing TR can be used to minimize these artifacts.

2.3 MRI Hardware

MR scanners are categorized in many different ways. There are low-field systems (< 1.0T), high-field systems (1.0T to 3.0T) and lately ultra-high-field systems (> 3.0T) have begun to be commercially available. Open-bore systems utilize a permanent magnet which is typically in a horseshoe shape, and are typically in the low-field range. High-field and ultra-high-field systems are closed bore systems where a superconducting solenoid creates a stable homogenous magnetic field. Superconducting properties of the solenoid are maintained through the use of a liquid helium cooling system. MRI hardware structure for a superconducting closed bore magnet can be seen in Figure 2.5.

Gradient coils are loops of wire, or thin conductive sheets that are just inside the bore of the scanner. These loops, or sheets, can have a current passed through them, which will create a magnetic field. This gradient field distorts the main magnetic field and allows for localization of signal. There are three sets of these gradient coils, one for each of the x-, y-, and z-directions, which can be applied independently or together.

In addition to the main magnetic field coil and gradient coil, there are also RF coils. These coils are responsible for the transmission of the RF field which perturbs the spins, and also for the reception of the signals from the perturbed spins. For transmission, the B_1 field is produced through current being passed through specific RF-transmit coils. This rotating magnetic field is perpendicular to the direction of the main magnetic field, and when applied near the Larmor frequency of the spins being imaged, deposits energy in to the system. Coils used to receive the signal from the excited spins are placed on the body in the area that is being imaged. Different receive coils exist to try improve the visualization of the specific body parts being imaged. Specialty coils, such as 32 channel cardiac coils, are expensive and not available at all scanners but can improve image quality, whereas standard coils, such as the 8-channel flex coil, are readily available and good for general purpose imaging.

Shimming is a method of correction that is used to correct the homogeneity of the magnet once the magnet is placed on site. There are two ways in which a homogeneous B0 is achieved: passive and active shimming. Passive shimming involves the introduction of ferromagnetic materials within the bore of the magnet, with many iterations required before the desired homogeneity is achieved. Active shimming uses specialized shimming coils to create a corrective magnetic field. Active shimming requires a prescan field map, which determines unwanted spherical harmonics, and an equal and opposite spherical harmonic is created by the active shim coils. The superposition of these two spherical harmonics corrects the inhomogeneity. Active advanced shimming was performed for the studies performed at 3T in order to ensure a homogeneous B0 for experimentation.

2.4 Summary

Improvements to MRI require understanding the physics and the associated mechanical principles related to the NMR effect. The improvements that increasing B_0 can have on imaging, by increasing the signal, and impacting the T_1 values in tissue, but also by affecting the Larmor frequency which causes an impact on the excitation, will be discussed further in Chapter 5. When performing imaging, hardware considerations must be taken into account, and by not relying primarily on specialized, expensive equipment, access to MRI imaging can be improved.

2.5 References

1. Bloch F. Nuclear induction. Physical Review 1946;70:460.
2. Purcell EM, Torrey H, Pound RV. Resonance absorption by nuclear magnetic moments in a solid. Physical Review 1946;69:37.
3. Slichter CP. Principles of magnetic resonance: Springer Science & Business Media; 2013.
4. Hahn EL. Felix Bloch and magnetic resonance. Bull Mag Reson 1985;7:82-89.
5. Stanisz GJ, Odrobina EE, Pun J, Escaravage M, Graham SJ, Bronskill MJ, Henkelman RM. T1, T2 relaxation and magnetization transfer in tissue at 3T. Magn Reson Med 2005;54:507-512.
6. de Bazelaire CM, Duhamel GD, Rofsky NM, Alsop DC. MR imaging relaxation times of abdominal and pelvic tissues measured in vivo at 3.0 T: preliminary results. Radiology 2004;230:652-659.

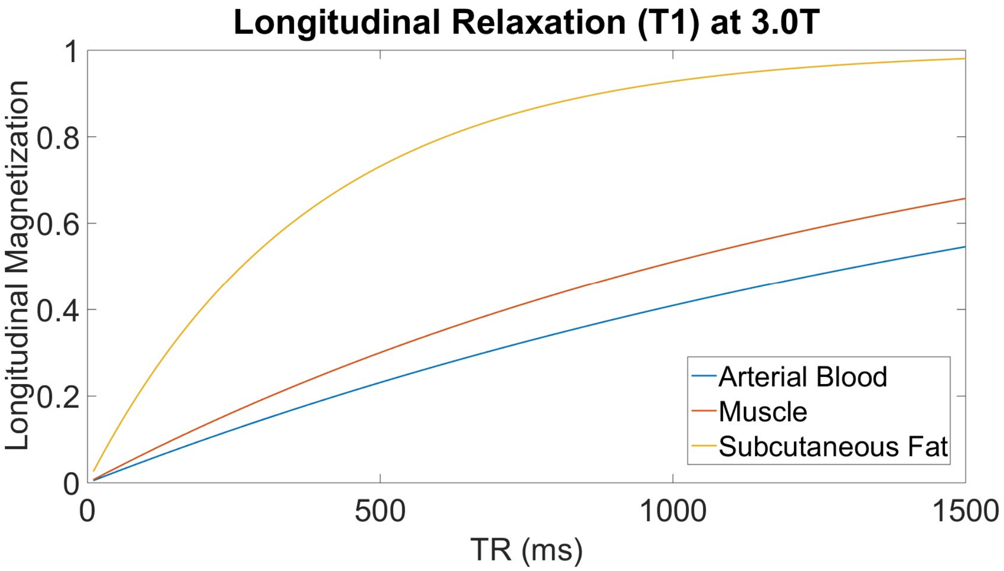

Figure 2.1: T1 relaxation for common tissues that need to be accounted for in NC-MRA.

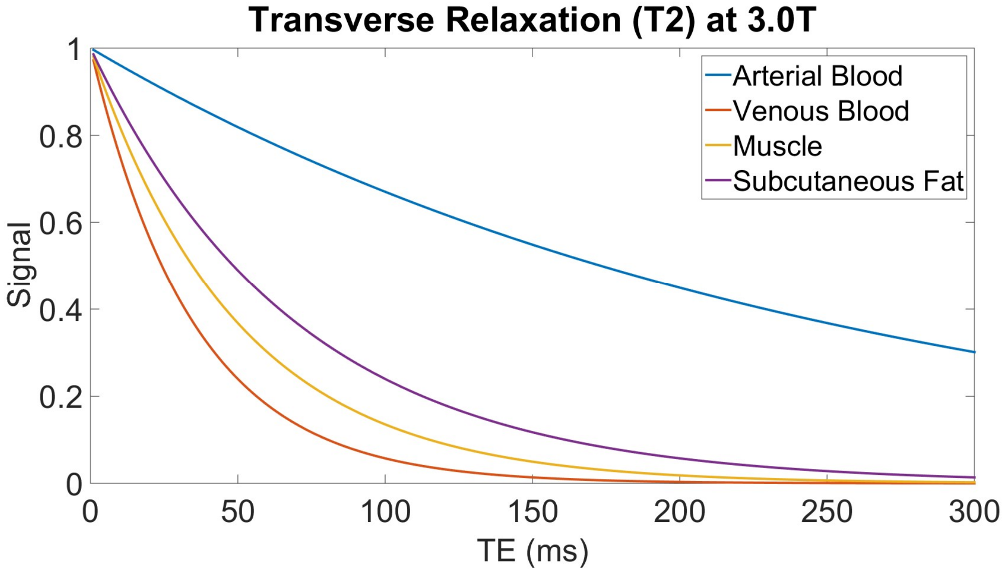

Figure 2.2: T2 relaxation for common tissues that need to be accounted for in NC-MRA.

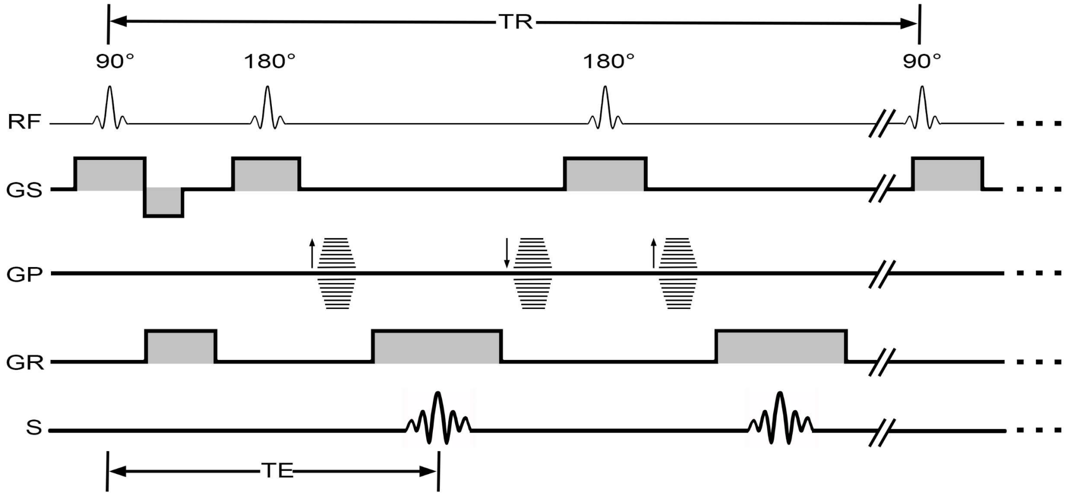

Figure 2.3: Representative pulse sequence diagram showing repetition time (TR), and echo time (TE).

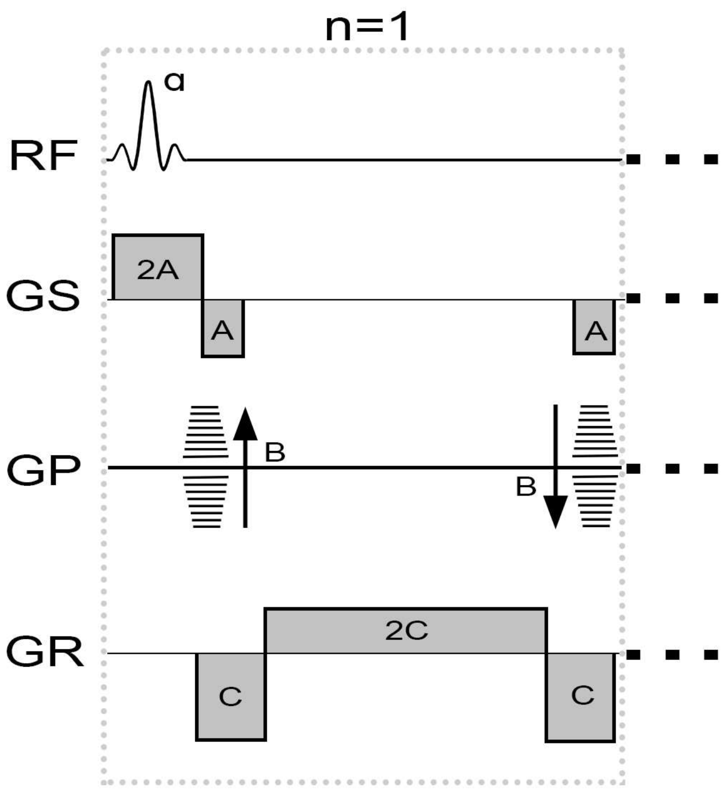

Figure 2.4: Representative pulse sequence diagram showing a balanced steady state of free precession (b-SSFP) readout, which can be repeated n number of times.

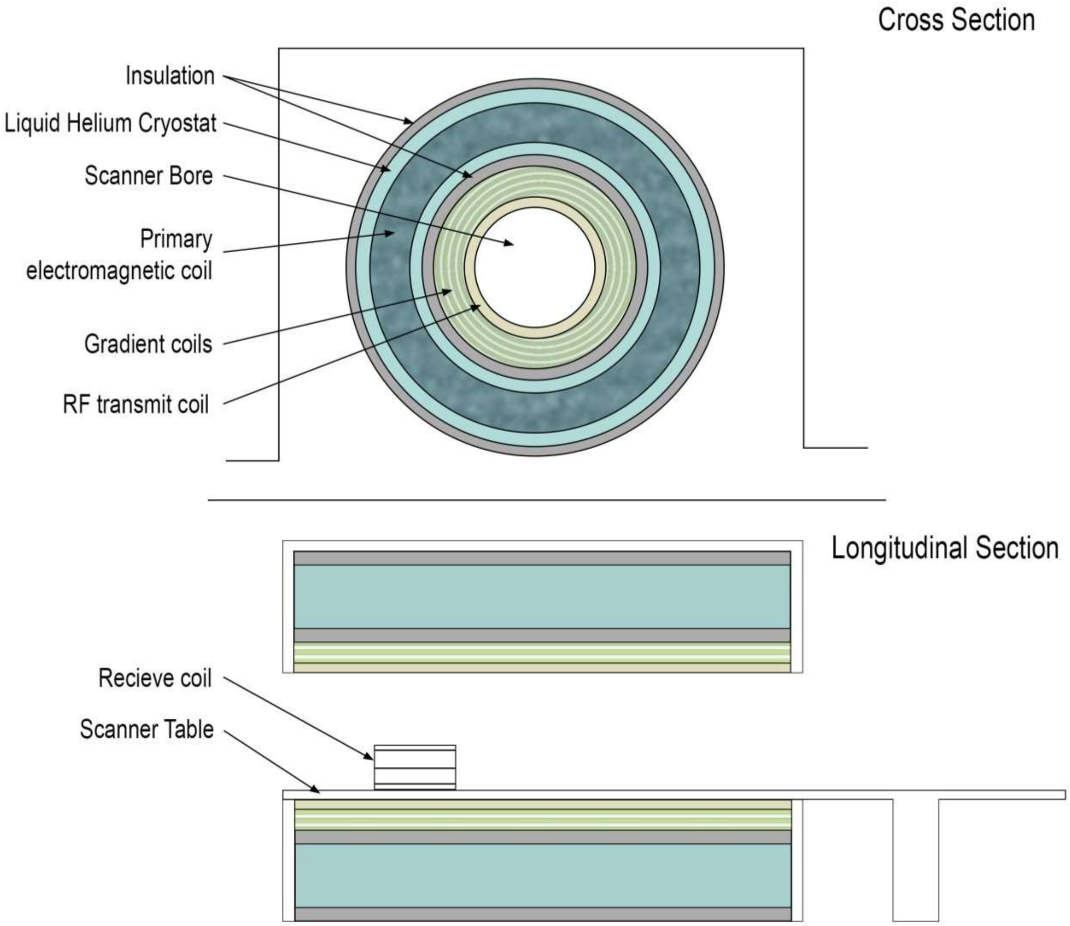

Figure 2.5: Visual representation of clinical MR scanners.Cross-section of a representative superconducting closed bore MRI scanner, showing location of primary coil, gradient coils, transmit coil, and passive shimming. Longitudinal section is also shown which demonstrates the positioning of the table and receive coils in the system. The object to be scanned is placed in the scanner bore with the area to be imaged placed near the scanners midpoint (isocenter).

Table 2.1: T1 relaxation times for common body tissues at 1.5T and 3T (5,6).

T1 Relaxation Time (msec)*

Tissue	1.5 T	3.0 T
Kidney	690 ± 30	1194 ± 27
Liver	576 ± 30	810 ± 64
Subcutaneous fat	343 ± 37	382 ± 13
Blood	1441 ± 120	1932 ± 85
Heart	1030 ± 34	1471 ± 31
Skeletal muscle	1008 ±20	1412 ± 13
Spinal cord	745 ± 37	993 ± 47

Table 2.2: T2 relaxation times for common body tissues at 1.5T and 3T (5,6).

T2 Relaxation Time (msec)*

Tissue	1.5 T	3.0 T
Kidney	55 ± 3	56 ± 4
Liver	46 ± 6	42 ± 3
Subcutaneous fat	58 ± 4	68 ± 4
Blood	290 ± 30	275 ± 50
Heart	40 ± 6	47 ± 11
Skeletal muscle	44 ± 6	50 ± 4
Spinal cord	74 ± 6	78 ± 2

CHAPTER 3

NONCONTRAST MAGNETIC RESONANCE TECHNIQUES

Angiographic techniques that are used to image vasculature using MRI are grouped in the category of Magnetic Resonance Angiography (MRA). MRA images can be used in the diagnosis and treatment of diseases due to the ability to image vessel narrowing (stenosis), vessel dilation (aneurysms), complete blockages (occlusions), and the presence of blood clots.

MRA can be performed with gadolinium contrast agents, CE-MRA, or without using contrast agents, NC-MRA. There are several recently developed techniques for NC-MRA that aim to show contrast between arterial and background signals. The main NC-MRA techniques are: (1) flow-dependent techniques, like time-of-flight, phase contrast, or subtraction based techniques; and (2) flow-independent techniques, like T2 prepared acquisitions. Several of these will be covered in this work, but discussion of every noncontrast technique is beyond the scope of this work.

3.1 Common Approaches

3.1.1 Gadolinium Enhanced MRA

The use of gadolinium-based contrast agents is the current standard of care for MRA, because they are effective at creating signal contrast in the vessels and tissues that they are in. When using gadolinium contrast agents it is necessary to image while the contrast agent is in the vessels before it has perfused into the extracellular space to obtain the optimal contrast. Gadolinium in its free ion form is considered to be somewhat toxic, and so is chelated to protect tissues from that toxicity.

Gadolinium is a paramagnetic material with seven unpaired electrons, which when placed in an external magnetic field creates magnetic dipoles. Unpaired electrons produce a stronger magnetic field than nuclei do, and fluctuate around the nuclei. Since a fluctuating magnetic field is necessary to relax spins, the unpaired electrons will produce a magnetic field at a frequency that is close to the Larmor frequency of hydrogen protons. The magnetic field will perturb due to the large fluctuating magnetic fields. These large fluctuating magnetic fields close to the Larmor frequency will result in the significant shortening of the longitudinal relaxation time, or the T1 of the surrounding molecules will be greatly reduced. The effect depends on the concentration of the gadolinium contrast agent in the area being imaged, and the effect on the T1 value can be determined from

$$\frac{1}{T_{1obs}} = \frac{1}{T_{1t}} + \frac{1}{T_{1c}} \qquad [3.1]$$

and the value for T1C can be determined by $\frac{1}{T_{1c}} = r_1[C]$, where [C] is the concentration of the gadolinium contrast agent.

Gadolinium contrast is an effective tool in MRI due to the change that it has on spin-lattice relaxation rates. It has been used not only in MRA, but also when imaging scar tissue infiltration (late gadolinium enhancement), diffusion rates in tissue, and several other diagnostic tools. Gadolinium also has been linked to nephrogenic systemic fibrosis for individuals with impaired renal function, and gadolinium deposits have even been observed in the brains of individuals with normal renal function, so care needs to be taken when gadolinium contrast is used, and methods that do not require gadolinium contrast agents to obtain diagnostic quality images are important.

There are two methods used to acquire CE-MRA, and the preferred method depends on the gadolinium contrast media that is used. The most commonly used method is a first pass method that uses a gadolinium contrast agent that perfuses into the extracellular space as it passes. This method requires precise timing to ensure that the contrast has not perfused into the extracellular space, thus preventing proper visualization of the vessels. In addition, contamination from veins in lower extremities can occur if the contrast agent has begun to return to the heart through the veins (1-6).

Recently gadolinium contrast media which remains in the bloodpool or in the blood vessels, intravascular contrast, has been developed and used in CE-MRA. Since the contrast does not enter the extracellular space but remains in the vasculature, other than some leakage with albumin-binding contrast agent (7-9), it is possible to use a lower dose of the contrast agent, and also to extend imaging beyond the short arterial first pass phase. This allows for the acquisition of steady state images. Steady state imaging allows for a longer acquisition time, which allows for the acquisition of higher resolution images. Steady state imaging will result in some venous contamination, but due to the higher resolution of the images discerning the difference between veins and arteries is possible (3,10-12). There are problems with availability of these agents due to the manufacturer for Ablavar (an albumin-binding contrast agent) halting production, and ferumoxytol (an agent around 30 nm large) obtaining a boxed warning from the FDA (13).

3.1.2 Time of Flight

Time of flight (TOF) MRA has been around since the 1980s and is one of the most commonly used noncontrast angiographic techniques. Even though it has recently been displaced, this bright blood imaging technique is still important for noncontrast neurovascular and peripheral angiography (14,15). When imaging using TOF, repeated excitations are performed over the slice or volume to be imaged. These repeated excitations have the effect of saturating the protons in the stationary tissues that surround the vessels in question. Fresh blood flowing into the slice or volume of interest has protons which have not been saturated and thus will have a high initial magnetization. Since both arterial and venous blood is fresh flowing into the region of interest, typically a tracking saturation pulse is used to nullify inflowing venous blood. Maximum enhancement of vessels occurs when vessels are perpendicular to the imaging plane, and thus TOF is somewhat insensitive to in-plane flow, which can lead to pseudostenosis (16). When imaging in 3D, TOF imaging has a limited slab thickness, due to the need for fresh unsaturated blood to reach the region for this bright blood signal to be received (17).

Clinically, the most common application for TOF imaging is in the imaging of the intracranial vessels (18-21). 2D TOF was the standard for peripheral angiography prior to the use of contrast agents to obtain bright blood images.

CE-MRA has largely replaced TOF imaging because TOF has longer acquisition times and creates pseudostenosis due to saturation of in-plane vessels.

3.1.3 Phase Contrast

Stationary and moving spins exhibit different reactions when exposed to bipolar magnetic field gradients, which is the basis for phase contrast imaging. A bipolar gradient is created by a gradient being applied in one direction for a period of time, then switching to the opposite direction, with the same amplitude, for the same period of time. The net accrual of phase for stationary spins when a bipolar gradient is applied is zero, but spins that are moving along the direction of the gradient will develop a nonzero phase. This nonzero phase is proportional to the velocity with which the spins are moving in the direction of the applied gradient.

This phase accumulation is not visible on magnitude images, but rather through the subtraction of an image obtained using a positive bipolar gradient and then an image using a negative bipolar gradient. The signal from the stationary spins when these two images are subtracted is canceled, but the signal from the moving spins is additive, which creates the angiogram (22,23).

The use of phase contrast is important in this work because to determine the timing used in ECG-gated FSE imaging it is necessary to determine the time for systolic and diastolic phases. When imaging in the thigh and calf regions it is necessary to run a phase contrast scout to determine at what time the maximal flow occurred.

3.2 Novel Approaches

3.2.1 ECG-gated 3D Partial-Fourier Fast Spin Echo Sequence

Initially introduced in 1985 by Wedeen et al. (24), ECG-gate FSE MRA is one of the more popular noncontrast MRA techniques, with all major MRI vendors having it as a commercially available product. The sequence is gated, or begins image acquisition, based off readings acquired from the ECG readings the system is receiving. The feasibility of the acquisition was improved with the replacement of the spin-echo acquisition with a partial-Fourier FSE acquisition, by Miyazaki et al. (25). This method takes advantage of the fact that during the systolic and diastolic cardiac phases the flow velocity in the arteries changes. During the systolic phase there is signal loss in the arteries due to the dephasing of the spins due to the fast flow. In diastole the blood is slower moving and thus dephasing is not observed. Venous blood travels at a more consistent velocity regardless of cardiac phase. When two images are acquired, one in systole, and the other diastole, a subtraction can be done, which since the background tissue and venous blood exhibit similar signal regardless of cardiac phase they will cancel, leaving a bright arterial blood signal, as seen in Figure 3.1.

This method relies heavily on signal differences between the two acquisitions, which relies on transmit flip angles to be applied consistently across the volume of interest. Nonuniformity of the transmit radio frequency (B_1^+) field can cause the actual flip angle in tissue to be different from the prescribed or nominal flip angle. The B_1^+ inhomogeneity tends to become more severe for higher field strengths, and at 3 Tesla, noticeable B_1^+ variation in different parts of the body has been observed by many studies (26-28), and will be discussed in detail in Chapter 6. The flip angle variation can be anywhere from 30 - 50%. Therefore, careful consideration of the B_1^+ inhomogeneity is important to the imaging of areas that are affected by this inhomogeneity. When trying to develop ECG-gated FSE NC-MRA it was observed that this inhomogeneity was distributed in a radial pattern, with the lowest flip angles being on the right femoral artery of the pelvis when the patient was placed feet first supine into the bore of the MRI. The effect of this B_1^+ inhomogeneity was a signal loss in the subtracted images which were used for the bright blood angiography.

3.2.2 Quiescent-Interval Single-Shot

Quiescent-Interval Single-Shot (QISS) imaging is an ECG-gated technique that has been shown effective in patients at 1.5T (29) with acquisition timing shown in Figure 3.2. After a delay from the cardiac R-wave a slice-selective saturation RF pulse is applied to the slice that is to be imaged. This is then followed with a tracking saturation pulse that is used to nullify the signal from the inflowing venous blood. After the application of the caudal RF pulse there is a quiescent interval, which coincides approximately with the time when blood is flowing most rapidly through the arteries, where no RF pulses are applied. Prior to image acquisition, a chemical shift-selective fat saturation RF pulse is applied to nullify fat signal within the imaging slice. Once all preparatory RF pulses are applied, image acquisition is performed using a single-shot two-dimensional balanced steady-state of free precession during the diastolic phase when the arterial blood is moving slowest, or has stopped.

3.2.3 Quadruple Inversion Recovery

The use of inversion recovery pulse with 3D balanced steady state of free precession readout NC-MRA has been developed and used for the evaluation of the renal arteries, and has even been validated in patients who have been diagnosed with renal artery stenosis (30-33). A recent development in NC-MRA was use of quadruple inversion recovery RF pulses (34,35) to minimize background signal and extend arterial imaging coverage. This sequence begins with a nonselective inversion recovery RF pulse. The nonselective IR pulse will invert all of the spins ($-M_0$) in the tissues in the MRI. The NS-IR pulse is followed immediately by a slice-selective IR (SS-IR) pulse which is positioned so that it will cover the abdominal aorta, as shown in Figure 3.3. This SS-IR acts to reinvert the spins which are contained within the slice, so their magnetization is M_0. A predetermined period of time later another SS-IR pulse is applied distal to the imaging volume. This IR pulse is used to null fresh spins from the inflowing veins.

3.2.4 T2 Prepared MRA

As previously discussed, there is a T2 difference between arterial blood and other tissues. This difference can be exploited to acquire angiographic images that suppress the myocardial tissue and venous blood. T2 preparation begins through the application of a 90° pulse that tips the magnetization into the transverse plane where dephasing begins, then a series of 180° pulses are applied to rephase the magnetization. After a prescribed period of time a -90° is applied to return the magnetization to the z-axis. Due to the T2 differences in the tissues there will be a difference in the magnetizations of the tissues, with arterial signal being highest, as seen in Figure 3.4. When used in conjunction with SSFP readout it is possible to obtain high quality noncontrast MRA images. The use of this sequence is limited in scope due to its susceptibility to inhomogeneities in the transmit field.

3.3 References

1. Prince MR. Gadolinium-enhanced MR aortography. Radiology 1994;191:155-164.

2. Prince MR, Yucel EK, Kaufman JA, Harrison DC, Geller SC. Dynamic gadolinium-enhanced three-dimensional abdominal MR arteriography. J Magn Reson Imaging 1993;3:877-881.

3. Nielsen YW, Thomsen HS. Contrast-enhanced peripheral MRA: technique and contrast agents. Acta Radiol 2012;53:769-777.

4. Kramer H, Zenge M, Schmitt P, Glaser C, Reiser MF, Herrmann KA. Peripheral magnetic resonance angiography (MRA) with continuous table movement at 3.0 T: initial experience compared with step-by-step MRA. Invest Radiol 2008;43:627-634.

5. Kruger DG, Riederer SJ, Grimm RC, Rossman PJ. Continuously moving table data acquisition method for long FOV contrast-enhanced MRA and whole-body MRI. Magn Reson Med 2002;47:224-231.

6. Vogt FM, Zenge MO, Ladd ME, Herborn CU, Brauck K, Luboldt W, Barkhausen J, Quick HH. Peripheral vascular disease: comparison of continuous MR angiography and conventional MR angiography--pilot study. Radiology 2007;243:229-238.

7. Phinikaridou A, Andia ME, Protti A, Indermuehle A, Shah A, Smith A, Warley A, Botnar RM. Noninvasive magnetic resonance imaging

evaluation of endothelial permeability in murine atherosclerosis using an albumin-binding contrast agent. Circulation 2012;126:707-719.

8. Phinikaridou A, Andia ME, Passacquale G, Ferro A, Botnar RM. Noninvasive MRI monitoring of the effect of interventions on endothelial permeability in murine atherosclerosis using an albumin-binding contrast agent. J Am Heart Assoc 2013;2:e000402.

9. Habets J, Zandvoort HJ, Moll FL, Bartels LW, Vonken EP, van Herwaarden JA, Leiner T. Magnetic resonance imaging with a weak albumin binding contrast agent can reveal additional endoleaks in patients with an enlarging aneurysm after EVAR. Eur J Vasc Endovasc Surg 2015;50:331-340.

10. Goyen M. Gadofosveset-enhanced magnetic resonance angiography. Vasc Health Risk Manag 2008;4:1-9.

11. Hartmann M, Wiethoff AJ, Hentrich HR, Rohrer M. Initial imaging recommendations for Vasovist angiography. Eur Radiol 2006;16 Suppl 2:B15-23.

12. Nikolaou K, Kramer H, Grosse C, Clevert D, Dietrich O, Hartmann M, Chamberlin P, Assmann S, Reiser MF, Schoenberg SO. High-spatial-resolution multistation MR angiography with parallel imaging and blood pool contrast agent: initial experience. Radiology 2006;241:861-872.

13. US FDA. FDA Drug Safety Communication: FDA strengthens warnings and changes prescribing instructions to decrease the risk of serious allergic reactions with anemia drug Feraheme (ferumoxytol). 2015.

14. Miyazaki M, Lee VS. Nonenhanced MR angiography. Radiology 2008;248:20-43.

15. McRobbie DW, Moore EA, Graves MJ, Prince MR. MRI from Picture to Proton: Cambridge University Press; 2007.

16. Hoey ET, Ganeshan A, Puni R, Henderson J, Crowe PM. Fresh blood imaging of the peripheral vasculature: an emerging unenhanced MR technique. AJR Am J Roentgenol 2010;195:1444-1448.

17. Lim R, Shapiro M, Wang E, Law M, Babb J, Rueff L, Jacob J, Kim S, Carson R, Mulholland T. 3D time-resolved MR angiography (MRA) of the carotid arteries with time-resolved imaging with stochastic trajectories: comparison with 3D contrast-enhanced Bolus-Chase MRA and 3D time-of-flight MRA. Am J Neuroradiol 2008;29:1847-1854.

18. Nael K, Villablanca JP, Saleh R, Pope W, Nael A, Laub G, Finn JP. Contrast-enhanced MR angiography at 3T in the evaluation of intracranial aneurysms: a comparison with time-of-flight MR angiography. Am J Neuroradiol 2006;27:2118-2121.

19. Sprengers ME, Schaafsma JD, van Rooij WJ, van den Berg R, Rinkel GJ, Akkerman EM, Ferns SP, Majoie CB. Evaluation of the occlusion status of coiled intracranial aneurysms with MR angiography at 3T: is contrast enhancement necessary? AJNR Am J Neuroradiol 2009;30:1665-1671.

20. Pierot L, Delcourt C, Bouquigny F, Breidt D, Feuillet B, Lanoix O, Gallas S. Follow-up of intracranial aneurysms selectively treated with coils: Prospective evaluation of contrast-enhanced MR angiography. AJNR Am J Neuroradiol 2006;27:744-749.

21. Ozsarlak O, Van Goethem JW, Maes M, Parizel PM. MR angiography of the intracranial vessels: technical aspects and clinical applications. Neuroradiology 2004;46:955-972.

22. Gedroyc W, Neerhut P, Negus R, Palmer A, Al Kutoubi A, Taube D, Hulme B. Magnetic resonance angiography of renal artery stenosis. Clin Radiol 1995;50:436-439.

23. Kodoma T, Suzuki Y, Yano T, Watanabe K, Ueda T, Asada K. Phase-contrast MRA in the evaluation of EC-IC bypass patency. Clin Radiol 1995;50:459-465.

24. Wedeen VJ, Meuli RA, Edelman RR, Geller SC, Frank LR, Brady TJ, Rosen BR. Projective imaging of pulsatile flow with magnetic resonance. Science 1985;230:946-948.

25. Miyazaki M, Sugiura S, Tateishi F, Wada H, Kassai Y, Abe H. Non-contrast-enhanced MR angiography using 3D ECG-synchronized half-Fourier fast spin echo. J Magn Reson Imaging 2000;12:776-783.

26. Storey P, Lee V, Sodickson D, Santoro D, Zhang B, Lim R, Atanasova I, Stoffel D, Chen Q, Wiggins G. B1 inhomogeneity in the thigh at 3T and implications for peripheral vascular imaging. In Proceedings of the 17th Annual Meeting of ISMRM, Honolulu, Hawaii, USA, 2009. p 425.

27. Bottomley PA, Andrew ER. RF magnetic field penetration, phase shift and power dissipation in biological tissue: implications for NMR imaging. Phys Med Biol 1978;23:630-643.

28. Glover GH, Hayes CE, Pelc NJ, Edelstein WA, Mueller OM, Hart HR, Hardy CJ, O'Donnell M, Barber WD. Comparison of linear and circular

polarization for magnetic resonance imaging. J Magn Reson 1985;64:255-270.

29. Edelman RR, Sheehan JJ, Dunkle E, Schindler N, Carr J, Koktzoglou I. Quiescent-interval single-shot unenhanced magnetic resonance angiography of peripheral vascular disease: Technical considerations and clinical feasibility. Magn Reson Med 2010;63:951-958.

30. Glockner JF, Takahashi N, Kawashima A, Woodrum DA, Stanley DW, Takei N, Miyoshi M, Sun W. Non-contrast renal artery MRA using an inflow inversion recovery steady state free precession technique (Inhance): comparison with 3D contrast-enhanced MRA. J Magn Reson Imaging 2010;31:1411-1418.

31. Wyttenbach R, Braghetti A, Wyss M, Alerci M, Briner L, Santini P, Cozzi L, Di Valentino M, Katoh M, Marone C, Vock P, Gallino A. Renal artery assessment with nonenhanced steady-state free precession versus contrast-enhanced MR angiography. Radiology 2007;245:186-195.

32. Maki JH, Wilson GJ, Eubank WB, Glickerman DJ, Millan JA, Hoogeveen RM. Navigator-gated MR angiography of the renal arteries: a potential screening tool for renal artery stenosis. Am J Roentgenol 2007;188:W540-546.

33. Katoh M, Buecker A, Stuber M, Gunther RW, Spuentrup E. Free-breathing renal MR angiography with steady-state free-precession (SSFP) and slab-selective spin inversion: initial results. Kidney Int 2004;66:1272-1278.

34. Atanasova IP, Lim RP, Chandarana H, Storey P, Bruno MT, Kim D, Lee VS. Quadruple inversion-recovery b-SSFP MRA of the abdomen: initial clinical validation. Eur J Radiol 2014;83:1612-1619.

35. Atanasova IP, Kim D, Lim RP, Storey P, Kim S, Guo H, Lee VS. Noncontrast MR angiography for comprehensive assessment of abdominopelvic arteries using quadruple inversion-recovery preconditioning and 3D balanced steady-state free precession imaging. J Magn Reson Imaging 2011;33:1430-1439.

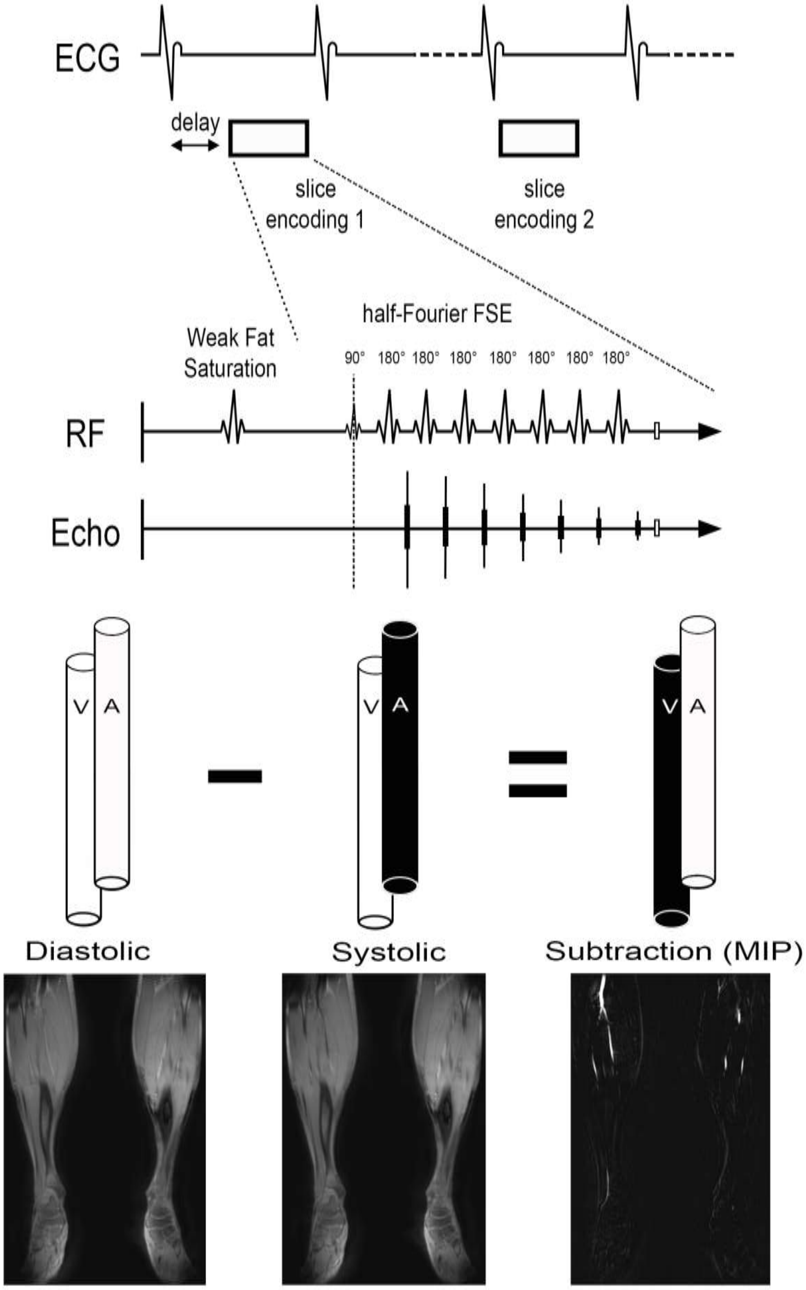

Figure 3.1: Representative timing and acquisition of ECG-gated noncontrast MRA using fast-spin echo acquisition. Due to the flow dephasing that occurs in the arteries during the systolic phase, there is a signal void in the arteries, which when subtracted from a baseline image acquired during the diastolic phase when the arterial blood is moving slowly or is stationary, allows for a bright blood signal to be acquired.

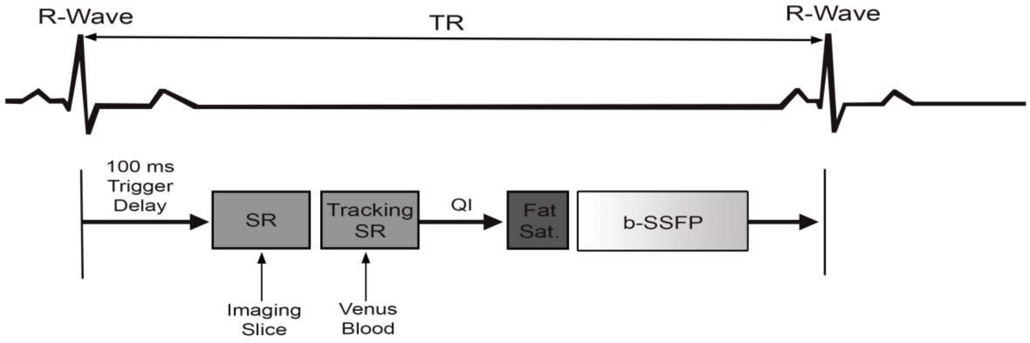

Figure 3.2: Representation of the quiescent interval single shot noncontrast MRA acquisition. After a short delay, two saturation recovery pulses are applied to null the imaging slice and the inflowing venous blood. Imaging is performed after another interval, the quiescent interval, with a fat saturation pulse and b-SSFP readout.

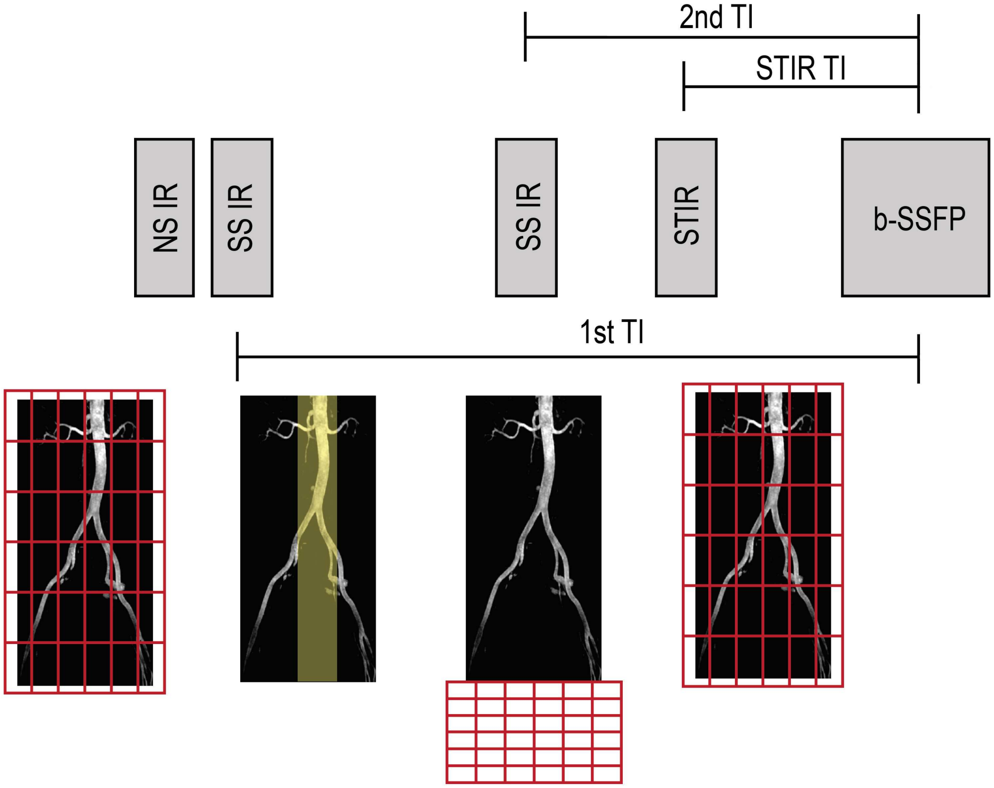

Figure 3.3: Representative structure and timing for QIR NC-MRA. Nonselective inversion recovery pulse is applied, followed immediately by a slice-selective inversion recovery pulse, which is positioned over the aorta to reinvert arterial spins in the aorta. Another slice-selective inversion recovery pulse is applied which nulls fresh inflowing venous blood. Before readout a short tau inversion recovery pulse is applied to nullify fat signal which can contaminate image quality. Readout is balanced steady-state of free-precession

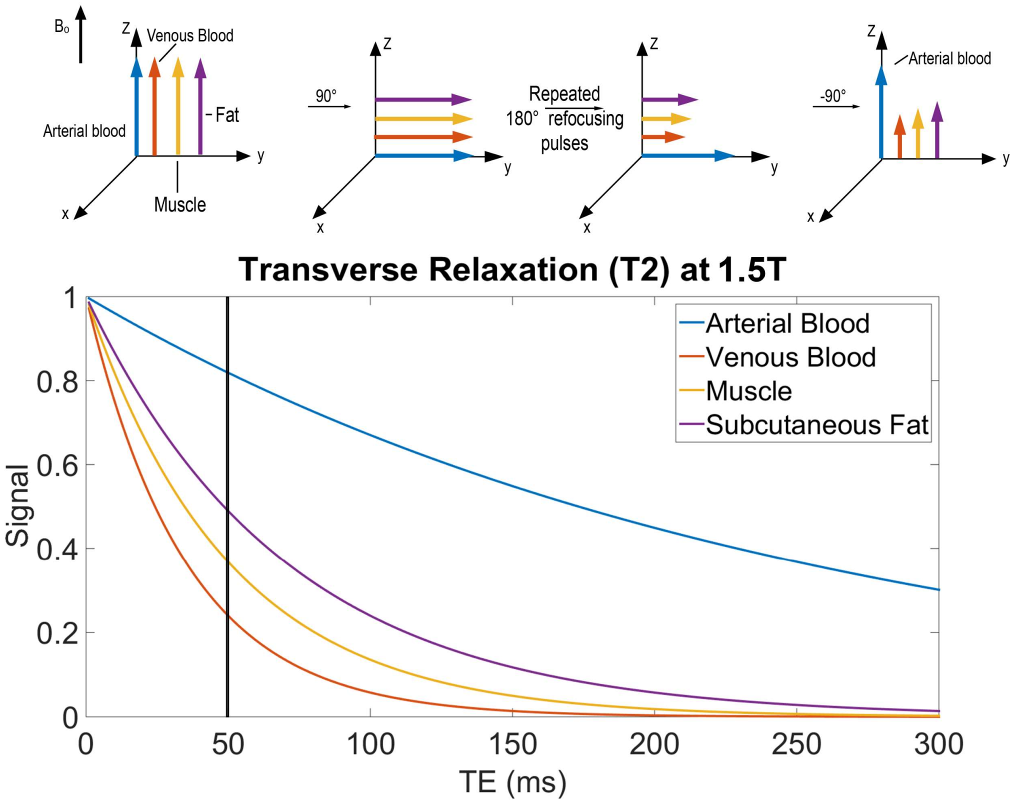

Figure 3.4: Example of the differences in T2 relaxation shows the signal difference that can be acquired through the use of T2 preparation. When the signal is allowed to decay according to T2 before being retipped in the z-axis, there will be significant signal differences between tissues and arterial blood.

CHAPTER 4

K-SPACE SAMPLING AND COMPRESSED SENSING

4.1 Sampling

In general, if an RF pulse is applied to a sample at the resonance or Larmor frequency the whole volume will be excited. In order to localize the locations of the spins to create an image, gradients must be applied. These gradients create a linear variation in the longitudinal magnetic field that is dependent on spatial position. This variation in the magnetic field will cause a change in the resonance frequency of the magnetization that is proportional to the gradient field. The acceleration of image acquisitions an understanding of k-space sampling is necessary to show the impact different acceleration techniques will have on image quality. With the application of the gradients, the MR system is able to encode the spatial information by superimposing the gradient fields. As previously shown, with the resonance frequency occurring at

$$\omega_0 = \gamma B_0, \tag{4.1}$$

upon the introduction of the gradient fields, the frequency will vary in space according to

$$\omega_0 = \gamma(B_0 + G_x x) \tag{4.2}$$

(in the x-direction). As a result of this applied gradient, the spins at positive x positions will precess faster, while spins at negative x positions will precess slower.

Spatial encoding of the spins through the use of the gradient creates a mixture of signals that are received by the MRI. This signal received by the MRI is related to the magnetization distribution through Fourier analysis, and can be analyzed through the signal equation,

$$s(t) = \int_R m(r) e^{-i2\pi k(t) r} dr, \qquad [4.3]$$

which is the signal that the receiver coils receives integrated over the entire volume imaged assuming the reception field is homogeneous. This equation is also referred to as the signal equation for MRI. It shows that the received signal is the Fourier transform of the sampled object m(r) at the spatial frequency, k(t). This differs from traditional optical imaging where the actual pixel samples are directly measured.

The method of acquisition is determined by the use of the gradients in conjunction with the applied RF pulses, or the pulse sequence. When applied, the integral of the gradient waveform will trace a k(t) trajectory in k-space, or spatial frequency space. The encoding pattern, or k-space trajectory, that is chosen is important in the acquisition of images in MRI. There are different times when the gradients can be applied that will allow for this spatial encoding.

4.1.1 Slice or Slab Selection

The first gradient that is typically applied is the slice (2D) or slab (3D) selective gradient. As has been discussed previously, excitation occurs when an

RF pulse is applied to the sample at the resonance frequency. Without any gradients being applied, when an RF pulse is applied at the resonance frequency the whole volume inside the scanner will be excited, and is referred to as a nonselective excitation. In order to selectively excite specific regions, a magnetic gradient is applied perpendicular to the desired slice plane. This magnetic gradient adds to the static magnetic field B_0 and, as a result, the spins will precess at different rates. An RF pulse, when applied at the same time as the magnetic gradient, will only excite those spins which are at the same frequency, so only the spins at the specific slice, or volume, will have a shift in their magnetization. The spins which are located outside of the region of interest experience no excitation and they will not emit any signal. The RF pulse does not only have one frequency, as this would require an infinitely long duration, it will cover a certain bandwidth, which is dependent on the shape and duration of the RF pulse being applied. If desired, it is possible to adjust the thickness of the region being excited, by adjusting the bandwidth of the RF pulse, and/or the amplitude of the slice selective gradient. These are related to each other through

$$\Delta F = \gamma * G_{ss} * \Delta z, \qquad [4.4]$$

where ΔF is the bandwidth of the RF pulse, G_{ss} is the amplitude of the slice select gradient, and Δz is the thickness. The z-direction is used here for simplicity, but slice selection can occur along any dimension.

4.1.2 Phase Encoding

With the appropriate slice selected, further gradients are necessary in order to localize the signal to a particular voxel, since all of the spins in the excited slice will contribute to the overall signal. After slice selection occurs, there is frequently a phase encoding gradient that is applied. This causes a change in the resonant frequencies of the spins while the gradient is being applied. Before the readout of the signals is performed, a gradient is applied for a period of time and then turned off. This causes the spins to precess at different rates when the gradient is on, but the spins will return to precess at the same rate as the other spins once the gradient is off. The period of time when the gradient is applied will cause the spins to have gained or lost phase relative to a reference state, even though they return to the same resonance frequency after the gradient is turned off. Therefore, the spins will precess at the same frequency but the spins will be in different phases. The total phase shift that the spins has undergone is

$$\Phi = \gamma * G * t, \qquad [4.5]$$

where t is the total time that the gradient was applied, G is the amplitude of the gradient, and Φ is the phase shift that the spins have after the phase encoding step has been done.

4.1.3 Frequency Encoding

In order to localize in plane, it is necessary to apply another gradient so the location of the protons being imaged can be localized to a particular voxel within the slice. If attempting to localize in the x-direction, for example, a gradient that varies linearly along the x-axis would be applied. The effective magnetic field *B(x)* along the x-direction would then be

$$B(x) = B_0 + x * G_x \tag{4.6}$$

where B_0 is the main magnetic field, x is the position along the x-axis, and G_x is the frequency encoding gradient. This effective magnetic field will affect the resonant frequency, so that it also varies linearly along the x-axis,

$$f(x) = \gamma * B(x) = \gamma B_0 + \gamma * x * G_x = f_0 + f_g(x), \tag{4.7}$$

where f_0 is the Larmor frequency from the main magnetic field, and $f_g(x)$ is the frequency offset. Since the frequency encoding gradient is being applied while the signal is being received, this frequency data is included. When imaging, pixels have a finite width, and thus each pixel will have a range of frequencies, and not a single frequency. This range of frequencies contained in a single pixel is called the per pixel bandwidth.

4.1.4 Resolution and Field of View

When sampling k-space, discrete points are sampled, which in an idealized situation would be an infinite number of acquired k-space samples. For practical considerations, however, it is only necessary to obtain a finite number of samples. For simplicity we will consider a two-dimensional symmetric case where $FOV_x = FOV_y = FOV$ and the pixel width is also symmetric, or $\Delta x = \Delta y = \Delta w$, where Δw is the pixel width. The total number of samples needed to obtain an image with the desired resolution is determined by the FOV and the pixel width. In relating image space parameters to k-space, there is an inverse relationship between FOV and the spacing between k-space samples, or

$$\Delta k = \frac{1}{FOV}, \qquad [4.8]$$

and also between pixel width and the k-space FOV, or

$$\Delta w = \frac{1}{k_{max}} \qquad [4.9]$$

as seen in Figure 4.1.

4.1.5 k-Space Trajectories

There are several different approaches that can be taken when sampling k-space. The most common is sampling k-space in a line-by-line scheme, or a

Cartesian scheme. This sampling pattern allows an inverse Fourier transform to be performed to obtain an image. Many other non-Cartesian-based sampling patterns have been proposed and used, including radial and spiral. Radial sampling is robust to undersampling and to motion, and spiral trajectories have many of the same benefits. Representations of these trajectories can be seen in Figure 4.2.

Non-Cartesian acquisition trajectories have been developed or seen a resurgence lately due to their undersampling, robustness to motion and also their efficiency. Even with the benefits of radial sampling, Cartesian acquisitions are still the most widely used in clinical practice. In order to shorten the acquisition time for thoracic and abdominopelvic NC-MRA, a 3D form of radial sampling is being used: 3D stack of stars with tiny golden angles.

4.1.6 k-Space Undersampling

MRI imaging is performed by traversing multi-dimensional k-space, with the speed of this traveling in k-space being limited by certain restraints. k-Space sampling has been traditionally designed to meet the Nyquist criterion, which is dependent on the FOV and the image resolution. As has been previously discussed the image resolution is dependent on the k-space region, k_{max}, being sampled. The trajectory that k-space is traversed is determined by the gradients applied as described by

$$\Delta k_x = \frac{k_{x,max}}{Matrix_x} = \frac{\gamma * G_x * t}{Matrix_x}. \qquad [4.10]$$

The strength with which the gradients are applied will affect the time required to cover the trajectory, with a higher amplitude gradient meaning a shorter traversal time. There are a couple of restraints to the use of higher amplitude gradients: limits in the gradient systems of current scanners and the effect that they have on the human body. Gradients in current MRI systems are limited by a maximum amplitude and maximum slew-rate, and thus are hardware limited. It has also been shown that the rapid switching of gradients and high gradient amplitudes can cause peripheral nerve stimulation in subjects. For patient safety and comfort this stimulation should be avoided if possible, and thus there is a fundamental limit to gradient system performance, even if hardware limitations are overcome.

Since the speed that k-space samples can be acquired is limited, other methods to accelerate acquisitions have been developed. These methods violate the Nyquist criterion and as a result reconstructed images exhibit aliasing artifacts, but maintain patient safety and comfort and are within the hardware limits. The method by which k-space is undersampled will have an impact on image quality, as seen in Figure 4.3. By acquiring a smaller k_{max} the image resolution is impacted, which can be detrimental to image quality. If uniform undersampling is performed the aliasing artifact created is obviously present. When random undersampling is performed image quality is diminished, but aliasing artifacts are incoherent. These methods aim to reduce these artifacts by generating artifacts that are incoherent and not as obstructive of the image, exploiting redundancy in k-space, or exploiting spatial or temporal redundancy. The methods proposed in this work utilize these approaches to reduce scan time and maintain image quality.

4.2 Radial Sampling

4.2.1 3D Stack-of-Stars

Radial trajectories are robust to motion, and undersampling, due to overlapping in the central part of k-space, there is an averaging effect on motion (1-5). One approach that has been proposed for obtaining 3D data sets using radial trajectories is the use of stack-of-stars. Each kx-ky partition is obtained separately with the radial pattern being acquired for each kx-ky partition to minimize crosstalk between each partition as well as maintaining a consistent T1 weighting. Typical commercially available 3D radial sampling requires an isotropic resolution due to how the k-space sampling occurs.

Radial sampling requires accuracy from the gradients systems that was not completely possible until a few years ago. The pulse sequence proposed and used in this thesis is the 3D radial stack of stars, which samples in the kx-ky partition with radial readout sampling, and Cartesian slice encoding in the kz direction. The underlying pulse sequences are based on a balanced steady state of free precession readout, with different preparation schemes.

The readout sampling in radial acquisitions is achieved by rotating the Cartesian readout direction by some defined rotation matrix, for example in the x-direction:

$$R_\theta = \begin{pmatrix} \cos(\theta) & -\sin(\theta) & 0 \\ \sin(\theta) & \cos(\theta) & 0 \\ 0 & 0 & 1 \end{pmatrix} \qquad [4.11]$$

where θ is the angle of rotation for each line of k-space. The gradient can then be obtained through

$$G_{RO,\theta} = R_\theta G_{RO} = \begin{pmatrix} G_x \cos(\theta) \\ G_x \sin(\theta) \\ 0 \end{pmatrix}. \qquad [4.12]$$

These equations demonstrate that unlike in Cartesian sampling where the readout gradient is applied along only one direction, the readout for radial sampling is applied in both the x- and y-directions simultaneously. The individual gradient strength is then determined based upon the original gradient strength and then weighted using sine and cosine with the angle of the acquisition.

The angles used for the acquisition can be arbitrarily chosen, but some angles are preferred over other angles. The most commonly used sampling types are uniform sampling, golden angle sampling, and, recently, tiny golden angle sampling. In each case the angle change from one acquisition to the next is constant.

Uniform sampling evenly distributes the acquisitions or rays uniformly over the range of [0, π], where the angular increment between each acquisition is determined by the total number of rays acquired and can be expressed by $\Delta\theta = \frac{\pi}{N}$ where N is the number of rays acquired. This acquisition method has the benefit that the rays are evenly distributed across the acquisition range, and allows for acquisitions in incremental order, or interleaving the rays. It also allows for rays to be acquired with the orientation of the ray flipped, by increasing the angle by π, which can improve the robustness to off-resonance effects.

Golden angle acquisitions use an angular increment $\Delta\theta = \theta_a$, where θ_a is the golden angle,

$$\theta_a = \frac{180^{\circ}}{\frac{1+\sqrt{5}}{2}} \approx 111.24^{\circ}. \qquad [4.13]$$

Using an angle increment at the golden angle has several advantages which have been shown: self-interleaving, approximate uniform distribution, including any subsequent set of rays, no ray is acquired twice, and when time is a dimension the number of rays used can be retrospectively selected. When golden angle is used for the incremental step, each new spoke closes the largest gap between the previous spokes. This enables an even distribution of readout rays regardless of the number of rays that are acquired, which makes the golden angle increment an ideal acquisition pattern for dynamic acquisitions. When acquiring dynamic images, it is possible to “rebin” the rays into temporal frames, and by using the golden angle pattern, regardless of the number of rays that were acquired, there will be an even distribution of rays in the slice.

In order to improve the effectiveness of the constrained reconstruction for 3D imaging, the incoherent artifacts need to appear in different patterns in different slices. When acquiring using Cartesian sampling, this is accomplished through random distribution of the sampling pattern. When acquiring 3D radial stack-of-stars, it is common for the sampling pattern to be repeated for each kx-ky partition. If the sampling is done in this way, the streaking artifacts will be repeated on each slice, which will minimize the effectiveness of the reconstruction method being used. This can be avoided by rotating the sampling pattern being used so that the rays do not overlap. To avoid that problem in this work the projection angles were rotated by the next golden angle increment from the previous ray. This allowed for the artifact in adjacent slices to have a different structure.

Due to the large angle differences between subsequent rays, there are rapidly changing eddy currents that are created in the conducting part of the magnet. Due to the nature of b-SSFP readout, and its need for homogeneity in the field, as discussed in Chapter 2, these eddy currents can exhibit strong signal fluctuations. In order to still gain the advantages of the irrationality of the use of golden angles, an irrational angular increment based on the golden angle has been proposed. This angle measure takes smaller steps between each successive ray which minimizes the creation of eddy currents.

$$\psi_N = \frac{\pi}{\frac{1+\sqrt{5}}{2} + N - 1}, \qquad [4.14]$$

where N = 1, 2, 3…, where the first two terms are the golden angle and the complementary golden angle. When N > 2 the angles are tiny golden angles, and have the same benefits when used in a radial acquisition when more than 2N samples are acquired. For this work, it was determined that an optimal value for N was 7. Even distribution across k-space can also be seen for the golden angle and tiny golden angle, with N = 7, in Figure 4.4. The separation between the maximum angle and minimum angle between two adjacent rays converges and maintains close proximity in these three radial k-space sampling techniques after a certain number of rays has been acquired, as shown in Figure 4.5.

4.2.2 Non-Cartesian Reconstruction

When dealing with Cartesian sampled acquisitions, reconstructions are simple and straightforward; a simple inverse Fourier transform is all that is necessary. For non-Cartesian sampling, inverse Fourier transform is not an option, but there are several other viable options available, for example resampling, conjugate phase reconstruction, and projection-reconstruction.

Projection reconstruction was the original method used for the reconstruction of MRI images (6,7). This reconstruction technique is very similar to how CT images are reconstructed, and so is accomplished by a filtered back projection of a 1D inverse Fourier transform of each line.

Conjugate phase reconstruction is computationally very intensive as it requires that an integral to be done for each pixel separately (8-10).

Resampling is a method where the non-Cartesian data is sampled as Cartesian data, then the inverse Fourier transform can be applied. The most commonly used resampling method is called gridding. For the radial trajectories that were acquired in these studies, gridding was used with a density compensation for the overlapping central k-space points. In order for the gridding method to be used it is necessary to know the angle that each subsequent acquisition is acquired in relation to the last. A typical gridding algorithm that is used is

$$\widehat{M}(k_x,k_y) = \left[\left(M(k_x,k_y)S(k_x,k_y)w(k_x,k_y)\right) * C(k_x,k_y)\right] \times III\left(\frac{k_x}{\Delta k_x},\frac{k_y}{\Delta k_y}\right) \quad [4.15]$$

where $w(k_x,k_y)$ is the density compensation function, $C(k_x,k_y)$ is the convolution kernel, $S(k_x,k_y)$ is the non-Cartesian sampling function, and $III\left(\frac{k_x}{\Delta k_x},\frac{k_y}{\Delta k_y}\right)$ is the Cartesian grid sampling.

4.3 Constrained Reconstruction

The constrained reconstruction method has been around for decades. There are many different kinds of constraints that have been proposed in the literature, and a discussion of all the different constraints that have been proposed is beyond the scope of this work. For this work we will discuss a few, but focus on the nonlocal means denoising algorithm.

It was originally thought that it was not possible to recover information that was beyond the measurement cutoff frequency. The information is not apparent in the measured data, but by looking elsewhere, these frequencies can in fact be partially restored. Rather than treating the unmeasured data as zeros, which is what conventional Fourier reconstruction aims to do; these constrained approaches instead recover the unmeasured data based on a priori information.

Compressed sensing (CS) while relatively new, promises to mathematically produce accurate signal reconstructions when data is sampled below the Nyquist sampling rate. There are some requirements to the use of compressed sensing modeling.

1. The model being used for CS is sparse in a transform domain. This means that in a certain transform representation that a fully sampled data set should only have a few nonzero coefficients.
2. When undersampling is performed in the measurement domain the artifacts that are created should be incoherent. For this reason, random sampling of k-space is performed, since regular sampling will produce coherent artifacts in the image that are not separable in the sparsity transforms and they cannot be eliminated using CS.

If these conditions are not met then the application of nonlinear reconstruction methods can be used to estimate the image, which is both consistent with the samples that have been measured and represented with a few coefficients can be some nonlinear reconstruction methods. Noncontrast MRA is a candidate for CS due to the sparsity of the data acquired.

Nonlocal means (NLM) denoising is the primary method of constrained reconstruction used for this work. NLM denoising takes advantage of the redundancy in the data that is contained in the image (11-14). Normally in the denoising of natural images, the data contains areas that contain varying textures, or smoothness, that can be used in this algorithm. When using NLM denoising in medical images, some care must be taken because areas of the image might contain similar textures, while having different meanings, and thus should not be used for comparison.

One of the downsides to NLM denoising is that it is computationally demanding and requires significant time for reconstruction due to the comparisons being made across the image (11,14). In order to accelerate the reconstruction using NLM denoising, a 3D method where the comparison is being done in a smaller three-dimensional volume was used (14). It is also possible that the use of the redundancy in the image can introduce artifacts in the clinical images.

Another popular method is the use of a wavelet transform (15-17). The use of a discrete wavelet transform is beneficial because in application it is a sparse representation of the data and can be used to describe local features. Due to the sparsity of the transform, it is possible to filter out most of the noise, while still being able to preserve the fine details, or the high frequency data. The use of a wavelet transform filter was proposed for the conditions where the noise is Rician. It is necessary for the noise variance to be estimated, and is based on the square of the magnitude image that comes from the k-space data.

4.4 Summary

There are many different approaches to sampling k-space. The most common in clinical practice is the use of a Cartesian sampling pattern. Lately a resurgence in non-Cartesian sampling patterns has occurred due to the many potential benefits that non-Cartesian sampling patterns offer in comparison to Cartesian sampling. It was not until recently that non-Cartesian sampling was feasible in a clinical setting due to the need for accurate gradient systems and homogeneities in the fields. With the use of radial sampling specifically, it is possible to accelerate the acquisition and use a constrained reconstruction method to recover the data and produce images with the incoherent artifacts removed.

4.5 References

1. Sarty GE. Single TrAjectory Radial (STAR) imaging. Magn Reson Med 2004;51:445-451.
2. Wundrak S, Paul J, Ulrici J, Hell E, Rasche V. A small surrogate for the golden angle in time-resolved radial MRI based on generalized Fibonacci sequences. IEEE Trans Med Imaging 2015;34:1262-1269.
3. Wundrak S, Paul J, Ulrici J, Hell E, Geibel MA, Bernhardt P, Rottbauer W, Rasche V. Golden ratio sparse MRI using tiny golden angles. Magn Reson Med 2016;75:2372-2378.
4. Winkelmann S, Schaeffter T, Koehler T, Eggers H, Doessel O. An optimal radial profile order based on the Golden Ratio for time-resolved MRI. IEEE Trans Med Imaging 2007;26:68-76.
5. Mistretta CA. Undersampled radial MR acquisition and highly constrained back projection (HYPR) reconstruction: potential medical imaging applications in the post-Nyquist era. J Magn Reson Imaging 2009;29:501-516.
6. Lauterbur PC. Image formation by induced local interactions: examples employing nuclear magnetic resonance. Nature 1973;242:190-191.
7. Glover GH, Pauly JM. Projection reconstruction techniques for reduction of motion effects in MRI. Magn Reson Med 1992;28:275-289.
8. Noll DC, Meyer CH, Pauly JM, Nishimura DG, Macovski A. A homogeneity correction method for magnetic resonance imaging with time-varying gradients. IEEE Trans Med Imaging 1991;10:629-637.
9. Noll DC, Pauly JM, Meyer CH, Nishimura DG, Macovski A. Deblurring for non-2D Fourier transform magnetic resonance imaging. Magn Reson Med

1992;25:319-333.

10. Noll DC, Fessler JA, Sutton BP. Conjugate phase MRI reconstruction with spatially variant sample density correction. IEEE Trans Med Imaging 2005;24:325-336.

11. Manjon JV, Carbonell-Caballero J, Lull JJ, Garcia-Marti G, Marti-Bonmati L, Robles M. MRI denoising using non-local means. Med Image Anal 2008;12:514-523.

12. Manjon JV, Coupe P, Marti-Bonmati L, Collins DL, Robles M. Adaptive non-local means denoising of MR images with spatially varying noise levels. J Magn Reson Imaging 2010;31:192-203.

13. Coupé P, Yger P, Barillot C. Fast non local means denoising for 3D MR images. Medical Image Computing and Computer-Assisted Intervention–MICCAI 2006: Springer; 2006. p 33-40.

14. Tristan-Vega A, Garcia-Perez V, Aja-Fernandez S, Westin CF. Efficient and robust nonlocal means denoising of MR data based on salient features matching. Comput Methods Programs Biomed 2012;105:131-144.

15. Zaroubi S, Goelman G. Complex denoising of MR data via wavelet analysis: application for functional MRI. Magn Reson Imaging 2000;18:59-68.

16. Pizurica A, Wink AM, Vansteenkiste E, Philips W, Roerdink BJ. A review of wavelet denoising in MRI and ultrasound brain imaging. Curr Med Imaging Rev 2006;2:247-260.

17. Anand CS, Sahambi JS. Wavelet domain non-linear filtering for MRI denoising. Magn Reson Imaging 2010;28:842-861.

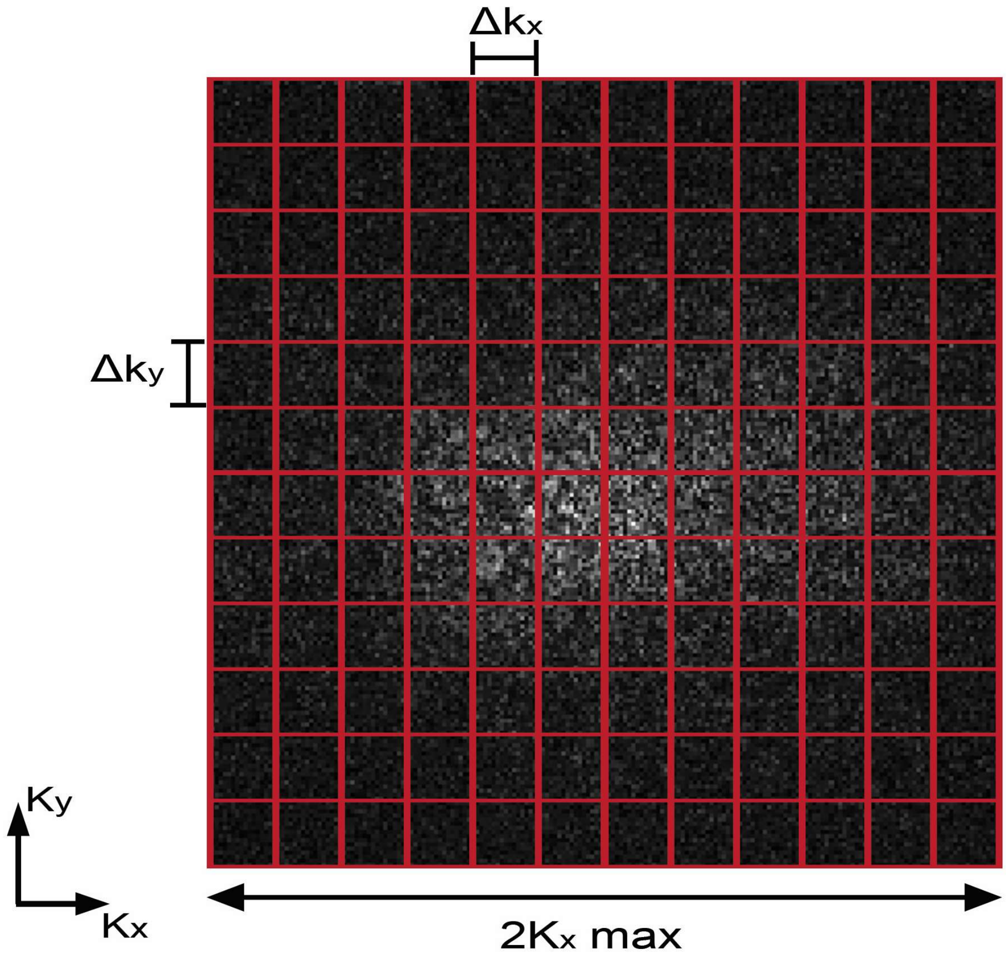

Figure 4.1: Example showing the structure for the sampling of k-space in a Cartesian sampling pattern.

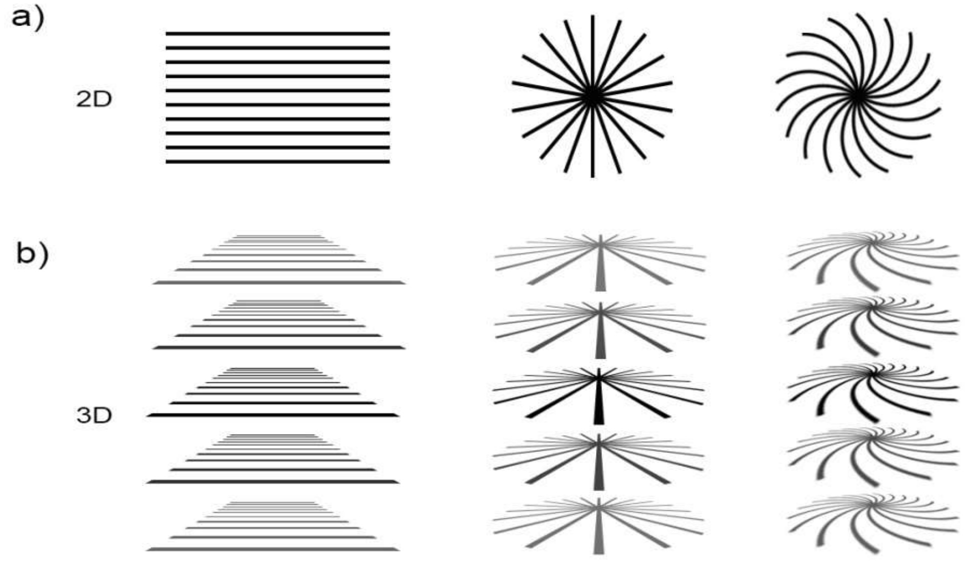

Figure 4.2: Representative common k-space trajectories (a) 2D from left to right: Cartesian, radial, and spiral; and (b) 3D from left to right: Cartesian, stack-of-stars, and stack-of-spirals.

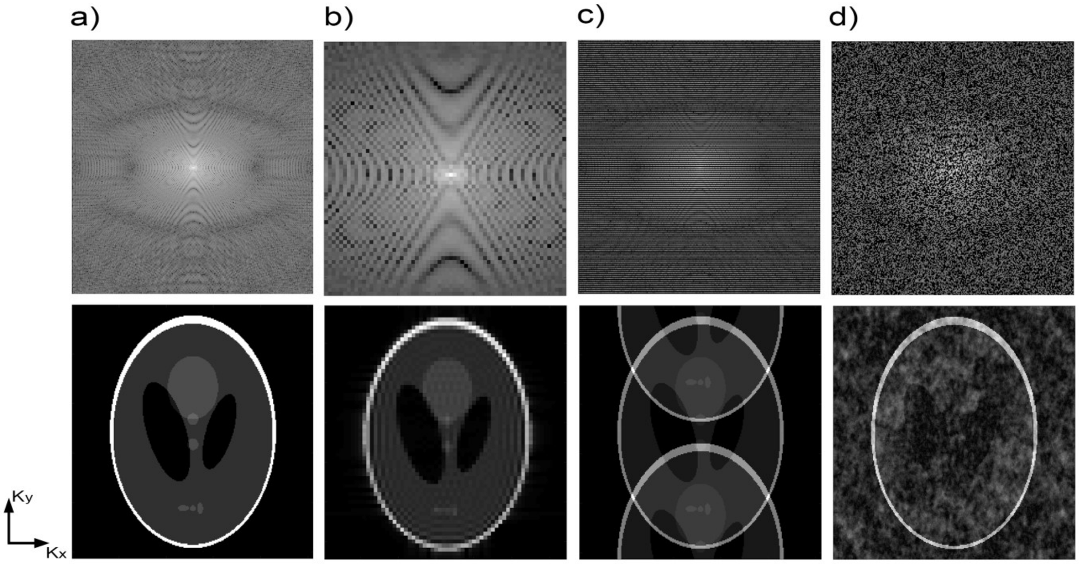

Figure 4.3: Imaging phantom representation of impact of k-space extent and violation of Nyquist criterion. The k-space that was used and the resultant images are shown. A fully sampled image (a) is shown for comparison to a (b) downsampled, (c) equispaced undersampling, and (d) irregular random undersampling. Both (c) and (d) have been undersampled by a factor of 2. It is evident the impact on the resolution from decreasing k_{max}. Coherent folding artifacts are present when sampling is uniform, but incoherent when sampling is randomly distributed.

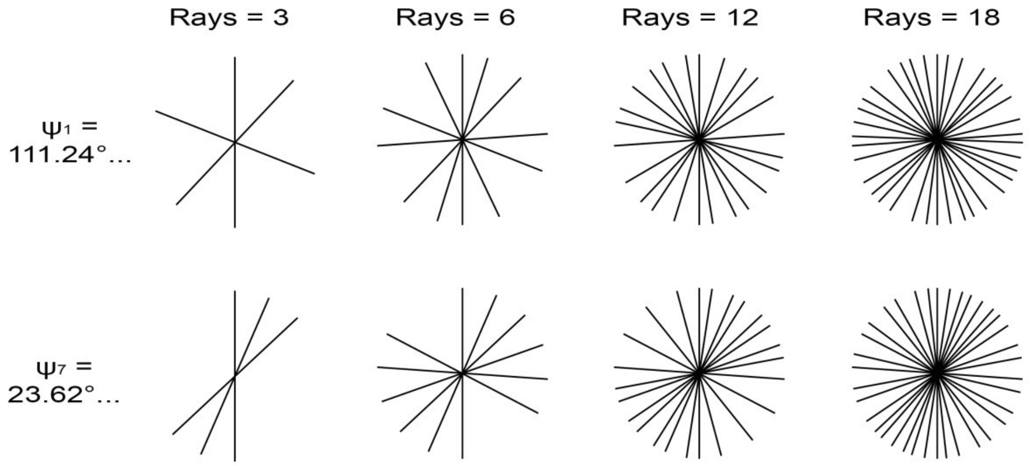

Figure 4.4: Golden angle, ψ1, ordering compared to tiny golden angle, ψ7. Both show comparable radial coverage starting with number of rays 12 or greater.

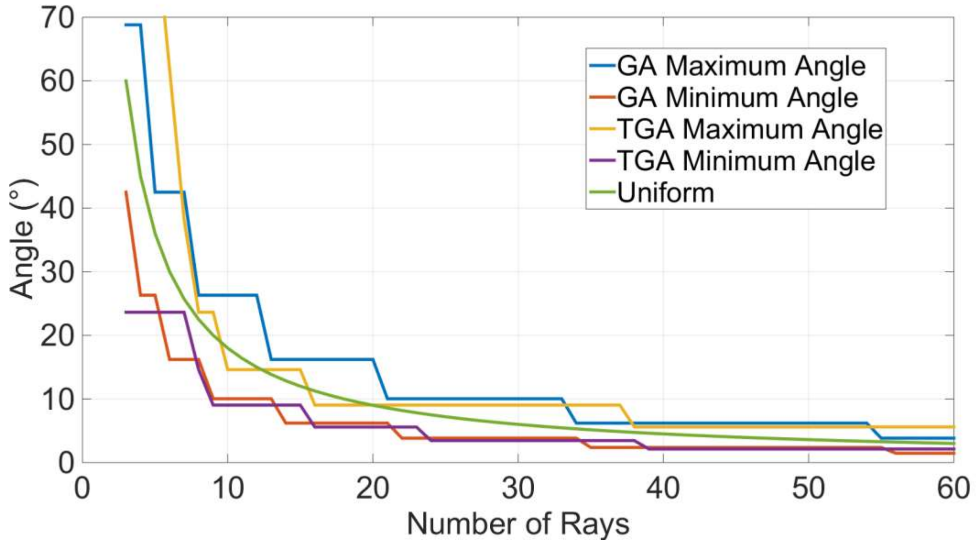

Figure 4.5: A comparison of the angle separation for uniform distribution, and the maximum and minimum angle between adjacent rays for golden angle (GA), and tiny golden angle (TGA) with ψ_7.

CHAPTER 5

RADIOFREQUENCY FIELD

To alter the net magnetization of the spins in the external magnetic field a perturbing field must be applied. This perturbation is an RF field that is applied perpendicular to the direction of the main magnetic field. When the RF field is applied at the appropriate frequency, which is

$$\omega_0 = \gamma B_0, \tag{5.1}$$

resonance will occur. The excitation causes the magnetization to change according to

$$\frac{d\mathbf{M}}{dt} = \mathbf{M} \times \gamma \mathbf{B} \tag{5.2}$$

where

$$\mathbf{M} = \begin{pmatrix} M_x \\ M_y \\ M_z \end{pmatrix} \tag{5.3}$$

and for the case of clinical MRI

$$\mathbf{B} = \begin{pmatrix} \boldsymbol{B_1 \cos(\omega_0 t)} \\ \boldsymbol{B_1 \sin(\omega_0 t)} \\ \boldsymbol{B_0} \end{pmatrix}. \tag{5.4}$$

When this excitation is performed the magnetization will tip depending on the RF pulse that is applied. The application of the RF field for excitation, or B1+, can present challenges in acquisition types due to excess heating or inhomogeneities in B1+.

For transmission, the B_1 field is produced through current being passed through specific RF-transmit coils. This rotating magnetic field is perpendicular to the direction of the main magnetic field, and when applied near the Larmor frequency of the spins being imaged, deposits energy into the system. The B_1 field is typically applied for brief periods of time, usually msec, and thus is called an RF pulse. Early RF coil design used linearly polarized RF pulses, which caused both transmission and reception of electromagnetic waves to be along a single axis. The field oscillating at the resonance frequency can be decomposed into two counter-rotating subfields, one of which rotates with the same frequency and direction as the NMR signal, while the other subfield rotates in the opposite direction and frequency. The subfields which rotate with the same frequency and direction induces a change in the nuclear magnetization, whereas the other subfields only deposit unwanted thermal energy into the body, increasing the Specific Absorption Rate (SAR), as defined below, without signal benefit.

To counter this effect a second set of coils perpendicular to the first, with a phase shift of 90° is introduced, as seen in Figure 5.1. This array of coils creates a circularly polarized B1+ field as shown. Due to the phase shift introduced, the unwanted counter rotating fields are always out of phase with each other and cancel out. The useful subfields are in sync with each other and interact additively to produce the rotating field without depositing unnecessary thermal energy into the body.

When RF coils are used to receive the oscillating magnetic flux from the spins, a current in the coil is induced, which is processed to obtain the frequency and phase information. The signal received by the receiver RF coils is frequently termed B_1-. When receiver coils are arranged in an array, it is possible to use parallel imaging to accelerate acquisitions (1).

5.1 Specific Absorption Rate

In the transmission of radiofrequency waves into the body, RF pulses can deposit energy into the body due to dielectric heating. As previously discussed, the RF pulses applied are dependent on the field strength that is being used, due to the need to produce resonance at the Larmor frequency. On modern MR systems, this frequency can range from 68 MHz to 300 MHZ for whole body systems and up to 400 MHz for head only systems. The plane-wave solutions for these RF pulses are given by

$$E(x,t) = E_1 e^{i(kx-\omega t)} \qquad [5.5]$$

and

$$B(x,t) = B_1 e^{i(kx- \quad)}. \qquad [5.6]$$

When MRI is being performed, due to the location of the patient, the patient is in the “near-field region” and the primary source of effects from the RF is from the magnetic field, with negligible contribution from the electric field. When time-varying magnetic fields are present, electric fields will be induced,

$$\nabla \times E = -\frac{\partial B}{\partial t}, \tag{5.7}$$

according to Maxwell’s equations. When these electrical fields are present in body tissues during B1 excitation, they will drive electrical currents in the tissues, which will heat the tissues, due to dielectric heating. This heating is monitored and must remain within certain limits specified by the Food and Drug Administration and is known as the Specific Absorption Rate (SAR). The value for SAR in practice is approximated as

$$SAR = \frac{\sigma |E|^2}{2\rho}\left(\frac{\tau}{TR}\right) N_p N_s \tag{5.8}$$

where the conductivity is given by σ,the electric field is E, ρ is the tissue density, the pulse duration τ, N_p is the number of pulses, and N_s is the number of slices (2,3). As the frequency of the wave increases, the induced electric field will increase linearly, since from Maxwell’s equations we know that

$$\nabla \times E = iB_1 \omega e^{i(kx-\omega\ )}. \tag{5.9}$$

The SAR equation can be simplified to a proportionality where the

$$SAR \propto \omega^2 B_1^2 \propto \alpha^2 B_0^2. \quad [5.10]$$

At higher field strengths, the SAR value can become a limiting factor if care is not taken when designing and implementing acquisitions.

5.2 Transmit Field Inhomogeneities

As previously stated, the frequency of the RF pulses applied depends on the strength of the main magnetic field, and for clinical systems range from 63.86 MHz to 400 MHz, with 63.86 MHz at 1.5T and 127.7 MHz at 3T being the focus for this work. These frequencies correspond to wavelengths of 4.7 m at 63.86 MHz to 0.75 m at 400 MHz in free space.

The wavelength of the RF pulse in a medium can be simplified for most materials, where the magnetic permeability of the material is close to the magnetic permeability in free space, to a relationship with the materials permittivity,

$$\lambda = \frac{2\pi c}{\omega\sqrt{\varepsilon_r \mu_r}} = \lambda_0 \sqrt{\frac{\varepsilon_0}{\varepsilon'}} \quad [5.11]$$

where ε_r is the permittivity, μ_r is the permeability, and ω is the frequency of the RF pulse. As can be seen, when these RF pulses come in contact with any medium, the human body in the case of MRI, these RF pulses have a shorter wavelength, as seen in Figure 5.2, and the amplitude is attenuated in the medium. In the case of fields > 3T, where the wavelengths are 2.35 m and shorter, the effective wavelength becomes comparable to, or less than, the dimensions of the body, typically being 26 cm and shorter. With the shortened wavelengths standing waves can be created, along with the propagation of the waves. As a result of the creation of standing waves, inhomogeneity in B1+ can result with regions of increased and decreased magnitudes. For lower fields, < 3T, the wavelengths of B1+ are not short enough to create standing waves in the human body, so do not suffer from the same inhomogeneity that is present in higher field strength MRI.

In order to test the inhomogeneities in the field, and determine the best way to correct them, it was necessary to perform a test to show the location and extent of the inhomogeneities. In order to do this test, B1+ maps were acquired. As will discussed in Chapter 6, a previously determined method of B1+ mapping was used, where the use of the slice selective preparatory pulses and the lack of the preparatory pulse were combined in to one sequence with a delay of 10 seconds, to enable the magnetization to relax to equilibrium (4). The method used is shown in Figure 5.3. The relative B_1+ value can be calculated using the following equation

$$\kappa = \frac{\cos^{-1}\left(\frac{SS\ Pre}{PD}\right)}{\alpha^{nom}} \qquad [5.12]$$

which provides a normalized B_1+ map (4).

5.2.1 RF Field Transmit Inhomogeneity Compensation

Methods

Several solutions have been proposed to correct these inhomogeneities in the transmit field. The use of a parallel transmit system is an active process that can be controlled by the user. In normal MR systems the transmit coil is sending a single B1 field, but in a parallel transmit system, the transmit system can be divided into separate and independent controlled elements that will produce their own B1 subfields. When these are summed, the sum B1 will be the net B1 experienced by the tissue. This makes it easier to control the homogeneity of the excitation. Calibration prior to scanning is required to optimize the RF pulses from the individual sources. This transmit method also requires the system to be equipped with a parallel transmit system, which can be very expensive.

A cheaper, passive system that has had success at improving B1 homogeneity is the use of high permittivity padding. One of the common high permittivity materials used in the pads is barium titanate. Barium titanate ($BaTiO_3$) is of the perovskite family. Barium titanate has been shown to have a large dielectric constant at room temperature, with grain size impacting the dielectric constant (5,6). When an EM wave enters a dielectric there is a secondary field that is created, according to Maxwell's equations,

$$\nabla\times B = \mu\boldsymbol{J_c} + \mu\boldsymbol{J_d} = \mu\sigma\boldsymbol{E} + \boldsymbol{i}\mu\varepsilon_r\varepsilon_0\omega\boldsymbol{E} \qquad [5.13]$$

where there are two currents, conductive current and displacement current, that are 90° phase shifted from each other. When plane waves travel through a homogeneous medium, the conductive current decays in the direction of the propagation, while the displacement current acts as a secondary field that facilitates the RF wave propagating through the medium. A ratio showing the contributions to the B1 can be considered

$$\frac{\boldsymbol{J_C}}{\boldsymbol{J_d}} = \frac{\sigma}{\omega\varepsilon_0\varepsilon_r}, \tag{5.14}$$

where it can be seen that materials with a low conductivity and a high permittivity can cause the B1 field in the region near the material to be strengthened due to this secondary field. The use of high permittivity pads has shown improvement in B1 homogeneity at high fields for imaging of the liver, head, and angiographic applications (7-14). The effect of the secondary field will be limited in scope and thus the padding needs to be placed where the effect would be most beneficial. Due to the passive nature of the padding, variability is only attainable by changing the padding (shape, thickness, material) (11). It is necessary to determine optimal pad thickness and location for improving B1+ homogeneity in the region of interest.

5.3 RF Field Summary

The spins must be perturbed, which affects the magnetization of the sample, to create images. This is accomplished through the application of a perturbing magnetization that is applied perpendicular to the main magnetic field, and at the resonance frequency of the spins being imaged. There are practical considerations that need to be taken into account and, if need be, corrected for the SAR and transmit field inhomogeneities. SAR, or the heating of tissues due to the RF field, can be compensated for by timing of the application of the RF pulses, and ensuring proper spacing between subsequent pulses, if needed. Field inhomogeneities are a problem at higher main magnetic field strengths due to the shortening of the wavelength from the medium. This shortening of the wavelength creates standing waves which cause interference and can be corrected through the use of parallel transmit, which requires special MRI hardware, or high permittivity padding, which is a passive tool for correction.

5.4 References

1. Griswold MA, Jakob PM, Heidemann RM, Nittka M, Jellus V, Wang J, Kiefer B, Haase A. Generalized autocalibrating partially parallel acquisitions (GRAPPA). Magn Reson Med 2002;47:1202-1210.

2. Bottomley PA, Redington RW, Edelstein WA, Schenck JF. Estimating radiofrequency power deposition in body NMR imaging. Magn Reson Med 1985;2:336-349.

3. Kanal E, Shellock FG, Talagala L. Safety considerations in MR imaging. Radiology 1990;176:593-606.

4. Chung S, Kim D, Breton E, Axel L. Rapid B1+ mapping using a preconditioning RF pulse with TurboFLASH readout. Magn Reson Med 2010;64:439-446.

5. Kinoshita K, Yamaji A. Grain-size effects on dielectric properties in barium titanate ceramics. J Appl Phys 1976;47:371-373.

6. Arlt G, Hennings D. Dielectric properties of fine-grained barium titanate ceramics. J Appl Phys 1985;58:1619-1625.

7. Yang QX, Rupprecht S, Luo W, Sica C, Herse Z, Wang J, Cao Z, Vesek J,

Lanagan MT, Carluccio G, Ryu YC, Collins CM. Radiofrequency field enhancement with high dielectric constant (HDC) pads in a receive array coil at 3.0T. J Magn Reson Imaging 2013;38:435-440.

8. Teeuwisse WM, Brink WM, Haines KN, Webb AG. Simulations of high permittivity materials for 7 T neuroimaging and evaluation of a new barium titanate-based dielectric. Magn Reson Med 2012;67:912-918.

9. Brink WM, Webb AG. High permittivity pads reduce specific absorption rate, improve B1 homogeneity, and increase contrast-to-noise ratio for functional cardiac MRI at 3 T. Magn Reson Med 2014;71:1632-1640.

10. Yang QX, Wang J, Wang J, Collins CM, Wang C, Smith MB. Reducing SAR and enhancing cerebral signal-to-noise ratio with high permittivity padding at 3 T. Magn Reson Med 2011;65:358-362.

11. Webb AG. Dielectric materials in magnetic resonance. Concept Magn Reson A 2011;38A:148-184.

12. Haines K, Smith NB, Webb AG. New high dielectric constant materials for tailoring the B1+ distribution at high magnetic fields. J Magn Reson 2010;203:323-327.

13. de Heer P, Brink WM, Kooij BJ, Webb AG. Increasing signal homogeneity and image quality in abdominal imaging at 3 T with very high permittivity materials. Magn Reson Med 2012;68:1317-1324.

14. Lindley MD, Kim D, Morrell G, Heilbrun ME, Storey P, Hanrahan CJ, Lee VS. High-permittivity thin dielectric padding improves fresh blood imaging of femoral arteries at 3 T. Invest Radiol 2015;50:101-107.

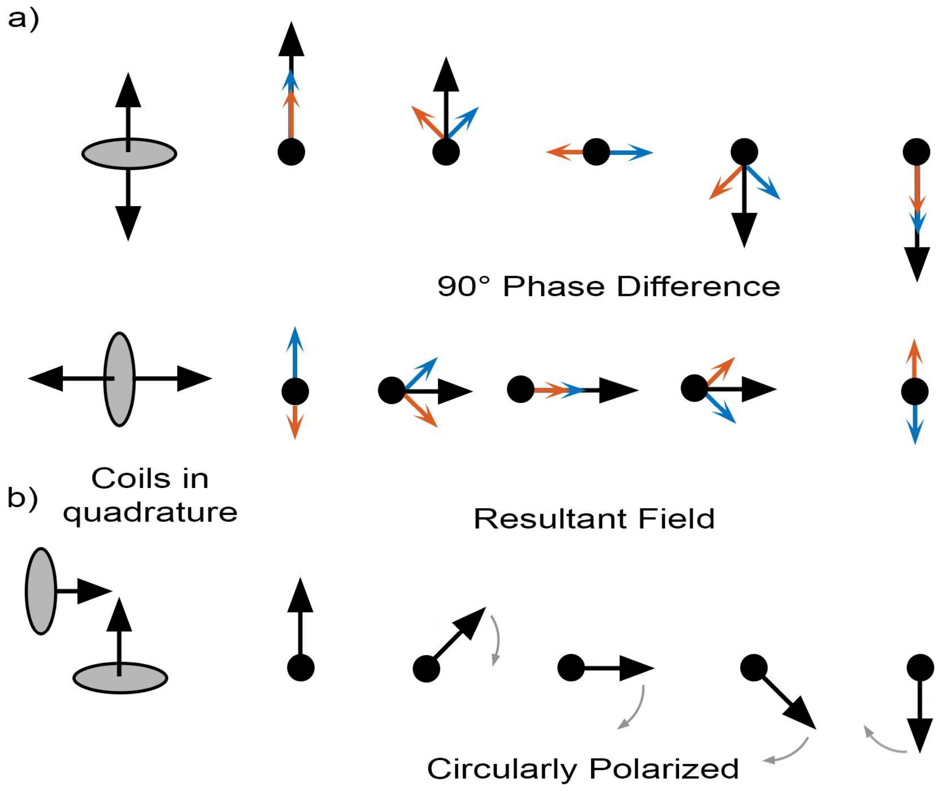

Figure 5.1: Creation of circularly polarized EM fields through the use of quadrature coils. The two coils (a) have a 90° phase difference which cancels one of the subfields resulting in (b) the circular polarized B1 field.

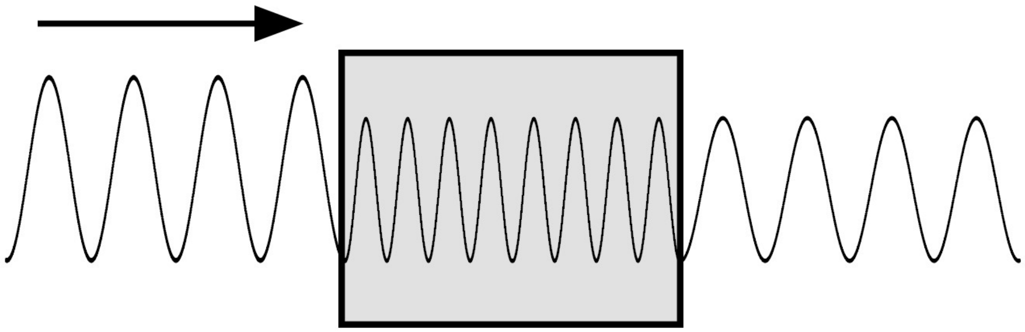

Figure 5.2: When an electromagnetic wave enters a dielectric, the wavelength is decreased and the amplitude is attenuated.

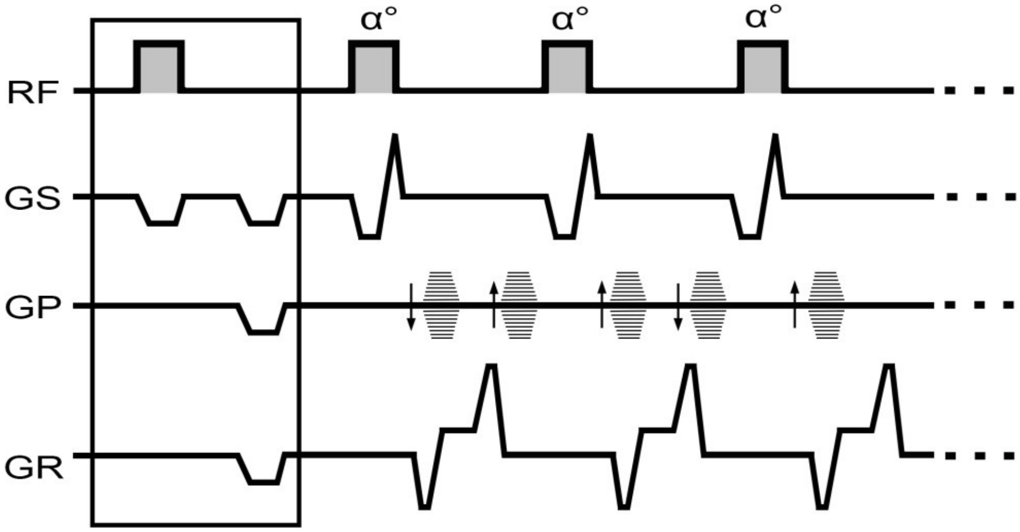

Figure 5.3: Representative pulse sequence diagram showing the preparatory (boxed) step. This sequence is performed in two single shots, once with the preparatory RF pulse and once without, with a delay of ten seconds between each acquisition. Once acquired the resultant images are compared to obtain a normalized B1+ map.

CHAPTER 6

HIGH-PERMITTIVITY THIN DIELECTRIC PADDING IMPROVES FRESH BLOOD IMAGING OF FEMORAL ARTERIES AT 3T

Lindley MD, Kim D, Morrell G, et al. High-Permittivity Thin Dielectric Padding Improves Fresh Blood Imaging of Femoral Arteries at 3T. Investigative radiology. February 2015 - Volume 50 - Issue 2 - p 101.107.
http://journals.lww.com/investigativeradiology/pages/articleviewer.aspx?year=2015&issue=02000&article=00006&type=abstract

TECHNICAL NOTE

High-Permittivity Thin Dielectric Padding Improves Fresh Blood Imaging of Femoral Arteries at 3 T

Marc D. Lindley, BS,*† Daniel Kim, PhD,† Glen Morrell, MD, PhD,†
Marta E. Heilbrun, MD, MS,† Pippa Storey, PhD,‡ Christopher J. Hanrahan, MD, PhD,†
and Vivian S. Lee, MD, PhD, MBA†

Objectives: Fresh blood imaging (FBI) is a useful noncontrast magnetic resonance angiographic (MRA) method for the assessment of peripheral arterial disease, particularly for imaging patients with poor renal function. Compared with 1.5 T, 3 T enables higher signal-to-noise ratio and/or spatiotemporal resolution in FBI. Indeed, previous studies have reported successful FBI of the calf station at 3 T. However, FBI of the thigh station at 3 T has been reported to suffer from signal void in the common femoral artery of 1 thigh only because of the radial symmetry in transmit radiofrequency field (B_1+) variation. We sought to increase the signal of femoral artery in FBI at 3 T using high-permittivity dielectric padding.

Materials and Methods: We performed FBI and B_1+ mapping of the thigh station at 3 T in 13 human subjects to compare the following 3 dielectric padding settings: no padding, commercially available thick (approximately 5 cm) dielectric padding, and high-permittivity thin (approximately 2 cm) dielectric padding. We characterized the radial symmetry in B_1+ variation as well as its impact on the FBI signal at baseline and how dielectric padding improves B_1+ and FBI. We evaluated the quality of 3 FBI MRA acquisitions using quantitative (ie, contrast-to-noise ratio of femoral arteries) and qualitative (ie, conspicuity of femoral arteries) analyses.

Results: With the subjects positioned on the magnetic resonance table in feet-first, supine orientation, the radial symmetry in B_1+ variation attenuates the signal in the right common femoral artery. The signal void can be improved partially with commercial padding and improved further with high-permittivity padding. Averaging the results over the 13 subjects, the mean B_1+, contrast-to-noise ratio, and conspicuity scores for the right common femoral artery were significantly higher with high-permittivity padding than with commercial padding and baseline ($P < 0.001$).

Conclusions: Our study shows that high-permittivity dielectric padding can be used to increase the signal of femoral artery in FBI at 3 T.

Key Words: peripheral arterial disease, noncontrast MRA, dielectric padding, B_1+ inhomogeneity, fresh blood imaging

(*Invest Radiol* 2015;50: 101–107)

Peripheral arterial disease (PAD) is a chronic disease that affects more than 5 million Americans and is projected to affect more than 7 million adults in the United States by the year 2020.[1] Imaging plays an important role in diagnosis and guiding therapy. Contrast-enhanced magnetic resonance angiography (MRA) is clinically indicated as a test for noninvasive diagnosis and evaluation of PAD.[2,3] However, gadolinium-based contrast agents have been associated with nephrogenic systemic fibrosis in patients with renal insufficiency,[4,5] which is a major concern given that approximately 40% of patients with PAD have renal insufficiency.[6]

This safety concern has activated a renewed interest in noncontrast MRA (NC-MRA) methods.[7–10] One such method is fresh blood imaging (FBI), which is based on subtraction of two 3-dimensional fast spin-echo (FSE) acquisitions at 2 different cardiac phases.[9,10] The first FSE scan is acquired during diastole, in which both the arteries and veins appear bright. The second scan is acquired during systole, in which the veins appear bright and the arteries appear dark because of flow-induced signal dephasing. Subtraction of these 2 images cancels the vein and background signals and produces bright-blood angiograms. The FBI of peripheral vasculature has been shown to work effectively for both the thigh and calf stations at 1.5 T.[11–14]

Widening the availability of FBI to all clinical scanners, including 3 T, is important because approximately one third of clinical magnetic resonance (MR) scanners in the United States are 3 T and because 3 T enables higher signal-to-noise ratio and/or spatiotemporal resolution. Indeed, previous studies have reported successful FBI of the calf station at 3 T.[8,15] Our preliminary analysis in a few human subjects indicates that 3 T, as compared with 1.5 T, improves signal-to-noise ratio in the thigh station by approximately 50%. However, FBI of the thigh station at 3 T has been reported to suffer from signal void in the common femoral artery of 1 thigh only because of the radial symmetry in transmit radiofrequency (RF) field (B_1+) variation.[16] Given that this problem is not well understood in the MRA field, in this study, we characterized the radial symmetry in B_1+ variation at baseline and its impact on the FSE signal and FBI MRA.

Several methods are commercially available for compensating B_1+ inhomogeneity, including B_1+ shimming and parallel transmit RF technologies such as Philips *MultiTransmit* (Philips, Eindhoven, The Netherlands) and Siemens *TrueForm* (Siemens Healthcare, Erlangen, Germany). Similar to a typical runoff contrast-enhanced MRA protocol, our multistation (abdomen, thigh, calf) NC-MRA protocol is based on 3-dimensional coronal image acquisitions with head-to-foot coverage on the order of 400 to 500 mm per station. This requirement necessitates a long-bore MR imaging (MRI) system with large effective field of view (eg, Tim Trio; Siemens), which is unfortunately not equipped with the *TrueForm* technology. Therefore, we sought to compensate for B_1+ variation in a long-bore 3-T MRI system using high-permittivity dielectric padding, which has been applied for brain, body, inner ear, and cardiac MRI applications.[17–21] Dielectric padding has a major advantage of being low in cost (approximately $150) when compared with B_1+ shimming and parallel transmit systems, which require expensive hardware. The utility of high-permittivity dielectric padding in FBI of the thigh station at 3 T has not been evaluated until very recently in a preliminary analysis.[22] The objective of this study was to construct and evaluate high-permittivity dielectric padding for increasing the signal of femoral artery in FBI at 3 T.

Received for publication August 1, 2014; and accepted for publication, after revision, August 30, 2014.

From the *Department of Physics, and †Utah Center for Advanced Imaging Research, Department of Radiology, University of Utah, Salt Lake City, UT; and ‡Center for Biomedical Imaging, New York University School of Medicine, New York, NY.

Conflicts of interest and sources of funding: Supported in part by the National Institutes of Health (HL092439; HL116895-01A1).

Presented in part at the Society for Cardiovascular Magnetic Resonance Annual Conference, January 16–19, 2014, New Orleans, LA.

This study is related to the US patent 8,334,691 (ultrafast magnetic resonance imaging method and apparatus for noncontrast agent magnetic resonance angiography using electrocardiograph or pulse-triggered half-Fourier turbo spin echo-based acquisition with variable flip angle evolution and high resolution).

The authors report no conflicts of interest.

Reprints: Marc D. Lindley, BS, Utah Center for Advanced Imaging Research, University of Utah, 729 Arapeen Dr, Salt Lake City, UT 84108. E-mail: marcdlindley@gmail.com.

ISSN: 0020-9996/15/5002–0101

MATERIALS AND METHODS

High-Permittivity Dielectric Pad

High-permittivity pad was constructed using barium titanate (Alfa Aesar, 99%, approximately 325 mesh) and distilled water and was heat-sealed in a polyethylene bag. An approximate ratio of 4:1 by weight (barium titanate to water) was used to achieve the appropriate saturated suspension.[17,20] To evaluate the relative permittivity of the barium titanate mixture compared with a commercial pad, we performed the following simple experiment. Using 2 copper plates (approximately 2 × 2 inches in dimensions), we measured the capacitance of a fixed distance with and without the padding. Using the equation describing the capacitance $C = \varepsilon_r \varepsilon_0 \frac{A}{d}$, where ε_r is the relative permittivity, ε_0 is the electric constant (8.854×10^{-12} F m^{-1}), A is the area of the 2 plates, and d is the distance between the plates. This preliminary analysis showed that the barium titanate pad had approximately 9-fold higher permittivity than commercially available pad did. We elected not to report the absolute value of each pad because an accurate measurement of permittivity requires a more complicated analysis that is beyond the scope of this study.

The barium titanate pad, now referred to as high-permittivity padding throughout this study, was constructed with in-plane dimensions of 38 × 20 cm to cover the right thigh and pelvis following the path of the femoral arteries and within the peripheral RF coil configuration. These pad dimensions and placement were determined empirically on the basis of B_1+ mapping of the thigh and extensive experience with FBI of the thigh station at 3 T. In a preliminary experiment, we compared the performance of 3 different pad thicknesses (1, 2, and 3 cm) in a volunteer to determine an optimal thickness. Our careful visual analysis (Fig. 1, note the more even FBI signal between the left and right common femoral arteries at 2 cm) showed that 2 cm is the optimal pad thickness. Thus, we used the pad size of 38 × 20 × 2 cm (weighing 3.7 kg) throughout this study.

Human Subjects

Nine healthy volunteers (9 males; mean ± standard deviation (SD) age, 33 ± 8 years) and 4 patients (3 males and 1 female; mean ± SD age, 65 ± 13 years) with PAD were imaged with FBI. All subjects were positioned on the MR table in feet-first, supine orientation. This study was compliant with the Health Insurance Portability and Accountability Act and approved by the local institutional review board. Written informed consent was obtained from all subjects.

MRI Experiment

Imaging was performed on a whole-body, long-bore 3-T system (Tim Trio; Siemens Healthcare, Erlangen, Germany; maximum gradient strength, 40 mT/m; slew rate, 200 T/m/s). Radiofrequency excitation was performed using the body coil. For signal reception, body matrix coil array (6 elements available), peripheral coil array (16 elements available), and spine coil array (24 elements available) were used. For the thigh station alone, the number of elements used was 32. For each subject, we performed FBI and rapid B_1+ mapping[23] with 3 different dielectric padding settings: no padding, with commercial padding, and with high-permittivity padding. A commercial dielectric pad (Siemens), 37 × 25 × 5 cm^3, with a weight of 2.9 kg, was compared, with similar pad placement as the custom-made padding (Fig. 2). For consistency, we used similar pad placement for all subjects using the peripheral matrix coil as the marker for positioning the bottom of the padding. Care was taken to ensure that transmit and receive RF calibration settings were identical for the 3 experiments. The magnet isocenter was set consistently at the mid-thigh level for all subjects, as is typically done for our multistation runoff MRA protocol. B_1+ mapping was performed in an axial plane at the common femoral artery level.

Pulse Sequence

Fresh blood imaging of the thigh station was performed using the following relevant imaging parameters: scan time, approximately 4 minutes; field of view, 500 (readout encoding) mm × 425 (phase encoding) mm × 163 to 204 (partition encoding) mm; image acquisition matrix, 320 × 276 × 96 to 120; spatial resolution, 1.3 mm × 1.3 mm × 1.7 mm; repetition time, 1 heart beat based on electrocardiogram; echo time, 22 milliseconds; excitation flip angle, 90 degrees; constant refocusing flip angle, 120 degrees; bandwidth,781 hertz per pixel; echo train length, 136; and generalized autocalibrating partially parallel acquisitions (GRAPPA)[24] acceleration factor R, 1.7 (accounting for 24 reference lines) in the left-right direction. For each subject, phase-contrast MRI was performed in an axial plane to determine the trigger delay for peak systolic flow in the femoral artery. Typical trigger delay ranged from 150 to 270 milliseconds.

Contrast-enhanced MRA was performed on each of 4 patients as part of clinical MR examination, using the following relevant imaging parameters: scan time, approximately 29 seconds; field of view, 500 mm × 406 mm × 134 to 168 mm; image acquisition matrix, 384 × 234 × 96 to 120; spatial resolution, 1.3 mm × 1.7 mm × 1.4 mm; repetition time,

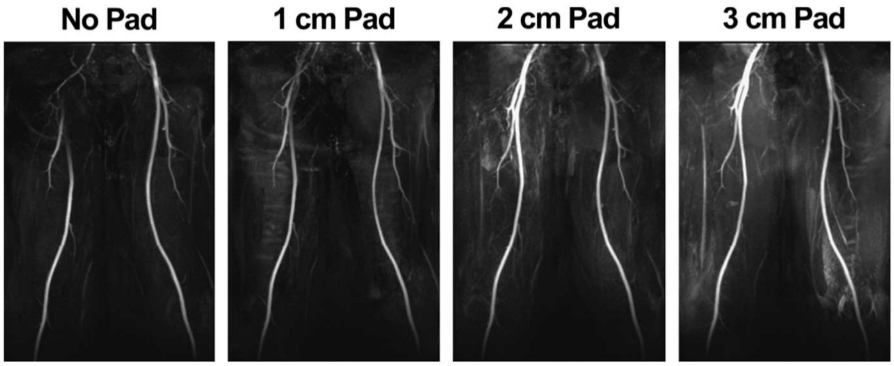

FIGURE 1. Maximum intensity projection of a volunteer with 3 different high-permittivity pad thicknesses: 1 cm (second column), 2 cm (third column), and 3 cm (fourth column). For reference, a MIP without padding is also shown (first column). All 4 MIPs were displayed with identical gray scales. The pad was placed on the upper thigh to the pelvis, following the path of the femoral arteries. On this preliminary analysis, we used the 2-cm–thick pad throughout this study.

3.5; echo time, 1.2 milliseconds; flip angle, 25 degrees; bandwidth, 781 hertz per pixel; and actual GRAPPA acceleration factor R, 1.7. Gadoteridol (Bracco, Monroe Township, NJ) was administered on the basis of subject weight (approximately 30 cc) via a power injector (MedRad, Warrendale, PA).

We used a previously described rapid B_1+ mapping pulse sequence[23] on the basis of ultrafast gradient echo (TurboFLASH) readout with centric k-space ordering. Briefly, this sequence acquires a proton density image, PD, first and then waits adequate time for full magnetization recovery (eg, 5 T_1, approximately 10 seconds). A second image, SS Pre, is then acquired using a magnetization preparation module, followed immediately by the same TurboFLASH readout. The magnetization preparation module consists of a slice-selective RF pulse with nominal flip angle $\alpha = 60$ degrees, α^{nom}, and

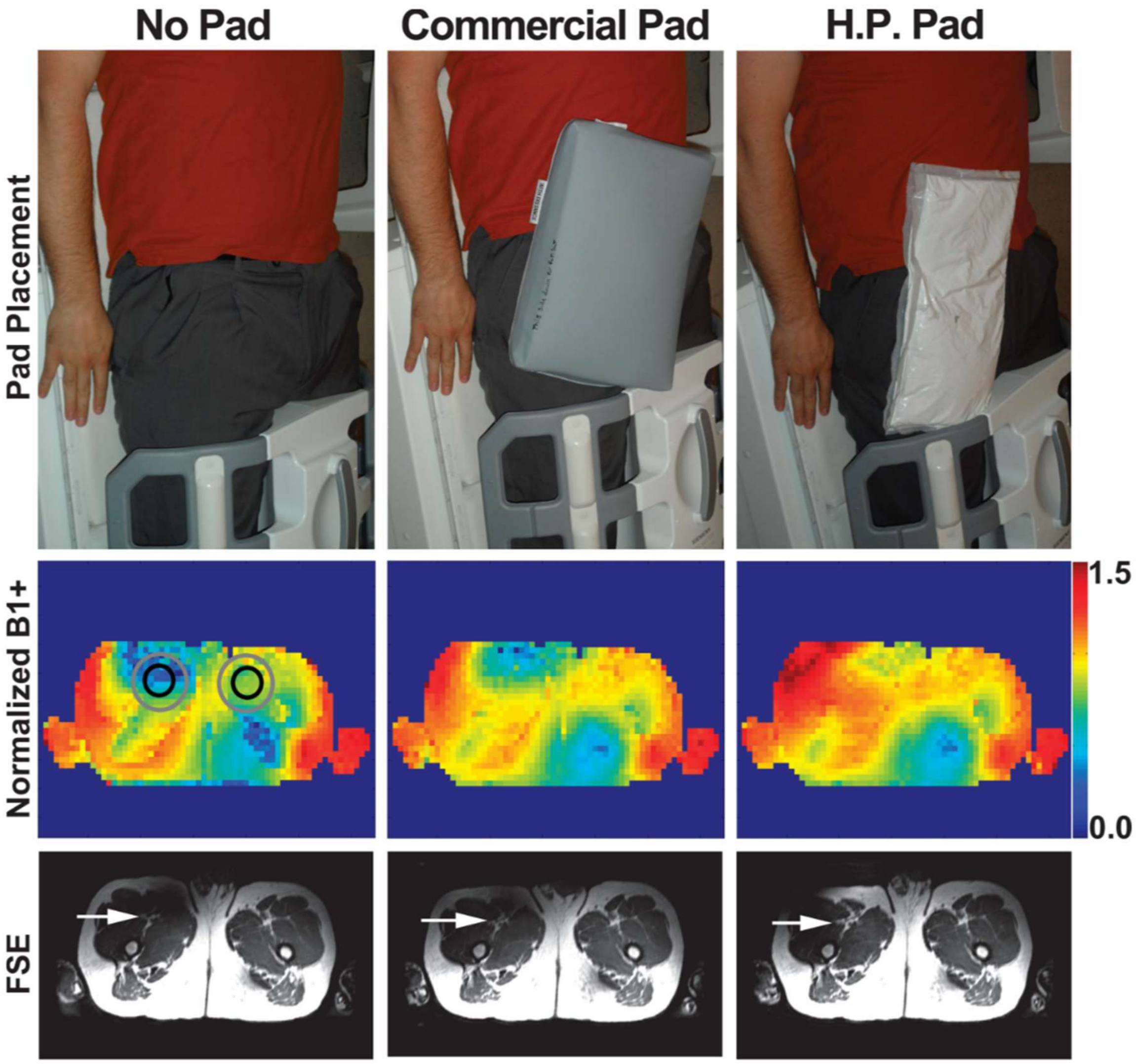

FIGURE 2. Fresh blood imaging of the thigh station acquired with 3 different padding settings (row 1 shows pad placement): no padding (left column), commercial padding (middle column), and high-permittivity padding (right column). The pad was placed on the upper thigh to the pelvis, following the path of the femoral arteries. This placement was consistent from subject to subject with the peripheral coil configuration as shown. The subject's head is toward the top of the image. Corresponding normalized B_1+ maps (row 2) and reformatted diastolic FSE images (row 3): baseline (left column), commercial padding (middle column), and high-permittivity padding (right column). At baseline, the radial symmetry in B_1+ variation reduces the B_1+ in the anterior-right ROI (gray circle) corresponding to the right common femoral artery (black circle). The B_1+ in the right common femoral artery is improved partially with commercial padding and improved further with high-permittivity padding. Similar trends are shown in the FSE images (displayed with identical gray scales). Red arrows point to the right common femoral artery. H.P. pad indicates high-permittivity padding.

spoiler gradients. The relative B_1+[23] can be calculated using the following equation:

$$K = \cos^{-1}\left(\frac{\text{SS Pre}}{\text{PD}}\right)/a^{\text{nom}} \quad (1)$$

Image Analysis

Analysis 1: Radial Symmetry in B_1+ Variation and Its Impact on FSE Signal

We quantified the radial symmetry in B_1+ variation as well as its impact on FSE signal at baseline and how dielectric padding improves B_1+ and FBI signal. We drew circular regions of interest (ROIs) to include the left and right common femoral arteries as well as their surrounding regions, as shown in Figure 2. We note that the location of the femoral arteries along the anterior-posterior direction varies among different individuals. Thus, we contend that an analysis of circular ROIs that are slightly larger than the femoral arteries is more generalizable. To match the orientation of the B_1+ maps (axial) and FSE images (coronal), we reformatted the FSE images in the axial plane and drew the corresponding ROIs in diastolic and systolic FSE images. To average the FSE signals over the subjects, we first normalized the lower (right-anterior ROI) signal by the higher (left-anterior ROI) signal (control) and then averaged the normalized signal over the subjects. This normalization is necessary because MRI signal is scaled differently for different subjects. The resulting normalized B_1+ and FSE signals were compared between dielectric padding settings.

Analysis 2: Radial Symmetry in B_1+ Variation and Its Impact on MRA

We quantified the impact of radial symmetry in B_1+ variation on FBI MRA. Specifically, we quantified contrast-to-noise ratio (CNR) = $(SI_{artery} - SI_{background\_Tissue})$/noise. The signal intensity was determined from the subtracted images, whereas noise was obtained from the diastolic images because subtracted images have altered noise statistics. For each common femoral artery, we identified the bifurcation point and drew a rectangular contour with approximately 190 pixels (approximately 120 mm^2) to quantify the mean arterial signal. The same contour was then moved laterally to background tissue to quantify the mean background signal (see insert in Fig. 3). For consistency, we used the same

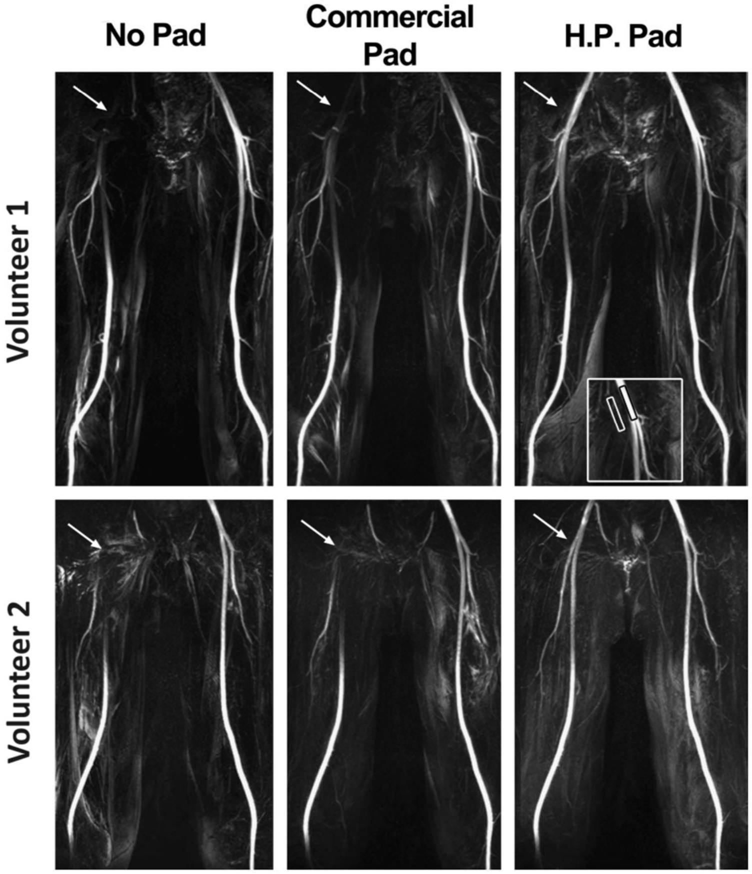

FIGURE 3. Representative MIPs of 2 volunteers (volunteer 1 on top and volunteer 2 on bottom) acquired with 3 different padding settings: baseline (left), commercial dielectric padding (middle), and high-permittivity dielectric padding (right). Compared with baseline and commercial dielectric padding, high-permittivity dielectric padding significantly increased signal around the bifurcation point of the right common femoral artery. Maximum intensity projections displayed with identical gray scales per subject. H.P. pad indicates high-permittivity padding.

TABLE 1. Mean Normalized B_1+ in an Axial Plane of the Thigh Station

Pad Setting		Baseline	Commercial Pad	High Permittivity Pad
Normalized B_1+	Right	0.62 0.17	0.76 0.11	0.96 0.17
	Left	0.92 0.11	0.95 0.07	1.01 0.10

Reported values represent mean SD over subjects.

Mean B_1+ in the anterior-right region of interest was significantly different between the 3 groups and within each pair of groups ($P < 0.0001$). Mean B_1+ in the anterior-left region of interest was different between high-permittivity padding and the other 2 groups ($P < 0.001$) but was not significantly ($P > 0.2$) different between baseline and commercial padding.

set of contours for the 3 scans. For noise estimation, we drew a circular contour with approximately 1900 pixels (approximately 1200 mm^2) in a signal-free region in diastolic images.

Image Quality Assessment

Three radiologists with 11 years (G.M.), 6 years (M.H.), and 5 years (C.H.) of experience were asked to score in consensus the conspicuity of the right and left common femoral arteries at the bifurcation level. The images were graded on a Likert scale of 1 to 5 (worst to best). The radiologists were blinded to image acquisition type and subject identity. To avoid bias, we made sure to crop out the padding in the images.

Statistical Analysis

For analysis 1, the mean B_1+ and FSE signal were compared between the 3 groups using analysis of variance and with Bonferroni correction to compare each pair of groups. Similarly, for analysis 2, the mean CNR values between the 3 groups were compared using analysis of variance and with Bonferroni correction to compare each pair of groups. For image quality analysis, the mean conspicuity scores between the 3 groups were compared using Kruskal-Wallis and with Bonferroni correction to compare each pair of groups. A P value of less than 0.05 was considered statistically significant. All statistical analyses were performed using Matlab (R2009a, Statistics Toolbox; The MathWorks, Inc, Natick, MA).

RESULTS

Analysis 1: Radial Symmetry in B_1+ variation and its Impact on FSE Signal

Figure 2 shows representative B_1+ maps displaying the radial symmetry in B_1+ variation at baseline as well as B_1+ maps acquired with commercial and high-permittivity dielectric padding. Note that the anterior-right ROI shows lower B_1+ compared with the anterior-left ROI without any padding. These B_1+ variation patterns translate to the corresponding signal variations in diastolic FSE images as shown (systolic FSE images were not shown because of space constraint, but similar trends were observed and summarized in Table 1). The attenuated B_1+ and FSE signal in the anterior-right ROI are improved partially with commercial padding and improved further with high-permittivity padding, as shown. Averaging the results over the 13 subjects, the mean B_1+ in the anterior-right ROI is significantly different ($P < 0.0001$) between the 3 padding settings, where the mean B_1+ with high-permittivity padding was significantly higher than that with commercial padding and baseline. Normalized B_1+ in the anterior-left ROI was not different between the groups ($P > 0.2$). The corresponding FSE signals showed similar trends in statistics (Table 2); the anterior-right ROI was significantly different between the 3 groups and within each pair of groups ($P < 0.0001$); the anterior-left ROI was not significantly different between the baseline and commercial padding ($P > 0.2$) but was significantly different between the high-permittivity padding and the other 2 groups ($P < 0.001$).

Analysis 2: Radial Symmetry in B_1+ Variation and its Impact on MRA

Figure 3 shows representative maximum intensity projection (MIPs) of 2 different volunteers using FBI with different dielectric padding settings. In both subjects, compared with baseline, the signal in the right common femoral artery was increased partially using commercial dielectric padding and increased further using high-permittivity padding. The signal in the left femoral artery remained consistent throughout the tests. Figure 4 shows representative MIPs of a patient with PAD. This patient's MRA results were consistent with the volunteer results shown in Figure 3 (ie, progressive improvement with commercial and then with high-permittivity padding). Note that contrast-enhanced MRA was acquired without any dielectric padding (clinical default) and that the signal in the right common femoral artery was attenuated because of the radial symmetry in B_1+ variation.

Averaging the results over the 13 subjects (Table 3), the mean SD CNR of the right common femoral artery in FBI MRA was significantly ($P < 0.001$) improved with high-permittivity padding (82 [15]), compared with no padding (12 [2]) and commercial padding (33 [8]). Similarly, the mean conspicuity (SD) score of the right common femoral artery was significantly ($P < 0.001$) improved with high-permittivity padding (4.3 [0.8]), compared with no padding (1 [0]) and commercial padding (2.5[1.0]). We note nonsignificant differences in the mean CNR and conspicuity scores for the left common artery (Table 3).

DISCUSSION

This study characterizes the radial symmetry in B_1+ variation as well as its impact on FSE signal at baseline and how dielectric padding

TABLE 2. Mean Normalized FSE signal (as a Ratio of the Right ROI Divided by the Left ROI) in an Axial Plane of the Thigh Station

Pad Setting		Baseline	Commercial Pad	High Permittivity Pad
FSE Signal Ratio	Diastolic	0.48 0.14	0.59 0.14	0.80 0.21
	Systolic	0.49 0.13	0.60 0.15	0.88 0.19

Reported values represent mean SD over subjects.

The normalized signal was significantly different between the 3 groups and within each pair of groups ($P < 0.0001$), except for the baseline and commercial pad pair ($P > 0.02$).

FSE indicates fast spin echo; ROI, region of interest.

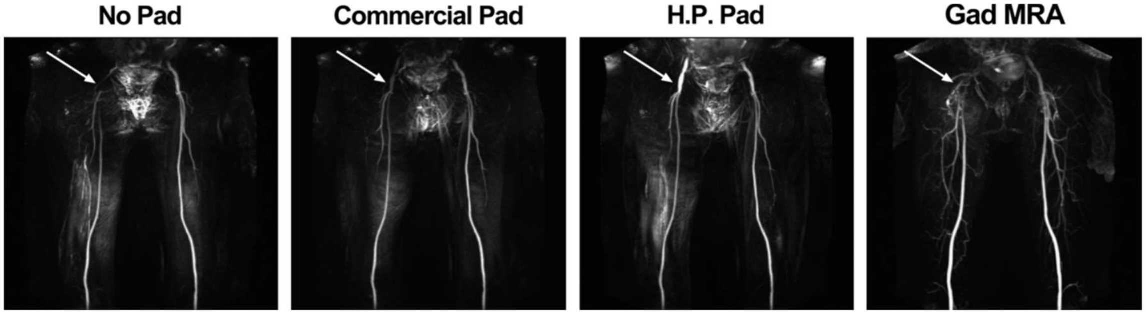

FIGURE 4. Representative MIPs of a patient with infrarenal abdominal aortic aneurysm and subsequent endovascular graft device: FBI without padding (first column), FBI with commercial padding (second column), FBI with high-permittivity padding (third column), and contrast-enhanced MRA without any padding (fourth column). The patient had an endovascular graft, which caused image artifact at the top of the image, near the bladder. The FBI MIPs are displayed with identical gray scales. Note that contrast-enhanced MRA was acquired without any dielectric padding (clinical default) and that the signal in the right common femoral artery was attenuated because of the radial symmetry in B_1+ variation. Gad MRA indicates gadolinium MRA; H.P. pad, high-permittivity padding.

improves B_1+ and FBI signal. With the subjects positioned on the MR table with feet-first, supine orientation, the B_1+ variation pattern caused signal void in the right common femoral artery. The mean B_1+, CNR, and image quality scores showed greater improvements with high-permittivity dielectric padding than commercial dielectric padding did.

High-permittivity dielectric padding provides a robust and inexpensive solution to increase the signal of femoral artery in FBI at 3 T. Unlike more expensive hardware solutions such as parallel RF transmit and B_1+ shimming, dielectric padding can be fabricated easily by the user, typically at a cost of approximately $150 for the dimensions described in this study. The commercial padding used in this study increased the signal partially, but the amount of signal enhancement was insufficient to produce adequate NC-MRA of the right common femoral artery. In addition, the thickness of commercial padding (5 cm) is less comfortable for patients and can limit proper positioning of the coil(s), especially for patients with high body mass index. High-permittivity dielectric padding used in this study was only 2-cm thick and has the clear advantage of providing more patient comfort and minimizing the gap between the coil and patient body for maximal signal reception.

The padding used in this study is a passive B_1+ correction method. As such, the resulting performance is influenced by padding size and placement. We determined the size and placement empirically to yield good results over a wide range of body weights. For other applications, one may need to adopt the dielectric material, size, and placement for optimal results. To account for different body sizes, one could make several padding sets with different sizes to achieve tailored results. We note that the particular padding size used in this study improved the quality of FBI of the thigh station over a wide range of body weight (63–95 kg). Nonetheless, additional studies in patients with different body mass indices are warranted to validate further the utility of high-permittivity dielectric padding for increasing the signal in FBI of the thigh region at 3 T. Furthermore, in this study, we did not determine the optimal combination of dielectric material and padding dimension. A future study is warranted to determine the optimal dielectric padding for FBI at 3 T. We note that the radial symmetry in B_1+ variation affects only 1 thigh. In this study, with the subjects positioned on the MR table with feet-first, supine orientation, the B_1+ variation pattern attenuated signal in the right common femoral artery. We note that, if the subject is positioned in the head-first, supine orientation, then the B_1+ variation pattern will attenuate the signal in the left common femoral artery. Thus, a user needs to consider the subject's orientation on the MR table and apply dielectric padding on the correct side. We note that CNR values reported in this study are not true values because it is not feasible to determine true image noise from GRAPPA images.[24] Because the 3 acquisitions used the same imaging parameters, except for padding, we elected to calculate noise as the standard deviation in a signal-free region and use that same noise estimate to calculate CNR for all 3 acquisitions for each subject. Although the calculated CNR may not truly reflect absolute CNR, it is adequate for comparing the 3 FBI acquisitions with different padding settings: no padding, with commercial padding, and with high-permittivity padding.

TABLE 3. Mean CNR and Conspicuity Scores for the Right and Left Common Femoral Arteries

Pad Setting		Baseline		Commercial Pad		High Permittivity Pad	
Right	CNR	12	2	33	8	82	15
	Conspicuity	1.0	0.0	2.5	1.0	4.3	0.8
Left	CNR	84	13	78	10	96	17
	Conspicuity	4.5	0.7	4.5	0.7	4.5	0.7

Reported values represent mean SD over subjects.

In the right common femoral artery, the mean CNR and conspicuity scores were significantly different between the 3 groups and within each pair of groups ($P < 0.0001$), whereas in the left common femoral artery, the mean CNR and conspicuity scores were not significantly different between the groups ($P > 0.5$). Note that the dielectric pads were placed on the subjects as shown in Figure 2. The dielectric pads extended to the medial portion of the pelvis, and as a consequence, the pads affected the left thigh as well.

CNR indicates contrast-to-noise ratio.

CONCLUSIONS

This study shows that the radial symmetry in B_1+ variation at 3 T attenuates the signal of femoral artery in FBI in 1 thigh only. This study also shows that high-permittivity thin dielectric padding can be used to increase the signal of femoral artery in FBI at 3 T.

ACKNOWLEDGMENTS

The authors thank Andrew Webb of the Leiden University Medical Center for his helpful suggestions on constructing the dielectric padding.

REFERENCES

1. Selvin E, Erlinger TP. Prevalence of and risk factors for peripheral arterial disease in the United States: results from the National Health and Nutrition Examination Survey, 1999–2000. *Circulation.* 2004;110:738–743.

2. Ho KY, Leiner T, de Haan MW, et al. Peripheral vascular tree stenoses: evaluation with moving-bed infusion-tracking MR angiography. *Radiology*. 1998;206:683–692.
3. Al-Qaisi M, Nott DM, King DH, et al. Imaging of peripheral vascular disease. *Rep Med Imaging*. 2009;2:25–34.
4. Runge VM. Gadolinium and nephrogenic systemic fibrosis. *Am J Roentgenol*. 2009;192:W195–W196.
5. Collidge TA, Thomson PC, Mark PB, et al. Gadolinium-enhanced MR imaging and nephrogenic systemic fibrosis: retrospective study of a renal replacement therapy cohort1. *Radiology*. 2007;245:168–175.
6. Tranche-Iparraguirre S, Marin-Iranzo R, Fernandez-de Sanmamed R, et al. Peripheral arterial disease and kidney failure: a frequent association. *Nefrologia*. 2012;32:313–320.
7. Hodnett PA, Koktzoglou I, Davarpanah AH, et al. Evaluation of peripheral arterial disease with nonenhanced quiescent-interval single-shot MR angiography. *Radiology*. 2011;260:282–293.
8. Li D, Lin J, Yan F, et al. Unenhanced calf MR angiography at 3.0 T using electrocardiography-gated partial-Fourier fast spin echo imaging with variable flip angle. *Eur Radiol*. 2011;21:1311–1322.
9. Wedeen VJ, Meuli RA, Edelman RR, et al. Projective imaging of pulsatile flow with magnetic resonance. *Science*. 1985;230:946–948.
10. Miyazaki M, Sugiura S, Tateishi F, et al. Non-contrast-enhanced MR angiography using 3D ECG-synchronized half-Fourier fast spin echo. *J Magn Reson Imaging*. 2000;12:776–783.
11. Lim RP, Fan Z, Chatterji M, et al. Comparison of nonenhanced MR angiographic subtraction techniques for infragenual arteries at 1.5 T: a preliminary study. *Radiology*. 2013;267:293–304.
12. Hoey ET, Ganeshan A, Puni R, et al. Fresh blood imaging of the peripheral vasculature: an emerging unenhanced MR technique. *AJR Am J Roentgenol*. 2010;195: 1444–1448.
13. Nakamura K, Miyazaki M, Kuroki K, et al. Noncontrast-enhanced peripheral MRA: technical optimization of flow-spoiled fresh blood imaging for screening peripheral arterial diseases. *Magn Reson Med*. 2011;65:595–602.
14. Storey P, Lim RP, Kim S, et al. Arterial flow characteristics in the presence of vascular disease and implications for fast spin echo-based noncontrast MR angiography. *J Magn Reson Imaging*. 2011;34:1472–1479.
15. Haneder S, Attenberger UI, Riffel P, et al. Magnetic resonance angiography (MRA) of the calf station at 3.0 T: intraindividual comparison of non-enhanced ECG-gated flow-dependent MRA, continuous table movement MRA and time-resolved MRA. *Eur Radiol*. 2011;21:1452–1461.
16. Storey P, Lee V, Sodickson D, et al. B1 inhomogeneity in the thigh at 3T and implications for peripheral vascular imaging. Proceedings of the 17th Annual Meeting of ISMRM, Honolulu, Hawaii, USA; 2009. p. 425.
17. Teeuwisse WM, Brink WM, Haines KN, et al. Simulations of high permittivity materials for 7 T neuroimaging and evaluation of a new barium titanate-based dielectric. *Magn Reson Med*. 2012;67:912–918.
18. Haines K, Smith NB, Webb AG. New high dielectric constant materials for tailoring the B1+ distribution at high magnetic fields. *J Magn Reson*. 2010;203: 323–327.
19. Brink WM, Webb AG. High permittivity pads reduce specific absorption rate, improve B homogeneity, and increase contrast-to-noise ratio for functional cardiac MRI at 3 T. *Magn Reson Med*. 2014;71:1632–1640.
20. de Heer P, Brink WM, Kooij BJ, et al. Increasing signal homogeneity and image quality in abdominal imaging at 3 T with very high permittivity materials. *Magn Reson Med*. 2012;68:1317–1324.
21. Brink WM, van der Jagt AM, Versluis MJ, et al. High permittivity dielectric pads improve high spatial resolution magnetic resonance imaging of the inner ear at 7 T. *Invest Radiol*. 2014;49:271–277.
22. Lindley MD, Kim D, Morrell G, et al. High-permittivity thin dielectric pad improves peripheral non-contrast MRA at 3T. *J Cardiovasc Magn Reson*. 2014;16:166.
23. Chung S, Kim D, Breton E, et al. Rapid B1+ mapping using a preconditioning RF pulse with TurboFLASH readout. *Magn Reson Med*. 2010;64:439–446.
24. Griswold MA, Jakob PM, Heidemann RM, et al. Generalized autocalibrating partially parallel acquisitions (GRAPPA). *Magn Reson Med*. 2002;47:1202–1210.

CHAPTER 7

ACCELERATED NONCONTRAST AORTOILIAC MAGNETIC RESONANCE ANGIOGRAPHY USING 3D RADIAL K-SPACE SAMPLING AND COMPRESSED SENSING

7.1 Introduction

Contrast-enhanced MR angiography (MRA) with a gadolinium (Gd)-based contrast agent is a clinically accepted test for assessment of peripheral arterial disease (PAD). As of today, over 8 million Americans are affected with PAD, where 12% to 20% of those are 65 years of age or older (1). Approximately 30% of PAD patients also have renal insufficiency (2). Gd-based contrast agents are known to be associated with nephrogenic systemic fibrosis. This concern has created a renewed interest in noncontrast MRA (NC-MRA) methods (3-7). NC-MRA also offers additional benefits such as reduced examination cost and capability to repeat as needed.

We have recently developed quadruple-inversion-recovery (QIR) NC MRA (6) for assessment of aortoiliac arteries using parallel imaging and evaluated its accuracy in patients with PAD (8). Despite its initial success, its lengthy examination time of 12-20 min continues to be a hindrance for routine clinical use.

Compressed sensing (CS) or constrained reconstruction methods are well-suited for MRA, because the data content is largely sparse (9-11). 3D radial k-space sampling (12) with golden angle ratio (13) has several features that are well suited for accelerated MRA with CS, including motion properties and incoherent aliasing artifacts with undersampling (14,15). While radial k- space sampling with golden angle ratio has several benefits for CS, for applications using balanced steady-state free precession (b-SSFP) readout, golden angle ratio produces image artifacts arising from eddy currents (16). This problem can be addressed using tiny golden angle ratio, as previously described (16,17).

In this study, we sought to accelerate QIR NC-MRA using 3D radial k-space sampling with tiny golden angle ratio (16,17) and CS using nonlocal means (NLM) filtering (18,19). Our goal was to evaluate the performance of QIR NC-MRA using parallel imaging compared to CS.

7.2 Methods

7.2.1 Simulation

To determine the theoretical limits of acceleration, we evaluated different k-space undersampling patterns with different acceleration factors (R). Numerical simulation experiments were performed using a fully-sampled data set obtained from a healthy volunteer. First, we compared Cartesian and radial stack of stars sampling patterns with R = 5.3, which is approximately 2-fold higher than R = 2.7 with parallel imaging. We note that R in radial k-space sampling is calculated with respect to Nyquist sampling in Cartesian space (i.e., same number of k-space lines between Cartesian and radial). Given that radial stack of stars is better suited for acceleration than Cartesian, additional radial k-space patterns with R = 10.7 and 16 were tested. Note that the choice of R is constrained by the need to achieve consistent inversion time for a partition of k-space. Retrospectively, undersampled data sets were reconstructed using the steps outlined below (see Image Reconstruction). Here, as a preliminary step in study design, we report results from this numerical experiment. As shown in Figure 7.1, compared with fully sampled, radial results were in better agreement than Cartesian results at R

= 5.3. Radial data with R = 10.7 and 16 produced considerable image artifacts. Thus, we used radial k-space sampling with R = 5.3 throughout this study.

7.2.1.1 Image Reconstruction

Image reconstruction was performed using MATLAB (R2014a, The MathWorks, Inc., Natick, MA), applying NLM, a denoising algorithm which compares pixels inside of a search window using weighted averages and has been shown to reduce incoherent artifacts in MRI images (18,19). Prior to NLM denoising, k-space data set was normalized to its largest value. NLM was performed in three dimensions, with comparison and search windows with 3x3x3 and 5x5x5 dimensions, respectively. 50 iterations of denoising were performed per data set. These settings were determined empirically to balance image reconstruction time and resulting image quality. See Section 7.6 for more details on NLM denoising steps.

7.2.2 Prospective Studies

7.2.2.1 Volunteer and Patient Studies

The study performed was HIPAA-compliant and approved by the Institutional Review Board. We obtained written informed consent from all human subjects. A total of 7 healthy volunteers (4 male, 3 female, mean age 39 yrs, range 24-60 yrs), and 4 patients with aortoiliac (2 male, 2 female, mean age 63 yrs, range 53-71 yrs) were imaged. Imaging was performed on a whole body 3T system (Tim Trio, Siemens Healthcare, Erlangen, Germany; maximum gradient strength = 40 mT/m; slew rate = 200 T/m/s). Excitation was performed using the body coil, and two phased array body coils and a spine coil array were used for signal reception

Two different QIR NC-MRA acquisitions were performed: 1) with GRAPPA R = 2.7 and 2) 3D stack-of-stars radial sampling with tiny golden angles with R = 5.3. The pulse sequence order was randomized for each subject. For parallel imaging acceleration each k_x-k_y partition was acquired in 2 shots. Radial stack-of-stars with R = 5.3 requires that each k_x-k_y partition is acquired in one shot.

In prospective studies it was observed that streaking artifacts were contaminating regions of the reconstructed image. We identified coils with severe streaking artifacts using a previously developed method (20) and removed them during reconstruction. NLM denoising was performed as described in Section 7.6.

7.2.2.2 Imaging Algorithm

Our imaging sequence has been described in detail elsewhere (6,8). Imaging parameters used were 318 (phase-encoding) x 320 (frequency-encoding) x 88-144 (partition-encoding) matrix for parallel imaging and 320 x 320 x 88-144 matrix for radial acquisition, where the number of partition encodings, or slices, depends on patient size, 1.3 x 1.3 x 1.7 mm^3 resolution, field of view (FOV) 400 x 400 x 176.8 - 244.8 mm^3 (last dimension is anterior-to-posterior coverage that depended on patient size), TR was one respiratory cycle, and respiratory gating used a respiratory belt with trigger occurring at 20% of exhalation. The same protocol was performed using conventional GRAPPA parallel imaging (R = 2.7) and radial undersampling with tiny golden angle ratio and CS (R = 5.3). Acquisition timing differences between radial and parallel imaging can be seen in Figure 7.2.

An oblique coronal imaging slab was used, with the superior edge of the slab positioned ~1 cm superior to the kidneys, to ensure inclusion of the renal arteries. All other imaging parameters were identical between parallel imaging and radial acquisitions, including TE = 2.1 ms, receiver bandwidth = 998 Hz / pixel, and flip angle = 100°. We used an inversion time (TI) = 1,600 ms, which was empirically determined to maximize the signal difference between the blood and background. See Section 7.6.2 for more details.

In prospective studies it was observed that streaking artifacts were contaminating regions of the reconstructed image. We identified coils with severe streaking artifacts using a previously developed method (20) and removed them during reconstruction. NLM denoising was performed in the way as previously described in the image reconstruction section, with empirical determined NLM and data fidelity weights.

7.2.3 Image Evaluation

For all acquisitions, source images were anonymized and presented in random order to two radiologists (Reader 1 with 9 years of experience, Reader 2 with 4 years of experience) to perform an independent blinded review. Readers were also blinded to clinical history, each other, and patient identity. There were four regions that were graded for image quality: the aorta, the renal arteries, the common iliac arteries, and the external iliac arteries. Image quality was rated for each region on a Likert-type scale from 1 to 5, with 1 = nondiagnostic and 5 = excellent. Image artifact was also scored on a scale from 1 to 5, with 1 = no visible artifact and 5 = artifacts.

To quantify the apparent contrast-to-noise ratio (CNR), signal difference between the arterial and background signal was determined, the difference was divided by the signal of the arteries for normalization. This calculation was performed at four locations to determine an average: near the renal artery origins, near the aortal bifurcation, and at the left and right iliac bifurcation areas, as shown by the arrows in Figure 7.3. This calculation was used as a surrogate for a true CNR since measuring CNR from GRAPPA and CS data is not straightforward. Vessel dimensions were also measured at the same four locations by the same reader.

7.2.4 Statistical Analysis

For aortic dimensions and signal difference measurements, the two groups (GRAPPA R = 2.7 and Radial R = 5.3) were compared using a paired *t*-test. For qualitative image quality scores, the two groups were compared using a Wilcoxon rank-sum test. A *p* value < 0.05 was considered statistically significant. All statistical analyses were performed using Matlab (R2014a, Statistics Toolbox, The MathWorks, Inc., Natick, MA).

7.3 Results

The mean scan time was 14.6 ± 2.9 minutes and 7.2 ± 1.8 minutes for GRAPPA and CS R = 5.3 acquisitions, respectively. Representative maximum intensity projection (MIP) images can be seen in Figure 7.3.

For quantitative evaluation, vessel dimensions and apparent CNR values were not significantly ($p > 0.07$) different between GRAPPA R = 2.7 and CS R = 5.3 acquisitions (see Table 7.1). For qualitative evaluation, there was no significant difference in image quality, artifact, and noise scores between GRAPPA and CS acquisitions ($p > 0.06$, Table 7.2).

7.4 Discussion

This study demonstrates feasibility of 5.3-fold accelerated QIR NC-MRA using 3D radial stack-of-stars with tiny golden angle CS, enabling 2-fold additional acceleration compared with previously described GRAPPA QIR NC-MRA with R = 2.7. Image quality scores based on the randomized and anonymized results from two radiologists showed no significant difference between the GRAPPA and radial accelerated acquisitions. The proposed acceleration strategy provides a means to perform QIR NC-MRA within about 7-8 min.

Retrospective studies were performed to test different sampling patterns and acceleration rates. Radial acquisitions appeared to perform better than Cartesian acquisitions for the same acceleration. Additional studies investigating different undersampling patterns could be explored to determine an optimal sampling pattern.

Because radial acquisitions sample the center of k-space with every ray, it was necessary to determine empirically an optimal TI. One subject was tested with varying TIs for GRAPPA and CS radial acquisitions, and for both acquisitions TI = 1600 ms was selected as the optimal timing. Different sampling patterns might require further optimization of TI.

Results showed no significant difference in reader scores between the GRAPPA R = 2.7 and radial R = 5.3 acquisitions. Further study is warranted to determine optimal CS constraints and diagnostic performance in patients with aortoiliac disease. Due to the constraints presented by the acquisition type (i.e., consistent TI weighting per k_y-k_z partition), reducing rays would not decrease acquisition time, but could decrease readout duration per respiratory cycle. There was slightly decreased image quality in the renal arteries and the external iliac arteries compared to the GRAPPA method with R = 2.7 and radial CS R = 5.3. The values were not deemed, however, to be statistically significant.

This study has several limitations worth mentioning. First, reconstruction time is a major issue that needs to be sped up in the future. Current reconstruction time per data set using a CPU with 8 cores and 128 GB of RAM is on the order of 60 hours. This could be accelerated using GPU and parallel computing that is available as a product package in Matlab. Reconstruction time reduction strategies need to be explored to make this method viable for clinical use. Second, using respiratory gating with QIR NC-MRA can cause signal dephasing in the upper aorta, due to inconsistent timing in the cardiac cycle. This inconsistency can be corrected by switching to ECG-gating and free breathing acquisition, but in that scenario respiratory motion may obscure the renal arteries. One solution might to be use ECG-triggering and respiratory gating, at the expense of increased scan time. Third, this study was tested in a limited number of subjects (7 volunteers and 4 patients), for the purpose of demonstrating feasibility. Further study in a larger cohort of patients is warranted to determine the diagnostic performance in comparison with gadolinium-enhanced MRA. This study demonstrates feasibility of 5.3-fold accelerated QIR NC-MRA using 3D radial stack-of-stars with tiny golden angle CS, enabling 2-fold additional acceleration compared with previously described GRAPPA QIR NC-MRA with R = 2.7. Image quality scores based on the randomized and anonymized results from two radiologists showed no significant difference between the GRAPPA and radial accelerated acquisitions. The proposed acceleration strategy provides a means to perform QIR NC-MRA within about 7-8 min.

7.5 Conclusion

We have shown that through the use of 3D radial stack of stars with tiny golden angles and NLM denoising, it is possible to reduce the scan time of QIR NC-MRA of the aortoiliac arteries by a factor of 2 compared with a previously reported acquisition with GRAPPA.

7.6 Supplemental Materials

7.6.1 NLM Reconstruction

NLM denoising was carried out as described below. A cost function is applied to the spatial neighborhood, S_{nbd}

$$\mathrm{Snbd} = \sum_{p \in tfr} \sum_{q \in \Omega_s(p)} \mathbf{w}_s\,(p, q) \left\| \mathbf{m}_p - \mathbf{m}_q \right\|_2^2 \qquad [7.1]$$

The cost function, Eqn 7.1, uses an initial estimate m, where m_p and m_q are individual pixels at points p and q in a particular time frame, tfr. By minimizing this functional, Eqn 7.1, undersampled k-space data can have resulting image artifacts resolved. Iterative steps are used to minimize this functional.

Steps followed in reconstruction are outlined below.

(1) An initial estimate is chosen, m_0. The initial estimate for this project was the inverse Fourier transformed undersampled k-space data, with coil sensitivity maps applied.

(2) The current estimate is projected on the data consistency term:

$$m^n_{data} = m^n + \mathrm{E}'(\mathrm{d} - \mathrm{E}m^n) \qquad [7.2]$$

where E’ is the adjoint operator of E.

(3) Weights are computed according to

$$\mathrm{w(p,q)} = e^{\frac{-d(p,q)}{h^2}}; d(p,q) = G_\sigma \left\| m(N_p) - m(N_q) \right\|_2^2 \qquad [7.3]$$

where d(p,q) is the Gaussian weighted L_2 norm distance between neighborhoods.

(4) The neighborhood term is minimized by applying NLM to the real and complex parts individually according to the weights from Step 3.

(5) The initial estimate is updated according to the new image from the constraints.

Steps 2-5 are repeated a predetermined number of times. In this study the number of iterations performed per data set was 50, with a step size of 0.05. Data fidelity and NLM weights were 0.7 and 0.7 for R = 5.3. The initial estimate, m_0, was the inverse Fourier transform of the undersampled data with coil sensitivity maps applied. Coil sensitivity maps are estimated from the highly sampled center of k-space (64x64 center lines)(11,21).

7.6.2 Empirical Determination of Optimal TI

Since QIR NC-MRA relies on nulling the background, while allowing adequate time for the reinverted, fresh blood from the aorta to transit into the iliac arteries, an optimal TI needs to be determined at 3T, as was previously done for 1.5T (6). Given that T1 of tissue is higher at 3T than at 1.5T, we set TI = 1,500 ms as the lower limit and increased it to 1,800 ms (100 ms steps). This same test was conducted for parallel imaging and radial sampling acquisitions in one volunteer.

Optimal TI was determined by measuring signal of artifact/signal-free background tissue. Four locations were tested for background signal: near the renal arteries, at the aortal bifurcation, and near the right and left iliac bifurcation sites, with results shown in Figure 7.4. Our preliminary analysis showed that the background signal was lowest with TI = 1,600 ms, as shown in Figure 7.5. As a result, TI = 1,600 ms was used throughout.

7.7 References

1. Rosamond W, Flegal K, Furie K, Go A, Greenlund K, Haase N, Hailpern SM, Ho M, Howard V, Kissela B, Kittner S, Lloyd-Jones D, McDermott M, Meigs J, Moy C, Nichol G, O'Donnell C, Roger V, Sorlie P, Steinberger J, Thom T, Wilson M, Hong Y. Heart disease and stroke statistics--2008 update: a report from the american heart association statistics committee and stroke statistics subcommittee. Circulation 2008;117:e25-146.

2. O'Hare AM, Bertenthal D, Shlipak MG, Sen S, Chren MM. Impact of renal insufficiency on mortality in advanced lower extremity peripheral arterial disease. J Am Soc Nephrol 2005;16:514-519.

3. Wedeen VJ, Meuli RA, Edelman RR, Geller SC, Frank LR, Brady TJ, Rosen BR. Projective imaging of pulsatile flow with magnetic resonance. Science 1985;230:946-948.

4. Miyazaki M, Sugiura S, Tateishi F, Wada H, Kassai Y, Abe H. Non-contrast-enhanced MR angiography using 3D ECG-synchronized half-Fourier fast spin echo. J Magn Reson Imaging 2000;12:776-783.

5. Li D, Lin J, Yan F, Wu Q, Lv W, San Y, Yun H. Unenhanced calf MR angiography at 3.0 T using electrocardiography-gated partial-fourier fast spin echo imaging with variable flip angle. Eur Radiol 2011;21:1311-1322.

6. Atanasova IP, Kim D, Lim RP, Storey P, Kim S, Guo H, Lee VS. Noncontrast MR angiography for comprehensive assessment of abdominopelvic arteries using quadruple inversion-recovery preconditioning and 3D balanced steady-state free precession imaging. J Magn Reson Imaging 2011;33:1430-1439.

7. Shin T, Worters PW, Hu BS, Nishimura DG. Non-contrast-enhanced renal

and abdominal MR angiography using velocity-selective inversion preparation. Magn Reson Med 2013;69:1268-1275.

8. Atanasova IP, Lim RP, Chandarana H, Storey P, Bruno MT, Kim D, Lee VS. Quadruple inversion-recovery b-SSFP MRA of the abdomen: initial clinical validation. Eur J Radiol 2014;83:1612-1619.

9. Cukur T, Lustig M, Nishimura DG. Improving non-contrast-enhanced steady-state free precession angiography with compressed sensing. Magn Reson Med 2009;61:1122-1131.

10. Zhang C, van de Giessen M, Eisemann E, Vilanova A. User-guided compressed sensing for magnetic resonance angiography. In Proceedings of 36th Annual International Conference of the IEEE, Institute of Electrical and Electronics Engineers (IEEE), Chicago, Illinois, USA, 2014. p 2416-2419.

11. Lustig M, Donoho D, Pauly JM. Sparse MRI: The application of compressed sensing for rapid MR imaging. Magn Reson Med 2007;58:1182-1195.

12. Wech T, Pickl W, Tran-Gia J, Ritter C, Beer M, Hahn D, Kostler H. Whole-heart cine MRI in a single breath-hold--a compressed sensing accelerated 3D acquisition technique for assessment of cardiac function. Rofo 2014;186:37-41.

13. Winkelmann S, Schaeffter T, Koehler T, Eggers H, Doessel O. An optimal radial profile order based on the golden ratio for time-resolved MRI. IEEE Trans Med Imaging 2007;26:68-76.

14. Wu Y, Korosec FR, Mistretta CA, Wieben O. CE-MRA of the lower extremities using HYPR stack-of-stars. J Magn Reson Imaging 2009;29:917-923.

15. Chen L, Adluru G, Schabel MC, McGann CJ, Dibella EV. Myocardial perfusion MRI with an undersampled 3D stack-of-stars sequence. Med Phys 2012;39:5204-5211.

16. Wundrak S, Paul J, Ulrici J, Hell E, Geibel MA, Bernhardt P, Rottbauer W, Rasche V. Golden ratio sparse MRI using tiny golden angles. Magn Reson Med 2016;75:2372-2378.

17. Wundrak S, Paul J, Ulrici J, Hell E, Rasche V. A small surrogate for the golden angle in time-resolved radial MRI based on generalized Fibonacci sequences. IEEE Trans Med Imaging 2015;34:1262-1269.

18. Tristan-Vega A, Garcia-Perez V, Aja-Fernandez S, Westin CF. Efficient and robust nonlocal means denoising of MR data based on salient features matching. Comput Methods Programs Biomed 2012;105:131-144.

19. Manjon JV, Carbonell-Caballero J, Lull JJ, Garcia-Marti G, Marti-Bonmati L, Robles M. MRI denoising using non-local means. Med Image Anal 2008;12:514-523.

20. Xue Y, Yu J, Kang HS, Englander S, Rosen MA, Song HK. Automatic coil selection for streak artifact reduction in radial MRI. Magn Reson Med 2012;67:470-476.

21. Walsh DO, Gmitro AF, Marcellin MW. Adaptive reconstruction of phased array MR imagery. Magn Reson Med 2000;43:682-690.

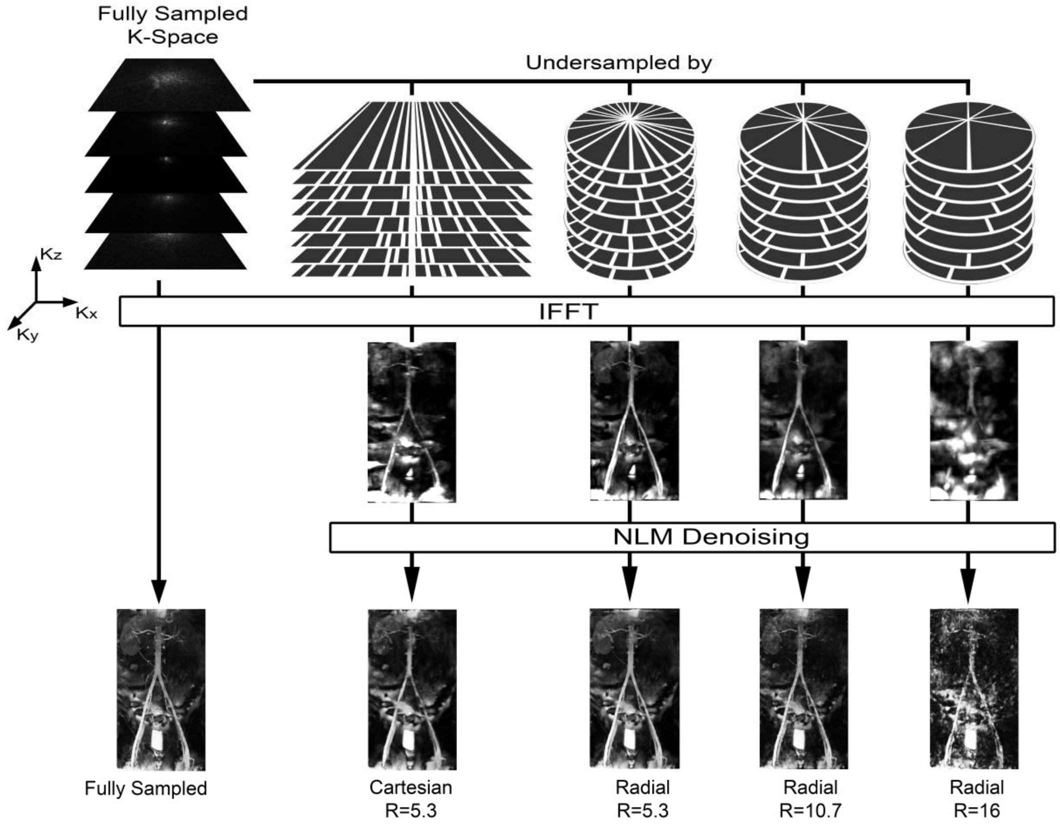

Figure 7.1: Fully sampled data was acquired, and then retrospectively undersampled with a (i) Cartesian R = 5.3 and radial (ii) R = 5.3, (iii) R = 10.6 and (iv) R = 16 undersampling patterns with a nonlocal means denoising algorithm.

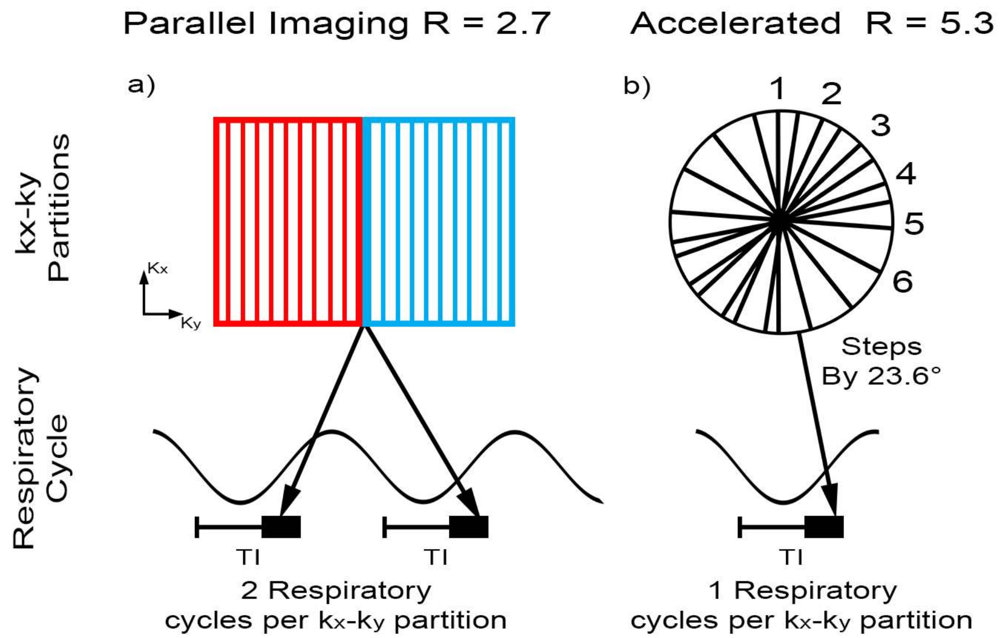

Figure 7.2: Representative timing for (a) parallel imaging and (b) radial with R = 5.3. For the parallel imaging and radial R = 5.3, one kx-ky partition is acquired in two respiratory cycles, with red and blue denoting lines acquired in each respiratory cycle, and one respiratory cycle, respectively.

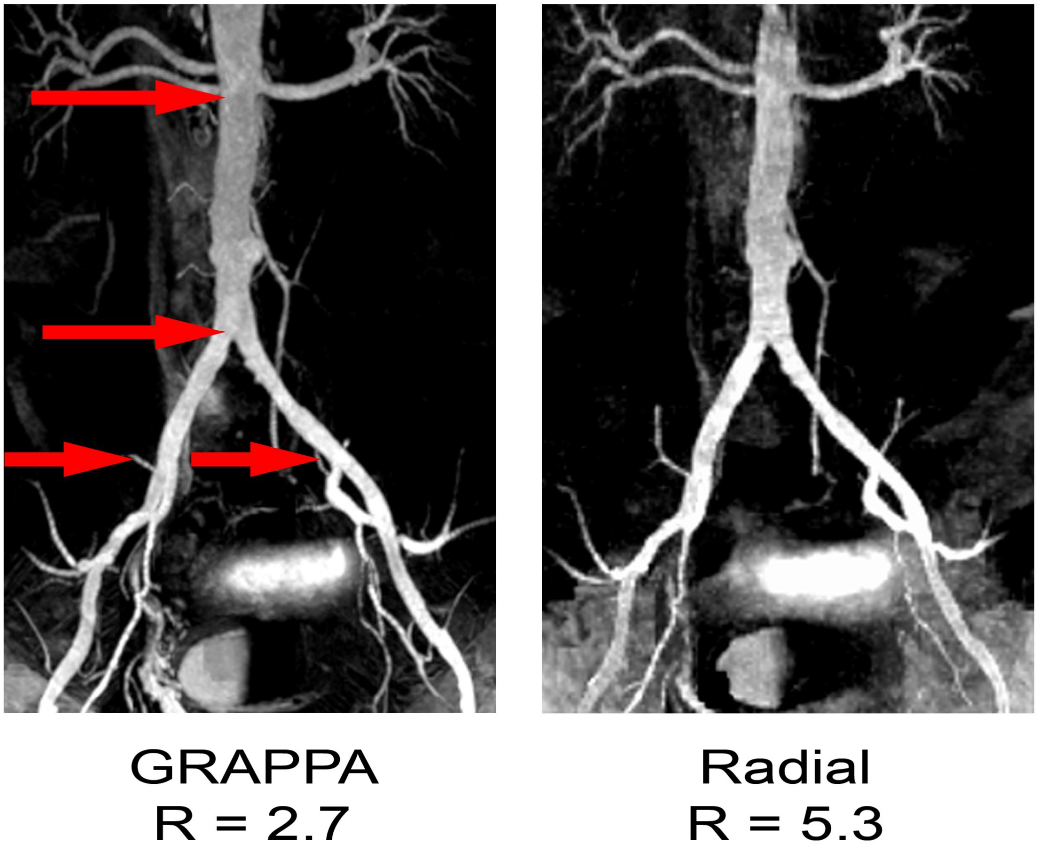

Figure 7.3: Representative maximum intensity projection images showing results for (left) GRAPPA R = 2.7 and (right) radial R = 5.3. Quantitative results were obtained at the four locations specified with the red arrows.

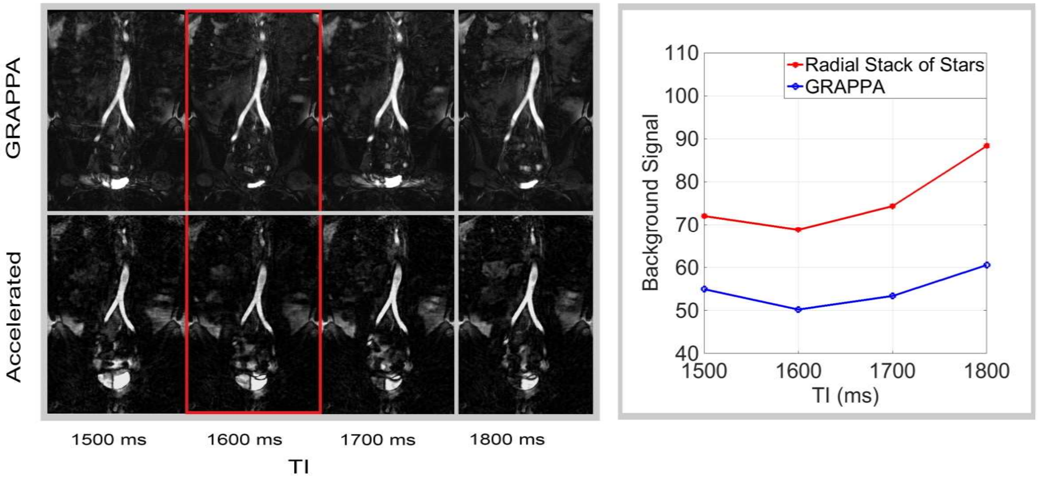

Figure 7.4: Determination of optimal TI for parallel imaging (GRAPPA) and radial accelerated acquisitions. Optimal TI was selected by determining which TI timing resulted in the lowest background signal. It was determined that for both GRAPPA and radial acquisitions the optimal TI was 1,600 ms.

Table 7.1: Normalized signal difference between arterial and background signals (left) where arterial signal is used as control, and vessel diameter measurements in cm (right). Measurements were taken for the aorta at the renal arteries and the aortic bifurcation, and for the iliacs at the left and right iliac bifurcation. Results represent mean ± standard deviation.

		Normalized Signal Difference		**p-value**	**Vessel Diameter Measurements (cm)**		**p-value**
		GRAPPA R=2.7	**Radial R=5.3**		**GRAPPA R=2.7**	**Radial R=5.3**	
Location	**Renals**	0.83 ± 0.16	0.91 ± 0.05	0.2	1.56 ± 0.13	1.54 ± 0.12	0.2
	Aortic Bifurcation	0.90 ± 0.06	0.94 ± 0.04	0.18	1.46± 0.14	1.46 ± 0.16	0.7
	Left Iliac Bifurcation	0.93 ± 0.02	0.96 ± 0.02	0.07	1.00 ± 0.26	0.99 ± 0.22	0.4
	Right Iliac Bifurcation	0.93 ± 0.02	0.94 ± 0.04	0.5	1.05 ± 0.21	1.02 ± 0.17	0.16

Table 7.2: Comparison of overall image quality score, noise, and artifact scores evaluated. Results represent mean ± standard deviation of average of 2 readers.

		Acquisition		**p-value**
		GRAPPA **R=2.7**	**Radial** **R=5.3**	
Location	**Renal Arteries**	4.0 ± 1.27	3.41 ± 0.91	0.06
	Aorta	4.18 ± 0.96	4.05 ± 1.00	0.5
	Common Iliacs	4.60 ± 0.80	4.73± 0.46	0.77
	External Iliacs	4.23 ± 1.11	3.64 ± 1.50	0.15
Noise		3.68 ± 0.95	3.45 ± 0.74	0.32
Artifact		3.95 ± 0.95	3.66 ± 0.68	0.07

CHAPTER 8

BREATH-HOLD NONCONTRAST THORACIC MRA USING 3D RADIAL STACK-OF-STARS AND COMPRESSED SENSING

8.1 Introduction

Contrast-enhanced 3D magnetic resonance angiography (CE-MRA) is routinely used for diagnosis of aortic disease. Without ECG gating, high spatial resolution is possible at the expense of acquisition, particularly at the aortic root. Alternatively, ECG gating can be used to suppress motion-induced blurring, but at the expense of spatial resolution. Neither approach has emerged as a clear winner. Both approaches require a gadolinium-based contrast agent, which is contraindicated for patients with impaired renal function (1-3).

ECG-gated, noncontrast (NC)-MRA is an alternative method that could be used for the general population and can be repeated immediately as needed. This method is based on T2-preparation and fat suppression prior to balanced steady-state free precession (b-SSFP) readout. A previous approach reported an acceleration factor (R) = 2 with a breath-hold duration of 40 heartbeats (4), which is not clinically feasible. Another approach reported GRAPPA acceleration factor (R) = 6 using a 32-element cardiac coil array (5), which is not widely available. This study seeks to develop and evaluate an accelerated NC-MRA pulse sequence using standard coil arrays.

3D radial k-space sampling (6) with golden angle ratio (7) has several features that are well suited for accelerated MRA with compressed sensing (CS), including motion properties and incoherent aliasing artifacts with undersampling (8,9). While radial k-space sampling with golden angle ratio has several benefits for CS, for applications using b-SSFP readout, golden angle ratio produces image artifacts arising from eddy currents (10). This problem can be addressed using tiny golden angle ratio, as previously described (10,11). For this study, we developed an accelerated NC-MRA using a combination of 3D radial stack-of-stars with tiny golden angles (10,11) and CS. We compare its performance versus ECG-gated CE-MRA.

8.2 Methods

8.2.1 Imaging Technique

The study performed was HIPAA-compliant and approved by the Institutional Review Board, and written informed consent was obtained from all subjects. 19 patients scheduled to undergo clinical cardiac MRI were scanned on a 1.5T scanner (Avanto, Siemens Healthcare, Erlangen, Germany; maximum gradient strength = 40 mT/m; slew rate = 200 T/m/s) with standard coil arrays. Each patient underwent breath-hold ECG-gated NC-MRA (research) and breath-hold ECG-gated CE-MRA (clinical). NC-MRA with b-SSFP readout used the following imaging parameters: TR = 1 heart beat, TE = 2.2 ms, flip angle =100°, FOV = 350 x 350 x 76.8-83.2 mm^3, image acquisition matrix = 256 x 256, slices = 24-26, resolution = 1.3 x 1.3 x 3.2 mm^3, with slice resolution interpolated to 1.6 mm, bandwidth 500 Hz/pixel, radial views = 48 per cardiac cycle, T2 preparation pulse with TE = 50 ms, and fat suppression pulse. Representative timing is shown in Figure 8.1. The 48 radial views gives an acceleration factor (R) of 5.3. We note that R in radial k-space sampling is measured with respect to Nyquist sampling in Cartesian space (i.e., same number of k-space lines between Cartesian and radial). Preliminary retrospective undersampling tests were performed to determine if a lower number of rays could be used, results can be seen in Section 8.6.

Baseline CE-MRA was performed using a 3D GRE sequence with TR/TE 2.75/0.94 ms, flip angle 40°, FOV 450 x 365 x 67.2-78.4 mm^3, matrix 384 x 265, slices 48-56, resolution of 1.2 x 1.4 x 1.4mm^3, with slice resolution interpolated to 1.4 mm, bandwidth 592 Hz/pixel. Postcontrast 3D CE-MRA with the same imaging parameters as baseline was then performed under suspended respiration following administration of Gd-DTPA 0.2 mmol/kg intravenously at 2 mL/sec followed by 20 mL saline flush at the same rate, with image acquisition timed based on CARE bolus tracker. Image acquisition time was recorded for each patient for both CE- and NC-MRA acquisitions.

8.2.1.1 Image Reconstruction

Image reconstruction was performed using MATLAB (R2014a, The MathWorks, Inc., Natick, MA). Coil sensitivity maps were self-calibrated using the densely acquired center of k-space (central 32x32 lines, see Figure 8.2), as previously described (12,13). Undersampled data were reconstructed using an NLM denoising algorithm with 50 iterations on a computer with 6 cores and 96 GB memory.

8.2.2 Image and Statistical Analysis

For qualitative evaluation, images were anonymized and randomized for blind review by two radiologists (Reader 1 with 9 years of experience, Reader 2 with 4 years of experience). Each reader graded for image quality, artifact, and noise on a Likert-type scale of 1-5 (worst-best). We define a score ≥ 3.0 as diagnostically acceptable. A Wilcoxon matched-pairs signed-rank test was performed to determine whether significant difference exists between CE- and NC-MRA acquisitions. For quantitative evaluation, vessel dimensions were made at 3 locations (ascending, arch, descending aorta, Figure 8.3) Apparent contrast-to-noise ratio (CNR) between vessel and background was estimated by measuring signal in the vessel, subtracting the signal value in a region of interest near the vessel, and dividing by the signal in the vessel, to normalize results. This surrogate CNR measurement was necessary because CNR is not straightforward to calculate from GRAPPA and CS data. The locations of the measurements being performed can be seen in Figure 8.3. A paired *t*-test was performed to determine whether significant difference exists between CE- and NC-MRA acquisitions.

8.3 Results

Representative multiplanar reconstructed images can be seen in Figures 8.3 and 8.4. As summarized in Table 8.1, qualitative evaluation by two radiologists showed that there was no significant difference in image quality at the ascending aorta and aortic arch ($p > 0.07$), but there was significant difference at the descending aorta ($p < 0.02$). Artifact and noise scores were higher ($p < .01$) in NC-MRA compared with CE-MRA acquisitions. Apparent CNR measurements were significantly different ($p < 0.05$) between CE- and NC-MRA acquisitions (see Table 8.1). However, vessel dimensions were not significantly different ($p > 0.23$) between both MRA acquisitions (Table 8.2). According to the linear regression analysis (Figure 8.5A), vessel diameters were strongly correlated ($r = 0.992$). According to the Bland-Altman analysis (Figure 8.5B), the measurements of aortic diameter using the two imaging methods were in good agreement (mean difference = -0.02 cm) and showed no systematic trend in difference, and the 95% confidence intervals were relatively narrow (0.12 and -0.16 cm).

8.4 Discussion

This study demonstrates feasibility of accelerated NC thoracic MRA using 3D stack-of-stars and CS. This method is capable of producing diagnostically acceptable image quality on a 1.5T system equipped with standard array coils.

In 19 subjects, while apparent CNR was higher in NC-MRA studies, we found that there was no significant difference in image quality of the ascending aorta and aortic root. Image quality scores were lower for NC-MRA than CE-MRA in the descending aorta, but were nonetheless diagnostically acceptable (> 3.0). Noise and artifact scores were significantly worse for NC-MRA than CE-MRA, although these differences did not appear to impact the measurement of vessel dimensions.

This study has several limitations that merit discussion. First, signal loss related to susceptibility artifact from adjacent bowel gas, the lung-liver interface, or surgical metal produced banding artifacts. This could be addressed with advanced static magnetic field shimming. Second, in order to improve patient comfort, imaging was performed at end inspiration. Further study is warranted to test the impact of breath holding on image quality. Third, this study did not include a comparison with other angiographic modalities such as digital subtraction angiography and computed tomography angiography. Fourth, it was not possible to randomize the pulse sequence order, because NC-MRA must be performed before CE-MRA. While the pulse sequence order is not expected to be a confounder, we are unable to confirm that it had no impact. Fifth, NC-MRA exhibits bright venous single (14), which is not the case for CE-MRA. Therefore readers could not truly be blinded to imaging technique. Sixth, the image reconstruction time is a major limitation. Current reconstruction time per data set using a CPU with 6 cores and 96 GB of RAM is on the order of 6 hours. This could be accelerated using GPU and parallel computing that are available as a product package in Matlab. Faster reconstruction algorithm needs to be explored to make this method viable for clinical use.

8.5 Conclusion

This study demonstrates feasibility of accelerated NC thoracic MRA using 3D stack-of-stars and CS. This new method produces diagnostically acceptable image quality on a 1.5T scanner equipped with standard coil arrays. The results indicate that this could a viable alternative to CE-MRA for patients with poor IV access, or contraindications to gadolinium-based contrast. Further testing is needed to determine the clinical utility in patients with aortic disease, with comparisons to other modalities. Finally, further improvements in reconstruction speed are necessary before clinical translation.

8.6 Supplemental Materials

8.6.1 Nonlocal Means Reconstruction

NLM is a denoising algorithm which compares pixels inside of a search window using weighted averages and has been shown to reduce incoherent artifacts in MRI images (15,16). Prior to NLM denoising k-space data was normalized to the largest value. NLM was performed in three dimensions, with comparison and search windows of size 3x3x3 and 5x5x5 respectively. 50 iterations of denoising were performed per data set.

NLM denoising was carried out as described below (17). A cost function is applied to the spatial neighborhood, S_{nbd}

$$\mathrm{Snbd} = \sum_{p \in tfr} \sum_{q \in \Omega_s(p)} \mathbf{w}_s\,(p,q) \left\| \mathbf{m}_p - \mathbf{m}_q \right\|_2^2 \qquad [8.1]$$

The cost function, eqn 8.1, uses an initial estimate m, where m_p and m_q are individual pixels at points p and q in a particular time frame, tfr. By minimizing this functional, 8.1, undersampled k-space data can have resulting image artifacts resolved. Iterative steps are used to minimize this functional.

Steps followed in reconstruction are outlined below.

(1) An initial estimate is chosen, m_0. The initial estimate for this project was the inverse Fourier transformed undersampled k-space data, with coil

sensitivity maps applied.

(2) The current estimate is projected on the data consistency term:

$$m_{data}^{n} = m^{n} + \mathrm{E}'(\mathrm{d} - \mathrm{E}m^{n}) \qquad [8.2]$$

where E’ is the adjoint operator of E.

(3) Weights are computed according to

$$\mathrm{w}(\mathrm{p},\mathrm{q}) = e^{\frac{-d(p,q)}{h^2}}; d(p,q) = G_{\sigma}\left\| m(N_p) - m(N_q) \right\|_2^2 \qquad [8.3]$$

where d(p,q) is the Gaussian weighted L_2 norm distance between neighborhoods.

(4) The neighborhood term is minimized by applying NLM to the real and complex parts individually according to the weights from Step 3.

(5) The initial estimate is updated according to the new image from the constraints.

Steps 2-5 are repeated a predetermined number of times. In this study the number of iterations performed per data set was 50, with a step size of 0.05. Data fidelity and NLM weights used were 0.4 and 0.3 respectively. The initial estimate, m_0, was the inverse Fourier transform of the undersampled data with coil sensitivity maps applied.

8.6.2 Retrospective Undersampling

In order to test the effect of different number of radial rays acquired, a patient data set was retrospectively undersampled with 32 rays and 16 rays. This retrospective undersampling was performed in the same manner as the retrospective undersampling. The first 32 or 16 rays were selected from each kx-ky partition and reconstruction was performed using NLM reconstruction with the same weighting parameters as were used for the prospective acquisitions. Reconstructed images can be seen in Figure 8.6.

8.7 References

1. Othersen JB, Maize JC, Woolson RF, Budisavljevic MN. Nephrogenic systemic fibrosis after exposure to gadolinium in patients with renal failure. Nephrol Dial Transplant 2007;22:3179-3185.

2. Kanal E, Broome DR, Martin DR, Thomsen HS. Response to the FDA's May 23, 2007, nephrogenic systemic fibrosis update. Radiology 2008;246:11-14.

3. Broome DR, Girguis MS, Baron PW, Cottrell AC, Kjellin I, Kirk GA. Gadodiamide-associated nephrogenic systemic fibrosis: why radiologists should be concerned. Am J Roentgenol 2007;188:586-592.

4. Niendorf T, McKenzie C, Spencer M, Farrar N, Dennis Z, Rofsky N. Image quality improvements in whole body MRA of the aorta by empolying accelerated, non-contrast enhanced, cardiac gated 3D SSFP. In Proceedings of the 12th Annual Meeting of ISMRM, Kyoto, Japan, 2004. p 2570.

5. Xu J, McGorty KA, Lim RP, Bruno M, Babb JS, Srichai MB, Kim D, Sodickson DK. Single breathhold noncontrast thoracic MRA using highly accelerated parallel imaging with a 32-element coil array. J Magn Reson Imaging 2012;35:963-968.

6. Wech T, Pickl W, Tran-Gia J, Ritter C, Beer M, Hahn D, Kostler H. Whole-heart cine MRI in a single breath-hold--a compressed sensing accelerated 3D acquisition technique for assessment of cardiac function. Rofo

2014;186:37-41.

7. Winkelmann S, Schaeffter T, Koehler T, Eggers H, Doessel O. An optimal radial profile order based on the golden ratio for time-resolved MRI. IEEE Trans Med Imaging 2007;26:68-76.

8. Wu Y, Korosec FR, Mistretta CA, Wieben O. CE-MRA of the lower extremities using HYPR stack-of-stars. J Magn Reson Imaging 2009;29:917-923.

9. Chen L, Adluru G, Schabel MC, McGann CJ, Dibella EV. Myocardial perfusion MRI with an undersampled 3D stack-of-stars sequence. Med Phys 2012;39:5204-5211.

10. Wundrak S, Paul J, Ulrici J, Hell E, Geibel MA, Bernhardt P, Rottbauer W, Rasche V. Golden ratio sparse MRI using tiny golden angles. Magn Reson Med 2016;75:2372-2378.

11. Wundrak S, Paul J, Ulrici J, Hell E, Rasche V. A small surrogate for the golden angle in time-resolved radial MRI based on generalized Fibonacci sequences. IEEE Trans Med Imaging 2015;34:1262-1269.

12. Lustig M, Donoho D, Pauly JM. Sparse MRI: The application of compressed sensing for rapid MR imaging. Magn Reson Med 2007;58:1182-1195.

13. Walsh DO, Gmitro AF, Marcellin MW. Adaptive reconstruction of phased array MR imagery. Magn Reson Med 2000;43:682-690.

14. Ho VB, Corse WR, Hood MN, Rowedder AM. MRA of the thoracic vessels. Semin Ultrasound CT MR 2003;24:192-216.

15. Manjon JV, Carbonell-Caballero J, Lull JJ, Garcia-Marti G, Marti-Bonmati L, Robles M. MRI denoising using non-local means. Med Image Anal 2008;12:514-523.

16. Tristan-Vega A, Garcia-Perez V, Aja-Fernandez S, Westin CF. Efficient and robust nonlocal means denoising of MR data based on salient features matching. Comput Methods Programs Biomed 2012;105:131-144.

17. Adluru G, Tasdizen T, Schabel MC, DiBella EV. Reconstruction of 3D dynamic contrast-enhanced magnetic resonance imaging using nonlocal means. J Magn Reson Imaging 2010;32:1217-1227.

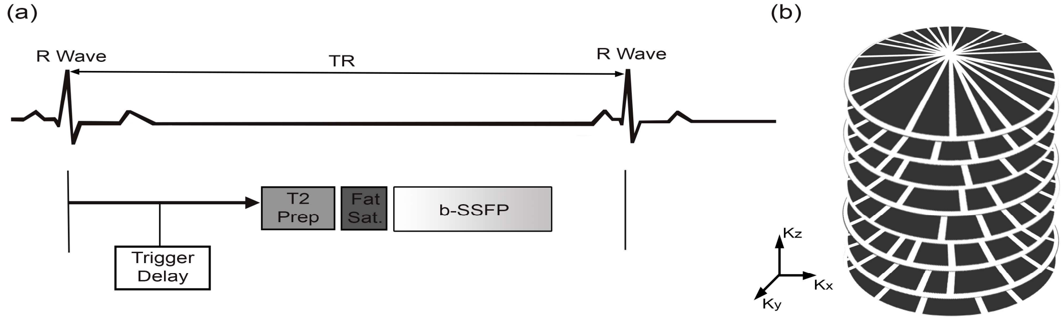

Figure 8.1: Pulse sequence diagram: (a) timing structure for acquisition and (b) 3D radial stack-of-stars sampling pattern with tiny gold angle ratio that has been downsampled by a factor of four for improved visualization. Note that tiny golden angle continues from one stack to another.

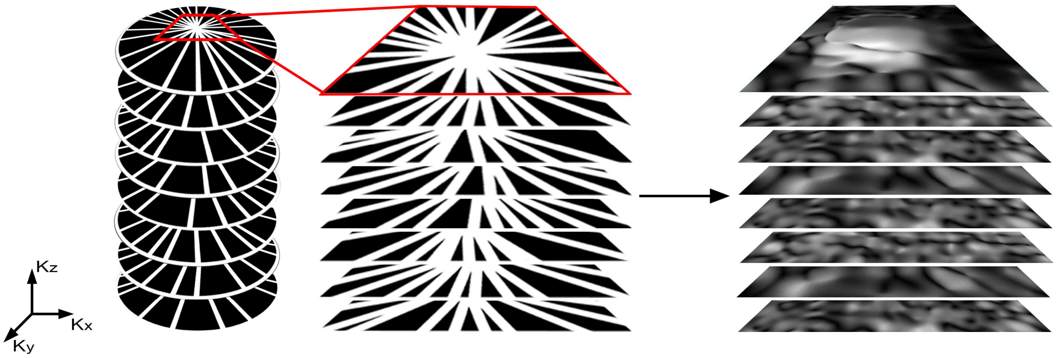

Figure 8.2: Schematic illustrating self-calibration of coil sensitivity maps. Densely sampled low spatial frequencies are used to generate a low spatial resolution image and processed to estimate coil sensitivity as shown. k-Space figure has been downsampled by a factor of four for visual clarity.

CE-MRA NC-MRA

Figure 8.3: Representative multi-planar reconstruction of contrast-enhanced MRA (left) and noncontrast (right) MRA in a patient (39yr, female). Arrows point to locations where vessel diameters were measured.

CE-MRA NC-MRA

Figure 8.4: Representative multiplanar reconstruction of contrast-enhanced MRA (left) and noncontrast (right) MRA in a patient (73yr, Female).

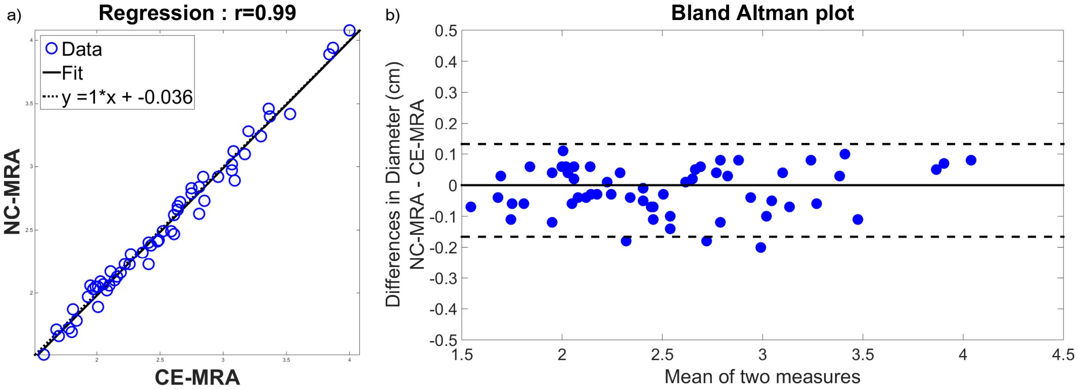

Figure 8.5: Scatter plots comparing vessel diameters between CE-MRA and NC-MRA: linear regression (a) and Bland-Altman analyses (b). According to a regression analysis, vessel diameters were strongly correlated (r = 0.992). According to the Bland-Altman analysis, the two measurements were in good agreement (mean difference of -0.02 cm) and showed no systematic trend in difference. The upper and lower 95% limits of agreement were 0.12 and -0.16, respectively.

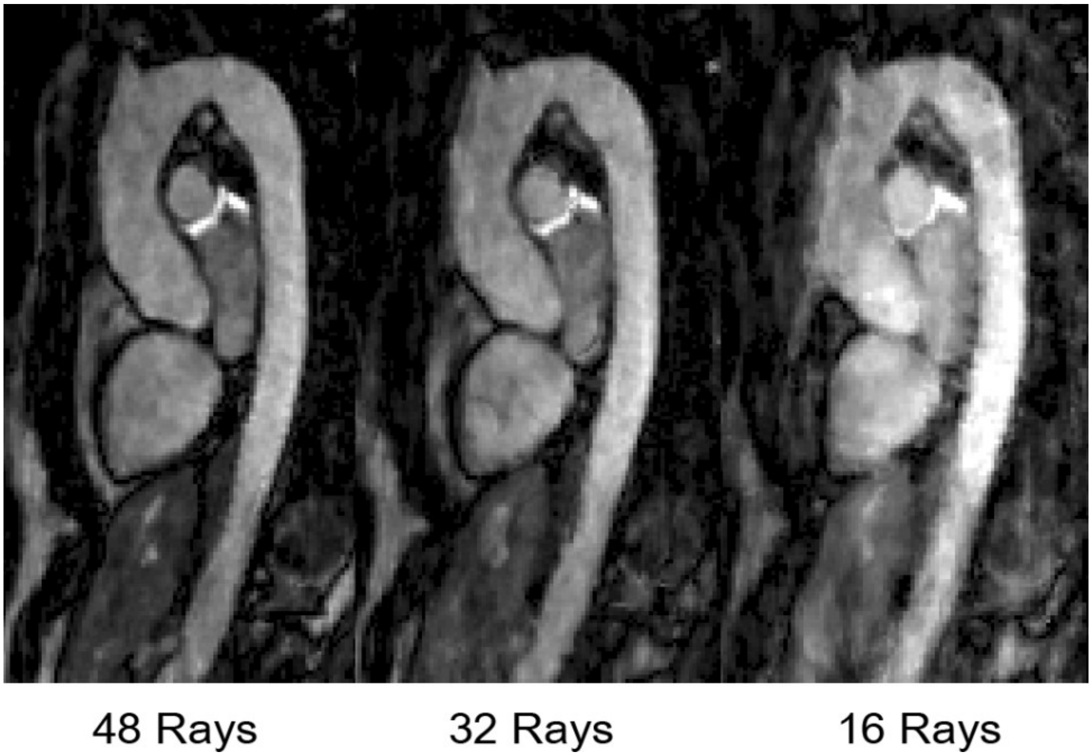

Figure 8.6: Retrospective undersampling was performed on the accelerated acquisition to determine if there was a possible lower value that would be acceptable. 32 rays and 16 rays were tested. It was decided to continue with 48 rays for this study.

Table 8.1: Apparent normalized CNR (left) and vessel diameter measurements (right) for CE-MRA and NC-MRA. Measurements were taken at the sinotubular junction, aortic arch, and descending aorta (as shown in Figure 8.3). Values represent mean ± standard deviation. For apparent CNR there was a significant difference between the two methods at all locations. For vessel measurements, none of the diameters were significantly different between the two methods.

		Normalized Signal Difference			**Vessel Diameter Measurements (cm)**		
		CE-MRA	**NC-MRA**	**p-value**	**CE-MRA**	**NC-MRA**	**p-value**
Location	**Sinotubular Junction**	0.76 ± 0.12	0.83 ± 0.11	0.03	3.14 ± 0.44	3.12 ± 0.49	0.26
	Aortic Arch	0.82 ± 0.12	0.91 ± 0.10	0.03	2.41 ± 0.35	2.39 ± 0.35	0.28
	Descending Aorta	0.84 ± 0.05	0.89 ± 0.07	0.02	2.08 ± 0.32	2.06 ± 0.31	0.23

Table 8.2: Comparison of overall image quality score, noise, and artifact scores evaluated. Results represent mean ± standard deviation of average of 2 readers.

		CE-MRA	**NC-MRA**	**p-value**
Location	**Aortic Root**	3.58 ± 1.29	3.34 ± 0.94	0.25
	Ascending Aorta	3.95 ± 1.06	3.58 ± 0.89	0.08
	Descending Aorta	4.11 ± 1.11	3.34 ± 1.19	0.016
Noise		4.03 ± 1.05	3.08 ± 1.19	0.001
Artifact		3.84 ± 1.10	3.03 ± 1.03	0.009

CHAPTER 9

CONCLUSION

9.1 Conclusion

MRA is a powerful tool that can be used for the diagnosis and for guiding treatment in patients with arterial diseases. Contrast enhanced methods, through the use of a gadolinium based contrast agent, have been the most frequently used. With the emergence of the risk for NSF for patients with impaired renal function, and recently with reports of gadolinium remaining in the brain even in patients with normal renal function (1-3), their clinical utility is beginning to be explored again. There are multiple techniques for imaging of the arteries that have been developed.

When increasing the field strength there are multiple benefits possible. There is an increase in the SNR, which can be leveraged to accelerate the acquisition, or increase the resolution of the images. It also presents technical challenges, increase in SAR, and increase in field inhomogeneities.

When using ECG-FSE to image the arteries of the thigh and pelvis at 3T it was observed that there was signal loss in the right femoral artery due to B1+ field inhomogeneities. There are a couple approaches to correcting these B1+ inhomogeneities, but one of the approaches requires specialized hardware to perform parallel transmission. The other method of correcting these is through the use of high permittivity padding (4-11). Parallel transmission is an active method of correction that can improve homogeneity across the sample, whereas the use of padding is passive. Through the use of high permittivity padding we were able to improve the conspicuity of the femoral arteries.

The quadruple inversion recovery sequence has been shown to be robust

(12,13), but the acquisition is long, typically on the order of ~12-15 minutes. By imaging at 3T we were able to leverage the increased SNR to accelerate the acquisition. It has been shown that through the use of 3D radial stack-of-stars with tiny golden angles that it is possible to acquire the abdominopelvic MRA in one half the time as previously performed through the use of just parallel imaging.

When imaging the thoracic aorta visualization of the aortic root, including the annulus and sinotubular junction is diagnostically relevant. In order to acquire images with clear diagnostic quality it is necessary to image during the diastolic phase of the cardiac cycle to minimize cardiac motion, and be able to perform the imaging in a single breath hold to eliminate bulk motion from respiratory motion. This work showed that it was possible to accelerate a T2-prepared b-SSFP readout acquisition through the use of 3D radial stack-of-stars imaging, and obtain diagnostic quality results.

MRA is an important tool for the diagnosis and treatment of arterial diseases in patients. As a result of recent concerns with the gadolinium contrast agent used in MRI for improving visualization of blood vessels, it has become important to develop imaging methods that acquire diagnostic quality images. Several of the methods that have already been developed show promise, but still need further development and improvement. In this work we have shown that through the use of high permittivity padding, we are able to improve vessel visualization. We have also been able to produce diagnostic quality images of the thoracic aorta, and acquired abdominopelvic images in half the time as previous methods through the use of 3D radial acquisitions.

9.2 References

1. McDonald RJ, McDonald JS, Kallmes DF, Jentoft ME, Murray DL, Thielen KR, Williamson EE, Eckel LJ. Intracranial gadolinium deposition after contrast-enhanced MR imaging. Radiology 2015;275:772-782.

2. Kanda T, Ishii K, Kawaguchi H, Kitajima K, Takenaka D. High signal intensity in the dentate nucleus and globus pallidus on unenhanced T1-weighted MR images: relationship with increasing cumulative dose of a gadolinium-based contrast material. Radiology 2014;270:834-841.

3. Errante Y, Cirimele V, Mallio CA, Di Lazzaro V, Zobel BB, Quattrocchi CC. Progressive increase of T1 signal intensity of the dentate nucleus on unenhanced magnetic resonance images is associated with cumulative doses of intravenously administered gadodiamide in patients with normal renal function, suggesting dechelation. Invest Radiol 2014;49:685-690.

4. Yang QX, Wang J, Wang J, Collins CM, Wang C, Smith MB. Reducing SAR and enhancing cerebral signal-to-noise ratio with high permittivity padding at 3 T. Magn Reson Med 2011;65:358-362.

5. Yang QX, Rupprecht S, Luo W, Sica C, Herse Z, Wang J, Cao Z, Vesek J, Lanagan MT, Carluccio G, Ryu YC, Collins CM. Radiofrequency field enhancement with high dielectric constant (HDC) pads in a receive array coil at 3.0T. J Magn Reson Imaging 2013;38:435-440.

6. Teeuwisse WM, Brink WM, Haines KN, Webb AG. Simulations of high permittivity materials for 7 T neuroimaging and evaluation of a new barium titanate-based dielectric. Magn Reson Med 2012;67:912-918.

7. Lindley MD, Kim D, Morrell G, Heilbrun ME, Storey P, Hanrahan CJ, Lee VS. High-permittivity thin dielectric padding improves fresh blood imaging of femoral arteries at 3 T. Invest Radiol 2015;50:101-107.

8. Lindley MD, Kim D, Morrell G, Heilbrun ME, Storey P, Hanrahan C, Lee VS. High-permittivity thin dielectric pad improves peripheral non-contrast MRA at 3T. J Cardiovasc Magn Reson 2014;16:P166.

9. Haines K, Smith NB, Webb AG. New high dielectric constant materials for tailoring the B1+ distribution at high magnetic fields. J Magn Reson 2010;203:323-327.

10. de Heer P, Brink WM, Kooij BJ, Webb AG. Increasing signal homogeneity and image quality in abdominal imaging at 3 T with very high permittivity materials. Magn Reson Med 2012;68:1317-1324.

11. Brink WM, Webb AG. High permittivity pads reduce specific absorption rate, improve B1 homogeneity, and increase contrast-to-noise ratio for functional cardiac MRI at 3 T. Magn Reson Med 2014;71:1632-1640.

12. Atanasova IP, Lim RP, Chandarana H, Storey P, Bruno MT, Kim D, Lee VS. Quadruple inversion-recovery b-SSFP MRA of the abdomen: initial clinical validation. Eur J Radiol 2014;83:1612-1619.

13. Atanasova IP, Kim D, Lim RP, Storey P, Kim S, Guo H, Lee VS. Noncontrast MR angiography for comprehensive assessment of abdominopelvic arteries using quadruple inversion-recovery preconditioning and 3D balanced steady-state free precession imaging. J Magn Reson Imaging 2011;33:1430-1439.